

AN ABSTRACT OF THE DISSERTATION OF

Daniel S. Gruss for the degree of Doctor of Philosophy in Physics presented on
May 20, 2016.

Title: Quantum and Classical Simulation of Electronic Transport at the Nanoscale.

Abstract approved:

Michael P. Zwolak

Time-dependent electronic transport is increasingly important to the state-of-the-art device design and fabrication. The development of nanoscale sensing, the harnessing and control of structural fluctuations, and the advancement of next-generation materials all require a treatment of quantum dynamics beyond the level of traditional methods and a more nuanced approach to the quantum/classical divide. It is thus becoming necessary to incorporate new theoretical approaches—as well as efficient computational tools—to fully understand the underlying physical processes in these systems, as well as the approximations used to solve for their behavior. In addition, recent progress in ultra-cold atom experiments allows for the direct observation of many-body transport in the laboratory—a form of quantum simulation—which provides a parallel technique for solving these problems.

We focus on simulation methods for electronic dynamics, from cold-atom to computational approaches. To this end, we examine the use of atomic transport in elucidating the nature of electronic transport and the simulation of the latter in classical computers. In particular, we develop an analog of a scanning tunneling microscope and a corresponding operational meaning of the local density of states for strongly interacting particles—a situation where the concept of quasi-particles cannot often be used. This

technique captures the energetic structure of a many-body system through the measurement of particle transport, as well as gives a novel approach to numerically characterize the system. We also demonstrate how interactions can generate steady-state currents in fermionic cold-atom systems, as opposed to globally biased systems.

We then shift our attention to the extension of numerical simulations of quantum transport to an open-system formalism—that is, inclusion of an external environment that drives the system out of equilibrium. We include an explicit treatment of the electronic reservoirs of a device with a corresponding finite-time relaxation. This yields a computationally efficient method for simulation of dynamics under non-equilibrium conditions. Moreover, it gives a general simulation technique for finding periodic steady-states, the decay of local disturbances, and the real-time response to structural changes.

©Copyright by Daniel S. Gruss

May 20, 2016

All Rights Reserved

Quantum and Classical Simulation of Electronic Transport at the Nanoscale

by

Daniel S. Gruss

A DISSERTATION

submitted to

Oregon State University

in partial fulfillment of
the requirements for the
degree of

Doctor of Philosophy

Presented May 20, 2016
Commencement June 2016

Doctor of Philosophy dissertation of Daniel S. Gruss presented on May 20, 2016.

APPROVED:

Major Professor, representing Physics

Chair of the Department of Physics

Dean of the Graduate School

I understand that my dissertation will become part of the permanent collection of Oregon State University libraries. My signature below authorizes release of my dissertation to any reader upon request.

Daniel S. Gruss, Author

ACKNOWLEDGEMENTS

I would like to start off by expressing my deepest thanks to my advisor and mentor, Michael Zwolak, for his guidance, encouragement, and especially patience. A not-insignificant part of my accomplishments and opportunities I've had can be traced back to his support. I would also like to thank my committee members Ethan Minot, David Roundy, and Guenter Schneider. Fellow collaborators Kirill Velizhanin, Massimiliano Di Ventra, and Chih-Chun Chien. My group members for their discussions and company Subin Sahu, Joshua Kincaid, and Xiaoxuan Huang. The many professors and students I've worked with during my time at OSU. And most importantly, Jessica—who offered a multitude of support, reassurance, and advice throughout my studies—and the rest of my family.

TABLE OF CONTENTS

	<u>Page</u>
1 Introduction	1
1.1 Simulation and Computational Physics	2
1.2 Fundamental Approach	3
1.3 General Quantum Mechanics	4
1.3.1 Classical Simulation	5
1.3.2 Quantum Simulation with Cold Atoms	7
1.4 Time Evolution of Quantum Systems	10
1.5 Applications	12
1.5.1 Quantum Chemistry	12
1.5.2 Device Design	14
1.5.3 Sensing Applications	14
1.6 Outline	16
2 Mathematical Background	18
2.1 The Fundamentals	18
2.2 Many-body Quantum Mechanics	20
2.2.1 Full Time Evolution	23
2.2.2 Realtime Approach	24
2.2.3 Mean Field Approximation	27
2.3 Electronic Transport	29
2.3.1 Lindblad Equation	30
2.3.2 Landauer Approach	33
2.3.3 Non-Equilibrium Green's Functions	35
2.4 tDMRG/MPS	42
2.5 Conclusion	50
3 Energy-resolved Atomic Scanning Probe	51
3.1 Introduction	51
3.2 Model	52
3.3 Thin Band Probe	55
3.4 Interacting System Simulation	59
3.5 Methods	61
3.6 Conclusion	65
4 Interaction-Driven Electronic Transport	66
4.1 Introduction	66
4.2 Interaction-induced Transport	69
4.3 Results and Discussions	72
4.4 Higher-order Correlations and td-DMRG	77

TABLE OF CONTENTS (Continued)

	Page
4.5 Conclusion	80
5 Landauer's Formula with Finite-Time Relaxation	82
5.1 Introduction	82
5.2 Model	85
5.3 Results	88
5.3.1 Single-Site Homogeneous System	88
5.3.2 Intermediate Relaxation	90
5.3.3 Small Relaxation	91
5.3.4 Large Relaxation	93
5.3.5 Reservoir Continuum Limit	94
5.4 Conclusion	96
6 Derivations and Analysis of Finite-Time Relaxation	98
6.1 Steady-State Current Derivations	98
6.1.1 Single Extended Reservoir State Green's Function	98
6.1.2 Landauer-like Formula	101
6.1.3 Small Relaxation, Continuum Limit	104
6.1.4 Large Relaxation	105
6.2 Markovian Master Equation	105
6.2.1 Single Extended Reservoir State Green's Function	106
6.2.2 Steady-State Current	108
6.2.3 Small and Large Relaxation Limits	110
6.3 Validity of the Markovian Master Equation	112
6.3.1 Broadening and the Fermi Level	112
6.3.2 Asymmetric Reservoirs	115
6.4 Linear Reservoir with Equally Spaced States	117
6.5 Single-Site Reservoir Rate Equation	118
6.6 Conclusion	120
7 Discord, Dephasing, and Steady States	121
7.1 Introduction	121
7.2 Discord	122
7.2.1 General Measurement	123
7.2.2 Particle Conserving Measurement	125
7.2.3 Four Site, Particle Conserving Measurement	127
7.3 Analytical Results	130
7.4 Open System Exact Solution	132
7.5 Interacting System	136

TABLE OF CONTENTS (Continued)

	<u>Page</u>
7.6 Conclusion	137
8 Conclusion	139
9 Bibliography	141
Appendices	160

LIST OF FIGURES

<u>Figure</u>	<u>Page</u>
1.1 The interrelationship between levels of simulation and physical reality	5
1.2 Simulation of electronic phenomena with cold atoms	9
1.3 Design of catalytic materials	13
1.4 Computational design of electronic materials	14
1.5 Dynamical sensing applications for electronic devices	15
2.1 Diagram of electron transport in a device	35
2.2 Time contour in the complex plane	38
3.1 Energy-resolved atomic scanning probe	54
3.2 Non-interacting, fermionic LDOS	57
3.3 Many-body, fermionic LDOS	60
3.4 The “scanning-mode” of the energy resolved probe	62
4.1 Schematic plot of the experimental set up we simulate	68
4.2 Mean-field particle number and number fluctuation dynamics	71
4.3 Average current dynamics and energy spectra	73
4.4 Currents induced by different ways of switching-on the interaction	74
4.5 Current versus time for varying levels of approximation	79
4.6 Average current versus U	80
5.1 Schematic representation of the model	84
5.2 Regimes of the electronic current	89
5.3 Expansion of the plateau	91
6.1 Spectral densities for a 1D reservoir	113
6.2 Asymmetric system response	115
7.1 Calculation of the conditional entropy within a steady-state current	125
7.2 Minimum values of the quantum discord	126
7.3 Conditional entropy of the two-site measurement	128
7.4 Minimized discord of the two-site particle basis measurement	129
7.5 Simulation of dephasing-induced resistivity	134
7.6 Discord of an interacting steady state	136
7.7 Resistivity from an interacting current	137

LIST OF APPENDICES

	<u>Page</u>
A Transformations, Distance Measures, and Examples	161
A.1 Jordan-Wigner Transformation	161
A.2 Wick's Theorem	163
A.3 Quantum Discord	165
A.4 Distance Measurement	166
A.5 Switching Between Levels of Approximation	167
A.5.1 Operator to Superoperator Conversions	168
A.5.2 Correlation Matrix to Density Matrix Conversion	169
A.6 Examples	170
A.6.1 Born-Markov Approximation	170
A.6.2 Non-interacting Green's Functions	172
B Computational and Practical Considerations	174
B.1 Scientific Computing and Python	174
B.1.1 NumPy	175
B.1.2 SciPy	176
B.1.3 Cython	179
B.1.4 Profiling and Testing	180
B.2 Other Scientific Computing Libraries	181
B.3 Analytic Work	182
B.4 Computational Complexity	182

Chapter 1: Introduction

The quantum mechanical nature of matter—in particular, the transport of electrons—plays a huge role in today’s modern society. It forms the basis of computing, the delivery and consumption of energy, and the storage of information. Starting with the transistor, knowledge of the fundamental nature of matter enabled unimaginable advances in these fields. We live our lives in the “classical” world where objects behave how we expect them to: stuff exists in one place and moves according to simple rules, but we are still reliant on quantum physics—that inherently unpredictable, unintuitive behavior at the atomic scale—for present-day technologies.

The foundational principles behind quantum mechanics are relatively unchanged from the 1920’s. In 1923, Louis de Broglie put forth his postulate of matter waves [1] and by 1930, Schrödinger generalized it with his wave equation [2], Werner Heisenberg formulated his uncertainty principle [3], and Paul Dirac unified the theory with special relativity [4]. In 1932, John von Neumann formalized it as linear operators in Hilbert spaces [5].

It is a testament to the rigor and applicability of these fundamental works that they posed questions that still remain open today. Present-day simulations and representations of physical systems can be completely described in the context of the original formulation.

The mathematics within this thesis makes a direct link to these postulates and, as shown in Chapter 2, can be derived directly from them.¹

While the core principles remain the same, our knowledge about quantum mechanics is far from complete. Even some of the most basic problems elude an exact analytical solution, and treating a small number of particles numerically quickly becomes extraordinarily difficult. The n -body problem of classical physics is also present, and greatly increases the challenge of finding solutions to open questions here.

Before getting into the mathematical details, though, this chapter provides a brief overview of some of the general history and ideas behind the research in the rest of this thesis.

1.1 Simulation and Computational Physics

From a practical standpoint, most problems in physics are intractable using analytic methods from first principles. The problem and the fundamental equations may be simple to write down, but finding a solution may be extremely difficult. Fortunately, since we typically care about connections to physical reality, an approximate or numerical approach is often just as good as an exact one—in the same way that an engineer does not need an analytic expression for the forces exerted on a bridge.

However, numerical solutions also allow us to tease out the underlying properties of a complex system. We can perform experiments “*in silico*”—that is, classically—by varying parameters and assumptions of our model and performing “measurements” on the results. The standard processes of experimental design, data analysis, and hypothesis testing apply in much the same ways as a physical experiment. A simpler version of the behavior can be posited, which can, in turn, be tested. In addition, this line of inquiry

¹That is not to say that quantum physics has not moved forward in the meantime. Quantum field theory [6], quantum chromodynamics [7, 8], and electroweak unification [9] are important components of theoretical quantum physics, and unification of the quantum world with gravity remains an open problem.

is bounded only by the amount of computational power available, which means a potentially large number of samples and searches over multi-dimensional parameter space. As computers get larger and faster, more complexity can be introduced and studied. Naturally, a major concern is that these conclusions match those in the laboratory, but beyond that strict requirement, researchers have the freedom to build and test various techniques to solve difficult problems.²

This thesis is focused on physical *simulation*, which attempts to create a realistic model of a given system and then allowing it to evolve over time. In practice, the line between a numerical solution and a simulation is quite arbitrary, as computational methods of dealing with dynamics are very similar to other processes. The two terms can usually be interchangeable.

1.2 Fundamental Approach

The study of complex phenomena admits two, sometimes complementary, approaches to scientific discovery: “bottom up” versus “top down,” each with their respective advantages and disadvantages. In the “top down” approach, one attempts to find fundamental rules through the observation of a collective process or from a holistic point of view. The other, “bottom up,” starts with a set of assumptions and works to explore the consequences or emergent behavior. The results presented in this thesis would arguably qualify as “bottom up.” The model is typically defined as a first step in each problem, which is usually described in a simple manner, after which the dynamics are explored and conclusions about its general functionality are found.

It is useful to be aware of the amount of approximation even within a numerical calculation. The error associated with a computation can arise from the model (such as using a

²The need for approximate, numerical calculations has largely been responsible for the rise of computing technology. Analog computation dates as far back as ancient Greece, where the Antikythera Mechanism was used to predict celestial positions [10]. The earliest programs ran on the ENIAC machine—the first general purpose computer—and were used to determine the feasibility of the thermonuclear weapon [11].

simpler system to represent a more complicated one), the solution to the model (such as intentionally using an approximate solution to an exactly-defined model to reduce the computational complexity), or from a general limitation of the process (such as rounding error). In a well-performed calculation, all potential sources of error are accounted for and reported.

Numerical exactness is the property of a computational method to faithfully reproduce the exact solution to within arbitrary precision. One such algorithm is tDMRG (time-dependent density matrix renormalization group—discussed in more detail in Sec. 2.4): the amount of approximation error present in the result is a function of the simulation parameters, so they can be tuned until convergence is reached. Even though an analytic output does not exist, it can be proven that the results will match the non-approximate solution within the correct limits.

Even though we focus mainly on computational solutions, that does not mean that we disregard analytic work. It is, in fact, the opposite. Analytics are critical for testing results on smaller, more tractable problems. If a numerical result displays a certain property (for instance, it appears to be linear within a particular regime), then that can guide the approximations taken to find a simpler, exact solution (like performing series expansions in the correct variables and limits). In addition, it is often useful to create forms that describe a complex behavior in a simplified manner, leading to interesting relationships that emerge from complicated interactions.

1.3 General Quantum Mechanics

In general, the challenges associated with real quantum-mechanical systems are difficult because of the tiny spatial extent and extremely fast speeds involved. Most readily observable phenomena occur at a classical timescale, which means that very precise measurements are needed to discriminate quantum effects. Observing processes at this

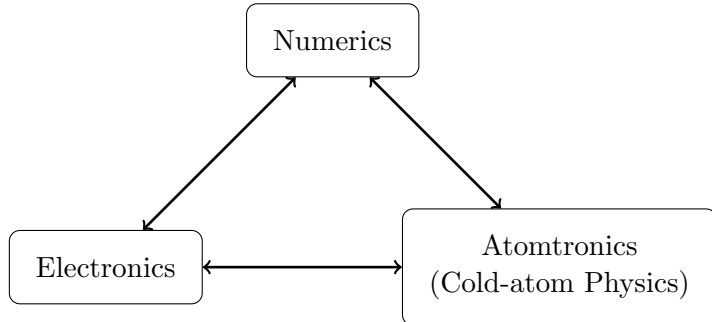


Figure 1.1: The interrelationship between levels of simulation and physical reality. Computational work allows for the simulation of quantum mechanics within a classical computer. These same models can be simulated physically within the laboratory using cold-atom experiments. Each box in this figure provides motivation for the other two.

scale remains a challenge, but nevertheless is regularly demonstrated—such as the recent observation of light as both a particle and a wave [12].

Even though individual quantum events—such as an electron moving from one place to another or a single spin flip—are hard to discriminate, the fundamental nature of the process plays an important role in the bulk properties of the material. Quantum effects are readily measurable without specialized equipment and we rely on their effects for a significant amount of our modern technology.

The contents of this thesis are mainly concerned with problems of the first kind: fine-grained electronic processes that can be extraordinarily difficult to measure in practice, particularly due to their time-dependent nature. Luckily, we are not restricted only to measuring these effects in electronic systems. As shown in Fig. 1.1, two other fields allow researchers to approach the problem in a complementary manner: classical simulation and quantum simulation in engineered cold-atom experiments.

1.3.1 Classical Simulation

As is discussed in further detail in Chapter 2, the computational effort needed to simulate a quantum system grows rapidly with the system size. Anything more complicated

than a few tens of atoms quickly becomes unfeasible to calculate exactly, even on the largest supercomputers. However, there are several methods to treat these systems approximately, often to a very high degree of accuracy.

Even though a quantum system may have an intractable number of degrees of freedom, in many realistic scenarios only a small part of this space needs to be actually explored. States generally stay close to thermal equilibrium, particle number remains exactly or nearly constant, and time evolution proceeds mostly in a continuous manner. More importantly, long range correlations and entanglement do not typically spontaneously develop.³ There remains a concept of approximate “locality,” which means that even though a particle *could* become entangled with any other particle, in practice they only tend to develop correlations to those near one another. This is one of the reasons why creating a quantum computer is so difficult: long-range correlations need to be created and maintained, while the natural tendency of the system is to decohere into a more local state.

Therefore, the general way forward in simulating these systems is to restrict the total space needed to accurately replicate the higher-dimensional state space. In the simplest case where the particles are non-interacting, one can immediately reduce from an exponential-sized space to a polynomial one with no loss of accuracy. If particle number is conserved, as in a closed system, then one only needs to work with configurations that contain the right number and can safely ignore the rest. Density functional theory (DFT) is a computational method that uses the local particle density to investigate the electronic structure of many-body systems [14]. tDMRG theory restricts the space to components that contribute the most to the overall state [15, 16].

Along with the process of making better approximations, the available computing power for these problems continues to grow. Although Moore’s law is coming to an end [17], the rise of cheaper and more energy efficient hardware means that the ability to simulate complex systems will continue to increase. Moreover, the types of algorithms used are

³The key word here is “typically” as there are, of course, many counterexamples of very interesting materials that do otherwise [13].

well suited to parallelism, meaning that a difficult calculation can be distributed over a large number of processors. As the processor industry makes the transition from increasing clock speed to increasing cores, this type of numerical work can readily take advantage of the change, whereas traditional applications are struggling to transition to a parallel machine [18]. In addition, the invention of GPU-based processing [19] or many integrated core architectures [20] means that an increasing amount of computational power will continue to be available in the near future.

1.3.2 Quantum Simulation with Cold Atoms

Recent advances in the study of cold-atom systems have led to a parallel method of studying quantum physics in the laboratory. Instead of working with electrons or phonons as the fundamental particles, whole atoms can be cooled to very low temperatures, at which point their quantum nature becomes the most important—whereas at high temperatures, they quickly undergo decoherence due to interactions with their environment.

When multiple electrons, protons, and neutrons are formed into an atom or molecule, the addition of angular momenta determines the net spin. This depends on the composite particles: for instance, hydrogen has spin $\frac{1}{2}$ while helium has spin 0. Like their fundamental particle counterparts, atoms with a half-integer spin are fermions and obey the Pauli exclusion principle and ones with integer spins are bosons. A natural consequence of this is that ultra-cooled bosonic atoms are able to occupy the same quantum state simultaneously in what is known as a Bose-Einstein condensate [21–23].

The cooling process is usually performed through a combination of laser and evaporative cooling methods. The required temperature is in the microkelvin range and so requires a precise control over the kinetic energy of the atoms. Laser cooling involves tuning an incident beam to a frequency that is slightly lower than an interatomic transition within the atom. Since the frequency is mismatched, it only weakly interacts with the atom. However, if the atom is moving in the direction of the laser, then it is Doppler shifted and the atom is able to absorb an incoming photon. This state is typically unstable

and a photon with similar energy is re-emitted, but in a random direction. Due to conservation of momentum, the atom will eventually be slowed through a series of these interactions [24, 25].

To achieve even colder temperatures, an evaporative cooling process is applied, which is functionally similar to air-cooling systems of the same name. The total temperature of the atoms is lowered by allowing the atoms with the highest kinetic energy to escape the system. This is usually done by reducing the depth of the trap that the atoms are held in, making it unable to contain the fastest atoms. These atoms compose the long tail of the energy distribution and remove the bulk of the energy when they exit the system [26].

Once sufficiently cool, then it is possible to probe the quantum nature of the atoms through a series of careful experiments. Various potentials can be applied to the atoms through the use of electric and magnetic fields and the system can be allowed to reach a ground state or to undergo some dynamical process. More importantly, since the bosons and fermions used are atoms, then they can be directly observed using light. The usual states of the atom still exist, so their reflection or transmittance acts as normal and the position of the particles can be seen through a microscope. Although the measurement is still destructive, the experiment can be repeated identically and measured at different times to record the time evolution. Moreover, the atoms are much more massive than electrons, so the timescales involved are much slower than in electronic systems.

Finally, even though the atoms are typically electronically neutral, they can still exhibit particle-particle interactions by manipulating the energy states of the electrons within the atom. A common method of performing this is by using a Feshbach resonance [23], which creates a bound state between atoms relative to the kinetic energy of a collision. An external field is applied which amplifies the hyperfine structure of the atoms. The strength of this field determines the magnitude of the many-body interaction and allows experimenters to tune the interaction magnitude from non-existent to strong.

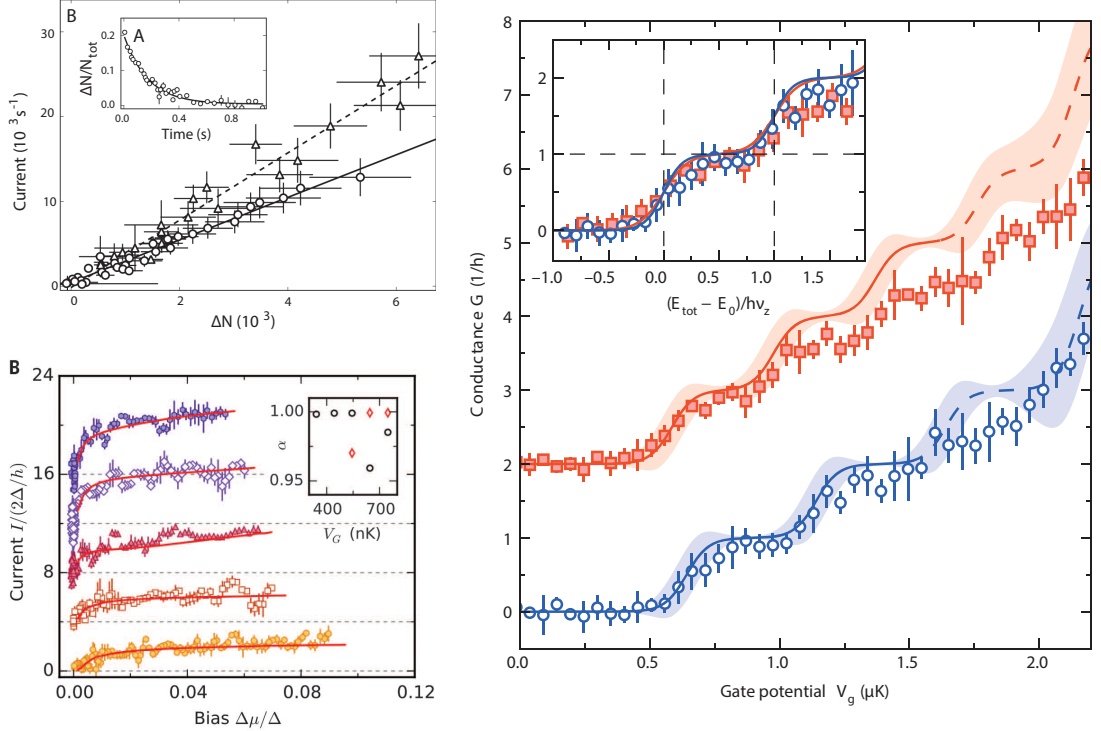


Figure 1.2: Simulation of electronic phenomena with cold atoms. Two clouds of ultra-cold ${}^6\text{Li}$ fermionic atoms with a particle density mismatch are allowed to come into contact with one another and a total current measured through total particle count. (Top Left) Ohmic conduction between two clouds in the ballistic transport regime. (Bottom Left) Non-linear transport of a strongly correlated superfluid. (Right) A quantum point contact via use of a laser confining potential and a micron-scale channel. The gate potential was created through the use of an additional laser beam providing an attractive potential. The solid lines are the theoretical predictions based on the Landauer formula, with the inset showing the plateau as a function of reduced energy. These results were reported in Refs. [27, 31, 32].

Special care must be taken to trap these atoms into a particular region and to apply the desired potential. Again, because of the atoms' neutrality, the electronic structure must be used to achieve the wanted effect. Mageneto-optical traps operate on a similar principle to the laser cooling: a spatially varying field is applied to the trap region with causes a shift in the magnetic-sensitive levels of the electronic structure. This shift increases with distance away from the center of the trap, so atoms moving away from the center are likely to absorb an incident photon and be pushed back towards the center.

With this method, experimenters are able to create arbitrary potentials on which to study ground state generation or time evolution phenomena [25].

Much work in the state-of-the-art of quantum simulation of fermionic systems has been done by Esslinger’s group at ETH [27–33]. Using a ${}^6\text{Li}$ -based cloud, the group has demonstrated ballistic-to-diffusive transitions, quantized conductance, and strongly correlated transport, among others (see Fig. 1.2). Although current progress in interacting systems is limited to the mean-field regime, experimentalists are rapidly approaching the ability to provide insights into open questions of condensed matter physics.

An alternative method involves using the magnetic moment of the whole atom. If a cooled atom is placed into strong magnetic field, then the magnetic moment will align in the same direction in order to minimize the energy. However, since the magnetic moment itself is quantized, this alignment cannot match an arbitrary magnetic field. The result is that when a weaker, spatially varying field is added to the strong one, it creates places where all the magnetic moments are aligned but the atoms still exist within an energy potential. With this technique, it is possible to pattern a chip with a magnetic material and use that to construct geometries of trapping potentials [34–36].

1.4 Time Evolution of Quantum Systems

A rapidly emerging field of study in quantum simulation—and the subject of this thesis—is the study of *dynamical* properties of systems, i.e., ones that are out of equilibrium. The study of static quantum systems has been very successful in describing a large amount of physical phenomena, and the work towards a deeper understanding of explicit time dependence is more challenging in comparison.

The difficulty lies in working with states that are far away from the ground state of a system. A key property of the ground state is that the total energy of the system is the lowest possible, given the physical constraints.⁴ This means that analytic and numerical

⁴Such as particle number, boundary conditions, etc.

solutions admit a number of variational and iterative techniques to find the solution. In short, one can always “spend more time” adjusting a solution to locate a more accurate candidate for a ground state, and a calculation of the total energy will show if a new solution is better than a previous one.

In the time-dependent case, this is no longer true, and we must instead find methods that give solutions for how the system behaves for each slice of the time domain. On the numerical side, the equivalent comparison is between performing a minimization routine and solving a set of coupled differential equations. Often times, the process comes down to controlling error associated with a discretization parameter (such as the timestep interval) and running increasingly more fine grained calculations until the results converge. Calculations in this domain must also deal with propagation of error throughout the simulation, which means that any error earlier in the simulation can greatly influence the final results. As a result, most simulations are limited to a finite-length—usually short—simulation time before the results become unreliable.

One could argue that dynamical properties of quantum systems are responsible for nearly all useful physical processes—such as light emission, electricity, and chemical reactions—but ground- or steady-state approaches have been largely successful in providing the theoretical underpinnings to these systems. For instance, one can use the band structure of a material to derive its conduction properties, even if the exact process of electron motion is not known. In contrast, there are many more open questions that require a more detailed approach. In the field of quantum chemistry, many reactions and processes require an in-depth description of particle motion to understand them [37]. In the world of nanoscale electronics, sophisticated techniques allow for small-scale fabrication of components, which are much more sensitive to electronic motion [38]. Molecular devices not only have complicated energy structures, but can isomerize, or change shape, in real time in response to electronic motion [39].

Of particular interest is when the quantum mechanical nature of electrons interacts with observable motion in the on a larger scale. These two processes have vastly different

timescales associated with them, with the quantum system reacting much faster than the constituent atoms and molecules. As such, these systems are usually treated with the Born-Oppenheimer approach [40] or variations thereof, which assume that the electronic relaxation and nuclear motion are separable. However, this is not always the case and different orders of processes can interact with one another in complex ways [41]. The difficulty here not only lies in the simulation across separated timescales, but deciding how much of the system should be treated quantum-mechanically versus the inclusion of some classical components.

Lastly, the study of open quantum systems [42]—which allow systems to exchange particles with a larger environment—has cleared up some of the questions behind electronic transport. However, the state space is similar to that of static calculations. Often, iterative techniques are applied to find the “steady-state” solution, which is the long-time, stationary response. This process again eliminates the detail of the dynamical motion on top of the non-equilibrium solution, and oftentimes these methods introduce much complexity. A system which constantly fluctuates in time could have interesting classical/quantum interactions which are not entirely captured by the steady-state approach.

1.5 Applications

This section briefly summarizes a few select applications of time-dependent transport theory.

1.5.1 Quantum Chemistry

Catalytic processes play a huge role in material applications and much remains to be learned about the underlying physics. In particular, and of interest to the material in this thesis, electrocatalytic processes and current-induced chemical reactions have a strong dependence on the underlying electronic motion. Individual electron transfer or current

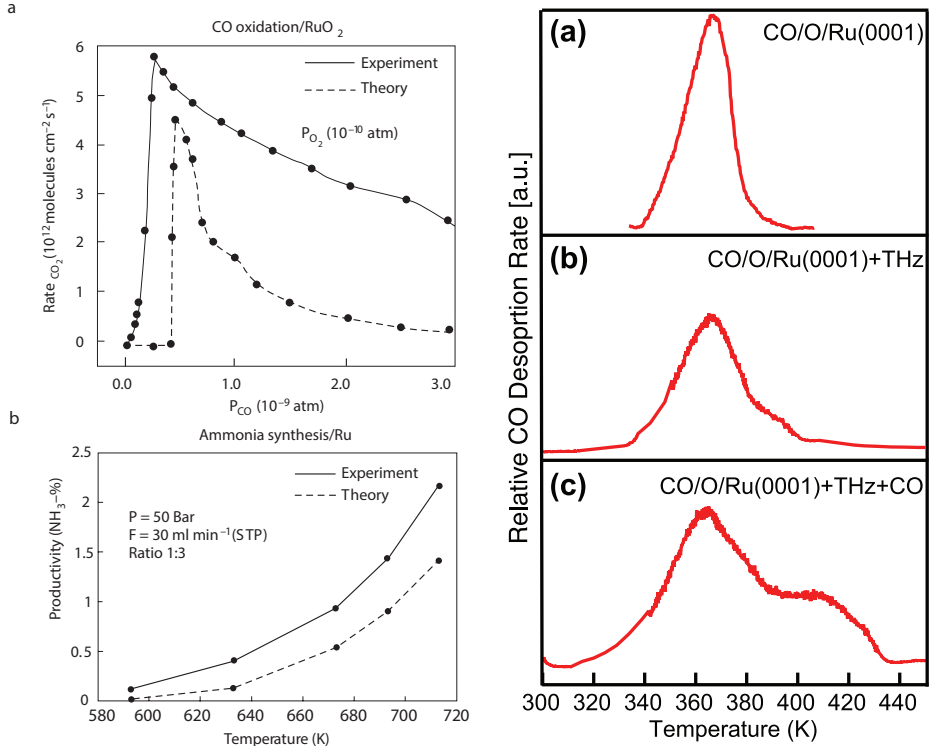


Figure 1.3: Design of catalytic materials. (Top and Bottom Left) The reaction rate was found experimentally and computationally with kinetic models based on DFT calculations. Here, CO oxidation activity and ammonia synthesis productivity were analyzed, as published in Ref. [43]. (Right) Desorption of CO initially, after exposure to THz radiation, and after CO is redosed to form a CO layer, from Ref. [44]. This implies that a strong electric field—which influences the electronic motion—plays a relevant role in the catalytic process and new theoretical models are necessary to accurately model it.

flow can have strong effects on the chemical structure. A more thorough understanding leads to greater predictive power of catalytic processes and a stronger computational support for the development of new processes. Only recently has the design of novel or improved catalysts been attempted entirely *in silico* [45], and there remain many open problems in this field.

Figure 1.3 shows some examples of computational chemistry as applied to catalytic systems. DFT-based models have been largely successful in the computational design of certain materials. However, current research suggests that a more sophisticated model of the electronic properties is needed in certain cases, such as in some strongly correlated

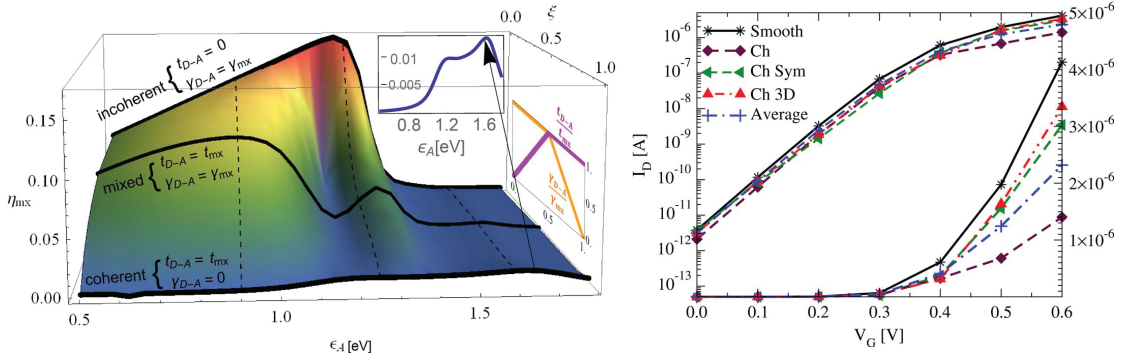


Figure 1.4: Computational design of electronic materials. (Left) Computed efficiency of a solar cell device using open quantum systems and electron-phonon processes, from Ref. [46]. (Right) Full 3D non-equilibrium Green’s function calculation of a doped semiconducting nanowire, from Ref. [47].

oxides, the inclusion of van der Waals interactions, and complications from electrocatalytic and photocatalytic processes [43].

1.5.2 Device Design

A more thorough understanding of dynamical properties can also inspire device design. Electronic devices such as solar cells, those fabricated on the nanoscale, or assembled out of individual molecules all benefit from a more complete picture of real-time processes. Quantum mechanical effects become a primary factor in the efficacy of these devices. Figure 1.4 shows some examples of devices and device design involving first principles transport.

1.5.3 Sensing Applications

Time-dependent processes are increasingly more important in the emerging field of electronic molecular sensing. Here, a current is passed through a nanoscale device that is immersed in a solution which contains the desired sensing target, often an ionic concentration, a molecule, etc. When it is in close proximity to the device, the field effect alters the electronic properties of the material and hence induces a change in the measurable

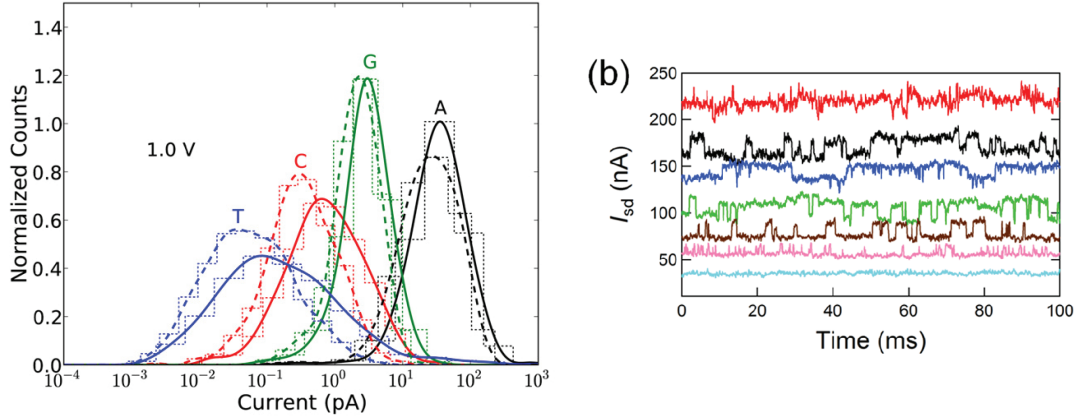


Figure 1.5: Dynamical sensing applications for electronic devices. (Left) A computational study of DNA base discrimination in an electrode nanopore under thermal fluctuations, as reported in Ref. [48]. (Right) Time-dependent current of a liquid-gated carbon nanotube transistor, from Ref. [49].

current. The steady-state methods can work well for these systems; however, the interaction between the two happens in a stochastic manner—the ions or molecules are usually rapidly fluctuating within the medium under the effect of thermal, or Brownian, motion, which needs to be taken into account in the device design.

If the fluctuations are rapid enough or strongly coupled to the electronic system, then their dynamical motion can have a large effect on the device response. A time-dependent model is required to encapsulate the hierarchy of timescales: very fast electronic dynamics, electronic scattering and relaxation times, fast-to-intermediate structural fluctuations of the device and the surrounding media, and long measurement timescales. The key goal in this field is to be able to create an accurate prediction of the aggregate time average that will incorporate this information in a realistic and computationally efficient manner.

In order to simulate devices used at a finite temperature, information about the structural information in addition to electronic properties is required. Usually, the large scale atomic motion is typically treated classically, while the electronic properties are calculated afterwards. This classical simulation is done through the use of molecular dynamics, which simplifies the interatomic interactions to particles with electrostatic

and van der Waals forces between them. This in turn allows for a simulation of time evolution to be completed using much more reasonable computing power at the expense of a complete quantum-mechanical picture.

More sophisticated sensing devices have been proposed for biomolecular applications, such as DNA and protein sequencing. Figure 1.5 shows some examples where the dynamics of the molecules become important for the transport properties and sensing applications. Device design through real-time approaches remains relatively unexplored.

1.6 Outline

The remainder of this thesis is organized as follows:

Chapter 2 contains the mathematical details required for the remainder of this thesis. This chapter provides derivations of the particular concepts we examine starting from the fundamentals of quantum physics.

Chapter 3 contains work performed in collaboration with Chih-Chun Chien and Massimiliano Di Ventra. We develop an analog of a scanning tunneling microscope and a corresponding operational meaning of the local density of states for strongly interacting particles. We apply this approach to an inhomogenous many-body system, in the context of cold-atom simulation.

Chapter 4 contains work also performed in collaboration with Chih-Chun Chien and Massimiliano Di Ventra, and originally published in Ref. [50]. It analyzes the presence of an interaction-induced conducting-to-non-conducting transition in a 1D fermionic system.

Chapter 5, authored in collaboration with Kirill A Velizhanin, derives a connection between an open quantum system in the non-equilibrium Green's function approach with that of a Markovian master equation with explicit extended reservoirs. This formalism

provides a suitable method for determination of the long time dynamics in interacting systems. This work was published in Ref. [51].

Chapter 6 continues the previous one and focuses on the details of the mathematical derivations of the particular system, with additional information about regimes where the master equation breaks down.

Chapter 7 examines the effect of electronic transport on a quantity known as the quantum discord and it's relationship to the ballistic to diffusive transition in an open quantum system.

Appendix A covers some derivations, methods, and examples used in computational quantum simulation and Appendix B discusses some of the software tools and languages used for development of this thesis.

Chapter 2: Mathematical Background

Much of the contents of this thesis involves methods of solving Schrödinger’s equation numerically with a controllable error. The process is as follows: consider the Hamiltonian \mathcal{H} of a simplified model of a physical system. This Hamiltonian represents how all the components of the system interact: how favorable it is for particles to move, how particle-particle interactions occur, how correlations develop, etc. The Hamiltonian encodes all the information about energy in this model “universe.” Along with it, a Hilbert space is defined, which is the vector space in which a single quantum state exists along with a set of observables. Then, working from the postulates of quantum mechanics, information about the ground state or the time evolution of the state can be calculated. This process dates from the foundation of quantum mechanics, but, as will be shown, methods and techniques of numerical solutions are necessary to make complex systems tractable.

2.1 The Fundamentals

Schrödinger’s equation is the basis for describing quantum mechanical behavior, so it is only natural that the first numbered equation in this thesis should reproduce it:

$$\mathcal{H} |\psi(t)\rangle = i\hbar \frac{\partial}{\partial t} |\psi(t)\rangle. \quad (2.1)$$

Here, the time-dependent equation in bra-ket notation was chosen. The Hamiltonian \mathcal{H} describes the quantum system and all information about the state is contained in the vector $|\psi(t)\rangle$. In this form it can apply to any physical system, e.g., a particle in a potential, a set of spins, or states of a molecule.¹ The quantity \hbar is the Planck constant and it describes the relationship between energy and time. At time of writing, it is equal to $6.582\,119\,514(40) \times 10^{-16}$ eV s [52].

The above formalism is useful for a pure quantum state, but often it is necessary to work with mixed quantum states—that is, a statistical ensemble of pure states. If a system is in quantum state $|\psi_i\rangle$ with probability P_i , then we can define the density matrix, ρ , as

$$\rho(t) = \sum_i P_i |\psi_i(t)\rangle \langle \psi_i(t)|. \quad (2.2)$$

We can then use Eq. (2.1) to write down the *canonical time evolution* of the density matrix as

$$\dot{\rho} = -\frac{i}{\hbar} [\mathcal{H}, \rho]. \quad (2.3)$$

Here, the brackets, $[\dots]$, mean commutator: $[A, B] = AB - BA$.

The procedure to find the dynamics of these quantum systems is as follows: define the initial conditions of the density matrix $\rho(t=0)$, define the Hamiltonian of the system \mathcal{H} , and then solve the system of differential equations as defined above.² This solution contains all the information about the quantum state since the time evolution began, from which one can obtain correlations, particle densities, etc. In quantum mechanics, each observable is represented by a Hermitian operator that acts on the state of the system. The outcome of a measurement an observable A can only be one of the eigenvalues of A , but typically this is described using expectation values of operators.³ Using bra-ket notation, this expectation value is calculated by $|\langle \psi(t) | A | \psi(t) \rangle|^2 \equiv \langle A(t) \rangle$. In

¹Equation (2.1) even describes the time evolution of the entire universe.

²It should be noted that time evolution can also be calculated by finding an operator \mathcal{U} and applying it to the state, but in practice such methods are difficult to work with, as they require a diagonalization of the Hamiltonian.

³In many real-world systems, a large number of quantum states are prepared identically, so the main outcome of an experiment is typically the average or its fluctuations.

the density matrix formalism, the measurement value is just the probability of each state times its expectation value, which is $\langle A(t) \rangle = \text{tr}(\rho(t)A)$.

We are free to represent the time-dependent state of the system using whatever formalism is most convenient. These two representations are known as the *Schrödinger* picture and the *Heisenberg* picture respectively (with an intermediate approach termed the *interaction* picture). Using the definition for the expectation value and moving the time dependence onto the operators, Eq. (2.3) can be written equivalently as

$$\dot{A}(t) = \frac{i}{\hbar} [\mathcal{H}, A(t)], \quad (2.4)$$

and therefore we can work with the operators themselves rather than the quantum state in the wavefunction/density matrix. Typically, only a few observables are needed in the context of a given problem, so the computational workload can be drastically reduced simply by changing pictures, as is discussed below.

Up until this point we have not mentioned any particular representation of the Hamiltonian, states, and operators. In technical terms, they are described by a C*-algebra: a complex algebra of continuous linear operators on a complex Hilbert space [53]. In practice—especially in the areas of research where this thesis is concerned—the Hilbert space is discretized and, therefore, operators are represented by complex valued matrices and bras and kets are complex valued vectors. This representation preserves the non-commutativity required by quantum mechanics.

2.2 Many-body Quantum Mechanics

For this work, the focus is on quantum systems with multiple particles. These can be electrons in a metal, photons in free space, or cold atoms in a confining potential well. The formalism of quantum mechanics allows us to treat the myriad of particles and physical processes through a construct known as *creation* and *annihilation* operators. These are operators that can be applied to a quantum state to add or remove particles

with given properties. For example, let us consider a quantum system with a single state. In particular, we focus on fermionic systems. The eigenstates of the system are $|0\rangle$, which is when the system is empty, and $|1\rangle$, which contains a particle. The state of the system can be any superposition of these two states: $|\psi\rangle = a|0\rangle + b|1\rangle$. We can then define the pair of operators c and its Hermitian conjugate c^\dagger as the operators that remove and add a particle to the system respectively. It has the following properties:

$$c^\dagger |0\rangle \rightarrow |1\rangle \quad (2.5a)$$

$$c |1\rangle \rightarrow |0\rangle \quad (2.5b)$$

$$c^\dagger |1\rangle \rightarrow 0 \quad (2.5c)$$

$$c |0\rangle \rightarrow 0. \quad (2.5d)$$

It is important to note that at this point there is no distinction between what type of particles, or even general states, are used in this system, other than that it can only exist in two forms. Nevertheless, this construct allows us to define how we can retrieve information from the configuration. For instance, we can define a number operator $n \equiv c^\dagger c$ whose expectation value, $\langle c^\dagger c \rangle$, is the occupation of the system. In this case, it can be a real value between zero and one.

A rapid increase of complexity and computational requirements manifests itself when expanding the system to include more than a single particle. If we examine a system with two sites, where each site can hold a single particle, then the eigenstates for the system are all the possible products of the single site eigenstates: $|00\rangle$, $|01\rangle$, $|10\rangle$, and $|11\rangle$. The notation $|00\rangle$ is shorthand for $|0\rangle \otimes |0\rangle$, with each number corresponding to a single site that can contain a particle. There are now four of them, so the state of the system requires four complex coefficients to describe it.

Since there are two particle sites in this new system, the creation and annihilation operators need to be expanded to cover all possible eigenbasis. The usual way to do this is to add an index to the operator which relates it to a specific site, so now the basis

for the whole system can be described by a set of c_i and c_i^\dagger operators. Each one acts individually, for example, in the two site system, $c_1^\dagger |00\rangle \rightarrow |10\rangle$, and so on.

Once multiple particles are introduced, it is necessary to distinguish what kind of particles and particle states exist within the system. If we are describing a photon or phonon system, then we must use bosons, whereas if we are working with an electronic system, then fermions must be used. Bosons can share quantum states, whereas the Pauli exclusion principle applies to fermions and only one can occupy a single state. Most importantly, fermions have a property known as exchange antisymmetry, whereby exchanging the order in which these operators are applied will invert the sign. Mathematically, this is a condition on how the operators commute:

$$\{c_i, c_j^\dagger\} = \delta_{ij} \quad (2.6a)$$

$$\{c_i, c_j\} = \{c_i^\dagger, c_j^\dagger\} = 0. \quad (2.6b)$$

Here, the curly brackets, $\{\dots\}$, are the anticommutator $\{A, B\} = AB + BA$. Similarly for bosons, the operators follow the same relationship but with applying the commutator, e.g., $[c_i, c_j^\dagger] = \delta_{ij}$.

At this point, we can continue to expand the system to include a total of N sites, with each site able to hold a single particle. Even though we are describing single sites, this formalism can be expanded to include other quantum numbers by including them under the same index. For example, a system with both spin up and spin down fermions can be modeled with $2N$ spinless sites. Each state on each site can be indexed by the quantity $\tau_i \in \{0, 1\}$, so the entire wavefunction can be written as

$$|\psi\rangle = \sum_{\tau_1, \tau_2, \dots, \tau_N} c_{\tau_1, \tau_2, \dots, \tau_N} |\tau_1, \tau_2, \dots, \tau_N\rangle = \sum_{\boldsymbol{\tau}} c_{\boldsymbol{\tau}} |\boldsymbol{\tau}\rangle. \quad (2.7)$$

Here, the vector $\boldsymbol{\tau}$ goes over every possible combination of states on individual sites, and $c_{\boldsymbol{\tau}}$ are all the coefficients needed to describe a complete state. Now we see where the exponential growth in complexity comes from: every additional site that is added

doubles the number of coefficients needed to describe the state of the composite system. To give an idea of how much information a quantum system like this needs, a system with $N = 32$ sites would require 32 GB of storage to hold one wavefunction. If that were increased to $N = 64$, then 8 EB (exabytes) are required. This 2^N growth in storage requirements quickly becomes unwieldy.

The above values only apply to pure quantum states, and the space required is even larger when working with a mixed state. A density matrix describing an N site system is a 2^N by 2^N complex-valued matrix. Similar limitations apply to the application of an operator to a state, which requires a matrix-vector multiplication or 2^{2N} complex scalar multiplications. Both the space complexity (the amount of memory required to store information about the system) and the time complexity (the amount of time required to perform a calculation) go up exponentially with the size of the system. In addition, these sites typically represent single atomic or molecular states, so even simulating a nanoscale device would require a huge number of them.

However, these limitations only apply if one wants to keep track of the quantum states in their entirety. As will be shown, there are many ways to reduce the computational complexity by limiting the amount of information, restricting to a well-behaved subproblem, or by making approximations within the simulation techniques. Indeed, most of the field of quantum many-body systems is concerned with transforming these problems into ones that are more tractable.

2.2.1 Full Time Evolution

Calculating the time evolution of a quantum system without approximations is a matter of solving the differential equations given by Schrödinger's equation, Eq. (2.1). However, we still have not defined the form of the Hamiltonian \mathcal{H} , the associated c_i^\dagger operators, and the state $|\psi\rangle$ in a way that is suitable for numerical computation.

Since the creation and annihilation operators form a basis set for our system, then the Hamiltonian can be a sum or product of these operators. In the most general form,⁴

$$\mathcal{H} = \sum_{ij} h_{ij} c_i^\dagger c_j + \sum_{ijkl} h'_{ijkl} c_i^\dagger c_j^\dagger c_k^\dagger c_l + \sum_{ijklmn} h''_{ijklmn} c_i^\dagger c_j^\dagger c_k^\dagger c_l^\dagger c_m^\dagger c_n \dots \quad (2.8)$$

Here, the components of each order are written separately in order to distinguish them easily. However, higher order components can specify lower ones as well. For example, it can be seen from the commutation relations that the term specified by h'_{1112} is the same as h_{12} . To specify this most general form for the Hamiltonian completely, a 2^N by 2^N complex matrix is required. Section A.1 details the conversion between the operators and matrix forms via the Jordan-Wigner transform when dealing with fermions.

2.2.2 Realtime Approach

As a first step to reducing the computational complexity, we will first limit ourselves from the Hamiltonian in Eq. (2.8) to a quadratic Hamiltonian of the form

$$\mathcal{H} = \sum_{ij} h_{ij} c_i^\dagger c_j. \quad (2.9)$$

Pauli exclusion is guaranteed by the anticommutation relations but otherwise particles do not interact and the total particle number is conserved. This simplification might seem extreme at first, but nevertheless many interesting physical phenomena can be studied and explained with this type of model. This also provides a natural starting point to start building in higher order effects.⁵

Most, if not all, of the physical observables of interest in this type of system are derived from expectation values of pairs and c_i^\dagger and c_i operators. To simplify the notation, we

⁴ As a matter of simplicity, we have already taken into account that unpaired creation and annihilation operators do not have an effect on the expectation value of observables, and so have removed them from the expression

⁵ And is also the reason why the general Hamiltonian was originally written in the form of Eq. (2.8) as well.

will define the *correlation matrix* as

$$c_{ij}(t) \equiv \text{tr}[\rho(t)c_i^\dagger c_j] = \langle c_i^\dagger c_j \rangle(t). \quad (2.10)$$

As before, the terms of interest are directly related to values in this matrix. For example, the diagonal terms c_{ii} are the onsite occupations of their respective site i . This is useful on its own, but for the Hamiltonian in Eq. (2.9), this matrix uniquely describes the entire state of the system. To see this, we can calculate the time evolution of $\dot{c}_{ij}(t) = \frac{d}{dt} \langle c_i^\dagger c_j \rangle(t)$. Multiplying Eq. (2.3) on the right by $c_i^\dagger c_j$ and substituting \mathcal{H} yields

$$\dot{c}_{ij}(t) = \frac{i}{\hbar} [h, c(t)]_{ij}, \quad (2.11)$$

with the N by N matrix h (with elements h_{ij}) describing the complete Hamiltonian. No other higher-order terms arise in this expression and, therefore, the equations of motion, from Eq. 2.11, form a closed set of differential equations. The correlation matrix can be calculated directly as a function of time without any other information about the state required.

This is important for computational complexity because, for an N site system, both h and c are N by N complex-valued matrices. We now have a polynomial growth (N^2) in the space and time complexity rather than an exponential growth. Where eight sites would be difficult to calculate before, we now have the ability to scale up to thousands or hundreds of thousands of sites, which can reach the scale of nanoscale electronic devices. Of course, this is at the expense of the complete many-body picture.

Since we have reduced the Hamiltonian to the form of Eq. (2.9), it is possible to do a direct diagonalization of the system in a simple manner. The time evolution typically starts from a ground state of the system with the interaction turned off or from a system with different components initially disconnected. The diagonalization involves finding the unitary transformation $b_k = \sum_i U_{ki} c_i$ so that $\mathcal{H} = \sum_k \epsilon_k b_k^\dagger b_k$. U is unitary because $UU^\dagger = I$ and ϵ_k represents the spectrum of energies of \mathcal{H} . With this representation, the ground state correlation matrix can be found by

1. Find the eigenenergies and eigenvectors of h . Since it is a 2D matrix, this process is relatively straightforward for even a large number of sites. Ideally, we want the result in the form that most numerical packages provide: an array of N eigenvalues (ϵ_k) and a 2D matrix of normalized eigenvectors in the same order arranged into the rows or columns (U_{ij}).
2. Populate a correlation matrix in the energy basis. For the ground state (all states with energy less than zero are occupied) populate a matrix m so that $m_{ij} = \delta_{ij}\Theta(-\epsilon_i)$. That is, the diagonal elements have a value of 1 for each corresponding energy below a cutoff energy.
3. Find the site basis correlation matrix by applying $c = U^\dagger m U$ (or $c = U m U^\dagger$ depending on which direction the particular solver finds the eigenvectors).

A similar process can be done to find the state at finite temperature: $m_{ij} = \delta_{ij}f_D(\epsilon_k, \beta, \mu)$, with f_D as the Fermi-Dirac distribution [56, 57]:

$$f_D(\epsilon, \beta, \mu) = \frac{1}{e^{\beta(\epsilon-\mu)} + 1}, \quad (2.12)$$

where β is the inverse temperature $1/k_B T$, and μ is the chemical potential of the reservoir. The constant k_B is the Boltzmann constant, which relates the energy of a given particle to its temperature: $8.617\ 3303(50) \times 10^{-5}$ eV K⁻¹ [52].

The diagonalization yields the energy distribution as a function of the site index, so the density of states is found by expanding to the continuum and performing the derivative $dk/d\epsilon_k$. Alternatively it can be kept in discrete form, which means the density of states is proportional to a sum over delta functions, $\sum_k \delta(\epsilon - \epsilon_k)$. The local density of states (LDOS) is a space-resolved extension of the density of states that weights each state with the wavefunction overlap of a particular site. Each ϵ_k is associated with the k^{th} column vector, Ψ_k , in the eigensolution, so the overlap with site j is $|\langle j | \Psi_k \rangle|^2$, making

the LDOS in the discrete form

$$D(\epsilon) = \sum_k |\langle j | \Psi_k \rangle|^2 \delta(\epsilon - \epsilon_k). \quad (2.13)$$

This only works in this manner if the wavefunctions can be expressed in terms of a linear combination of single site eigenstates.

The diagonalization of the open system Lindblad equation, discussed later in Sec. 2.3.1, is found using the same process. An interacting Hamiltonian can be treated the same way, but the computational complexity of the eigenvalue problem quickly makes it unfeasible for anything but small systems.

As an example, the electronic current through the system can be found without any intermediate calculations. For a closed system, this involves dividing the system into two parts and examining the change in onsite occupation in one half:

$$I(t) = e \dot{N}_{\text{left}} = e \sum_{i \in \text{left}} \dot{c}_{ii}(t), \quad (2.14)$$

where e is the electronic charge $1.602\ 070\ 040(81) \times 10^{-19}$ C [52] and N_{left} is the total number of particles in the left section. Using the expression for the time evolution, this can then be written as

$$I(t) = \frac{e}{\hbar} \sum_{i \in \text{left}} \sum_j 2 \text{Im}[h_{ij} c_{ji}(t)], \quad (2.15)$$

as h and c are both Hermitian matrices.

2.2.3 Mean Field Approximation

Next, a term is included in the Hamiltonian that allows the particles to interact directly with one another. The preferred method for this to separate the fermions into spin up (\uparrow) and spin down (\downarrow) varieties. This is accomplished by adding an additional index to the c_i^\dagger operators: now the basis set is $c_{i\uparrow}^\dagger, c_{i\uparrow}, c_{i\downarrow}^\dagger, c_{i\downarrow}$. For the Hamiltonian, we will add a

term that adds an additional energy, U_i , if the two types are on the same site. This is written as

$$\mathcal{H} = \sum_{ij\sigma} h_{ij\sigma} c_{i\sigma}^\dagger c_{j\sigma} + \sum_i U_i c_{i\uparrow}^\dagger c_{i\uparrow} c_{i\downarrow}^\dagger c_{i\downarrow}. \quad (2.16)$$

Note that there is no interaction between the two species in the first term (the sums over $\sigma \in \{\uparrow, \downarrow\}$ are independent) so this Hamiltonian does not have a “spin flip” mechanism and the number of particles of each type is conserved.

If we calculate the time evolution of the correlation matrix using the same method as the previous section, then the equation of motion becomes

$$\begin{aligned} \dot{c}_{ij\sigma}(t) &= \frac{i}{\hbar} \left(\langle [c_{i\sigma}^\dagger, \mathcal{H}] c_{j\sigma} \rangle + \langle c_{i\sigma}^\dagger [c_{j\sigma}, \mathcal{H}] \rangle \right) \\ &= \frac{i}{\hbar} \left\{ [h, c(t)]_{ij\sigma} - U_i \langle c_{i\uparrow}^\dagger c_{i\uparrow} c_{i\downarrow}^\dagger c_{i\downarrow} \rangle(t) + U_j \langle c_{i\uparrow}^\dagger c_{i\uparrow} c_{j\downarrow}^\dagger c_{j\downarrow} \rangle(t) \right\}. \end{aligned} \quad (2.17)$$

Since the interaction term was added, the time evolution for the correlation matrix no longer forms a closed system of equations. The differential equations now include two-particle correlation terms, which are expectation values of four operators. If we calculated the time evolution of these two-particle correlations, what we would find is that the result depends on three-particle correlations, which, in turn, depend on four-particle correlations, etc. This infinite hierarchy of coupled equations is known as the BBGKY hierarchy (after Bogoliubov [59], Born and Green [60], Kirkwood [61], and Yvon [62]). The inclusion of interacting terms requires more information about higher order correlations and this process continues until the computational complexity is scales the same as the of original density matrix formulation.

Most of the relevant information about the system (particle density, current flow, etc.) is calculated from the single-particle correlations, so the computational complexity can be limited by truncating the equations of motion to only include correlations of order d or less. Expectation values that include more than d operators are approximated by lower order terms. This limits the total computational complexity in time and space to order N^d , so that it remains polynomial rather than exponential.

Use of the Wick decomposition (see Sec. A.2) and assuming the single-particle Hamiltonian is symmetric in spin allows us to rewrite Eq. (2.17) in approximate form:

$$\begin{aligned}\dot{c}_{ij}(t) &= \frac{i}{\hbar} \left\{ [h, c(t)]_{ij} - U_i \langle c_i^\dagger c_i \rangle(t) \langle c_i^\dagger c_j \rangle(t) + U_j \langle c_i^\dagger c_i \rangle(t) \langle c_j^\dagger c_j \rangle(t) \right\} \\ &= \frac{i}{\hbar} \{ [h, c(t)]_{ij} - U_i c_{ii}(t) c_{ij}(t) + U_j c_{ij}(t) c_{jj}(t) \}.\end{aligned}\quad (2.18)$$

At this point, we have recovered the N^2 space and time complexity of the single-particle Hamiltonian. It still forms a set of N^2 coupled differential equations, but this time they are non-linear. For numerical simulation purposes, the non-linear aspect usually matters very little, as the computational cost remains the same as the previous, linear version.

As we will see in Chapter 4, this process can be continued to keep orders higher than mean field. There, the total complexity is kept at N^4 by preserving all two-particle correlations and decomposing the three-particle terms that arose. Our truncation metric is the order of the correlations, which provides a convenient limit to the computational complexity, but is not necessarily the most efficient or accurate approximation, as discussed in Sec. 2.4.

2.3 Electronic Transport

So far the discussion has centered around closed quantum systems: the number of sites has remained finite and the total number of particles in the system are conserved. The system is initially placed into a particular configuration and the time evolution is allowed to proceed while the wavefunction or observables are monitored. However, in this thesis, but we are interested in electronic (and atomic) transport for which this approach has some drawbacks.

The first, and arguably the most important, is that we are usually interested in the steady-state dynamical properties of, e.g., electrons, which are properties on a longer timescale than the response time for a single particle. For instance, if we were to connect

a resistor to a battery, then there is some finite time where the electron flow has started but not yet reached through the whole circuit. However, this happens quickly and what is physically measured is a near-instantaneous transition to constant current flow.

Simulating this current in the long time regime is near impossible using the closed system approach. Any “switching on” of the time evolution results in a decaying transient motion. The simulation of the system must run long enough so that the results reflect the steady-state rather than the transient current. However, a finite system can only time evolve for a finite time before it starts recurrence. As an illustration, if we have N sites representing a particle reservoir and allow each particle to move to an adjacent site in one time unit, then the simulation can only continue for N time units before the reservoir empties and the particles begin to flow back in. This temporary formation of the constant motion solution is known as a quasi-steady state (QSS).

As a result, the size of the system will need to be large, with an associated increase in computational complexity. Additionally, if the Hamiltonian has a slowly varying time-dependent component, then it can be impossible to find the true steady-state, even when examining a non-interacting Hamiltonian. Real devices do not have this problem, as the number of states in, e.g., a battery is extraordinarily large and the recurrence time is correspondingly long.

The solution to this is to revisit our formulation of the time evolution, Eq. (2.3), to represent an open quantum system—that is, a model that allows particles to flow into and out of the system.

2.3.1 Lindblad Equation

The dynamics of an open quantum system are modeled as a smaller system that interacts with a larger, external environment. When combined, these two components time evolution in the usual unitary fashion. If \mathcal{U} is the time evolution operator for the state

of the system and the external environment, then we write the effect on the system as

$$\dot{\rho} = \mathcal{E}(\rho) = \text{tr}_{\text{env}} \left[\mathcal{U}(\rho \otimes \rho_{\text{env}}) \mathcal{U}^\dagger \right], \quad (2.19)$$

where tr_{env} is the partial trace over the environment. The object \mathcal{E} is a superoperator on the density matrix ρ , which is a linear operator that acts on the vector space of linear operators—it takes an operator as input and returns an operator. The commutator of ρ with \mathcal{H} in the canonical time evolution, Eq. (2.3), is another example of a superoperator on ρ .

We can choose an orthonormal basis $|e_k\rangle$ for the state space of the environment and label the initial state by $\rho_{\text{env}} = |e_0\rangle\langle e_0|$. Substituting this into Eq. (2.19) yields

$$\mathcal{E}(\rho) = \sum_k \langle e_k | \left[\mathcal{U}(\rho \otimes |e_0\rangle\langle e_0|) \mathcal{U}^\dagger \right] |e_k\rangle = \sum_k E_k \rho E_k^\dagger, \quad (2.20)$$

with $E_k \equiv \langle e_k | \mathcal{U} | e_0 \rangle$. This expression provides a general open system operator (as a unitary operator does for a closed system); however, we would like a more tractable form that matches reality in specific cases. Ideally, it would provide the following:

1. Trace preserving. The density matrix is coupled to the expectation values, so it is convenient to incorporate normalization into the time evolution.
2. Completely positive. This is a requirement of superoperators on ρ in general, so that probabilities are not less than zero and entanglement entropy is well defined.
3. Incorporates closed-system dynamics. We already know how a system defined by \mathcal{H} evolves in time, so presumably the open system dynamics should occur in addition to those.
4. Continuous time evolution. As with the closed system, the time evolution process is expressed in the form of a differential equation in t .

The solution to these requirements is given by what is known as the Markovian master equation

$$\dot{\rho}(t) = -\frac{i}{\hbar}[\mathcal{H}, \rho(t)] + \sum_k \left(L_k \rho(t) L_k^\dagger - \frac{1}{2} \left\{ L_k^\dagger L_k, \rho(t) \right\} \right). \quad (2.21)$$

The Hamiltonian in this expression still applies to the system,⁶ and the L_k operators are what are known as Lindblad terms, which represent the effect of the environment. In a sense, these are arbitrary, but they can be derived from an explicit representation of the environment through the use of Born and Markov approximations.

We now have access to the long-time dynamics of the system without needing to take into account the recurrence issue from closed systems. For example, if we wish to find the state after a long time and all the transient evolution has passed, $\rho(\infty)$, then we can simply set $\dot{\rho} = 0$ and invert the superoperator on the right side of the expression. If it is too expensive to work with the superoperator directly, then the time evolution can be iterated until it converges to the steady state.

Of particular interest is the master equation in the form

$$\dot{\rho} = -\frac{i}{\hbar}[\mathcal{H}, \rho] + \sum_k \gamma_{k+} \left(c_k^\dagger \rho c_k - \frac{1}{2} \left\{ c_k c_k^\dagger, \rho \right\} \right) + \sum_k \gamma_{k-} \left(c_k \rho c_k^\dagger - \frac{1}{2} \left\{ c_k^\dagger c_k, \rho \right\} \right), \quad (2.22)$$

where the Lindblad operators are the creation and annihilation operators on the system site basis. The term multiplied by γ_{k+} represents the injection of particles at site k with rate γ_{k+} , and similarly the γ_{k-} component represents the removal of particles. This, in effect, allows us to include the particle sources and sinks as something outside of the system. In electronic transport, this equation allows us to specify an “input,” such as a battery, and focus on the simulation of the device response in \mathcal{H} .

Moreover, if the system Hamiltonian \mathcal{H} is non-interacting, then we can follow a similar process as in Sec. 2.2.2 and examine the time evolution of the correlation matrix.

⁶In the most general sense, this Hamiltonian is not necessarily the same as the one with the system decoupled from the environment. However, for the work presented in this thesis this is always the case.

Multiplying Eq. (2.22) on the right by $c_i^\dagger c_j$ and taking the trace yields

$$\dot{c}_{ij}(t) = \frac{i}{\hbar}[h, c(t)]_{ij} + \frac{c_{ij}(t)}{2}(\gamma_{i+} + \gamma_{i-} + \gamma_{j+} + \gamma_{j-}) + \gamma_{i+}\delta_{ij}. \quad (2.23)$$

Like before, setting $\dot{c}_{ij} = 0$ and inverting the right side superoperator (which is now size N^4 rather than 2^{4N} as in the density matrix case) yields the long time solution for the steady state.⁷

2.3.2 Landauer Approach

We have taken some steps in reducing the complexity by using an equation of the form of Eq. (2.22), which eliminates the degrees of freedom of the environment. This section explores a further set of approximations known as the Landauer approach [54].

This approach is fundamentally a viewpoint and comprise a set of physical assumptions on top of the open quantum system formalism, which guide the construction of the model of electron transport. The primary assumptions are the following [55]:

1. There exists an ideal steady state which is said to be stationary and unique. Previously, this was implicitly taken to be true, but here it is explicit.
2. Edges of the device are treated as boundary conditions rather than a coupling to an environment.
3. A mean-field approximation is required. With the master equation, the Hamiltonian and/or Lindblad operators can be many-body operators.
4. A device consists of single-particle channels that are treated independently. The idea is that an incoming particle occupies an energy state in the device, which does not mix with others as it transitions through.

⁷Note that the steady state is not guaranteed to be unique or even to exist for all initial conditions on ρ . However, again, this is true for the work presented in this thesis.

Whether or not these assumptions reflect reality depends strongly on the properties of the device but, as we show in Chapter 3, it is possible to make an explicit connection between this approach and the master equation.

This picture of transport reinforces the idea of quantized conductance. If a device consists of many independent channels with some probability that current will flow through each one, then there must be an amount of current that each channel can sustain (provided the particle does not scatter).⁸ It is defined as $G_0 = e^2/(\pi\hbar)$, where, again, e is the charge of one electron, making the conductance quantum $7.748\ 091\ 7310(18) \times 10^5$ S [52].

In its simplest form, Landauer's formula for the conductance is just the quantum of conductance summed over all the open channels:

$$G(\mu) = G_0 \sum_k M_k(\mu). \quad (2.24)$$

This expression is for conductance at a particular energy μ . This is expanded into a continuous form to be

$$I = \frac{e}{2\pi\hbar} \int_{-\infty}^{\infty} [f_L(\epsilon) - f_R(\epsilon)] \times T(\epsilon) d\epsilon, \quad (2.25)$$

where several components are included: instead of conductance, we are now calculating total current, f_L and f_R are the electronic distributions of the surrounding environment and T is a continuous transmission coefficient.

The typical configuration is shown in Fig. 2.1. The system is divided into a “left” portion where electrons at a higher potential enter the device, a central region with a transmission probability (the section that was modeled with the Hamiltonian in the open system case), and a “right” portion at a lower potential where the electrons exit. These open portions are referred to as the leads of the device. The distribution function, f , can

⁸The quantum of conductance can also be found through a direct application of the Heisenberg uncertainty principle: $\Delta E \Delta t \approx \hbar$, making the appropriate conversions between charge/current to energy/time.

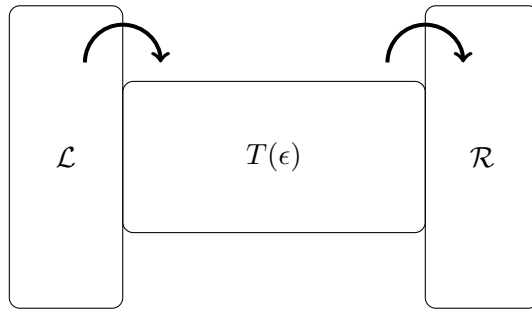


Figure 2.1: Diagram of electron transport in a device. In a typical calculation, the system is divided into electronic reservoirs, \mathcal{L} and \mathcal{R} in the figure, which are the sources and sinks of electronic currents. The remaining component is the system of interest, with a transmission coefficient $T(\epsilon)$ in this case, and is usually treated exactly with a specified Hamiltonian.

be any arbitrary function, but a common practice is to use a Fermi-Dirac distribution, Eq. (2.12). The distributions in Eq. (2.25) are then $f_{L(R)}(\epsilon) = f_D(\epsilon, \beta, \mu_{L(R)})$ with $\mu_L > \mu_R$.

2.3.3 Non-Equilibrium Green's Functions

The expression in Eq. (2.25) is useful for calculating the transport properties of a known or simple transmission function in the ballistic case. However, we would like to be able to relate it to our explicit definition of the Hamiltonian. That is, model the central system explicitly and as exact as possible. To do this, we need the non-equilibrium Green's function (NEGF) approach.

NEGF expands on the Landauer approach (Sec. 2.3.2) by allowing for the inclusion of scattering processes and strong correlations. Apart from the addition of many-body interactions, this formalism makes almost the same set of assumptions as were used in the last chapter. Much work has been put forth in the study of NEGF (see Ref. [58] for a broad reference). However, we will only cover the subset needed for the material in this thesis.

Mathematically, a Green's function of a linear operator \mathcal{L} is any solution of⁹

$$\mathcal{L}(G(t, t')) = -\delta(t - t'). \quad (2.26)$$

The goal of the non-equilibrium problem is to solve for the time dynamics of a system evolving under the Hamiltonian of the form

$$H = h + H'(t) = H_0 + H_i + H'(t). \quad (2.27)$$

H_0 is the single-particle time-independent part of the Hamiltonian that can be solved exactly, H_i is the time-independent part that contains the many-body aspects of the problem, and $H'(t)$ is the time-dependent perturbation that is applied to the system at time t_0 .

The derivation of NEGF is similar to that used in the equilibrium Green's function, so first we will provide a review of the Green's function formalism for an interacting system at equilibrium. Like the correlation matrices, these Green's functions yield important quantities (self-energy, spectral functions, etc.) that we will need for the non-equilibrium case. A number of physical situations are solvable using the equilibrium formalism as a starting point before moving into NEGF.

We expand into the continuous case by working with the field operator $\psi(\mathbf{r}) = \sum_k \langle \mathbf{r} | \phi_k \rangle c_k$, which destroys a particle at position \mathbf{r} . The time evolution in the Heisenberg picture with respect to the time-independent part of Eq. (2.27) is then

$$\psi(\mathbf{r}, t) = e^{iht/\hbar} \psi(\mathbf{r}) e^{-iht/\hbar}. \quad (2.28)$$

The single-particle time-ordered Green's function is defined as

$$G(\mathbf{r}, t, \mathbf{r}', t') = -\frac{i}{\hbar} \left\langle T[\psi(\mathbf{r}, t)\psi^\dagger(\mathbf{r}', t')] \right\rangle, \quad (2.29)$$

⁹The minus sign is a just a convention choice and can be omitted for the same result.

where $T[\dots]$ is the operation that time-orders the field operators. This expression can be generalized to finite-temperature equilibrium situations by using the thermal density matrix in the expectation value.

As it is strongly related to the correlation matrix from above, all measurable quantities are directly related to this Green's function and it encodes the entire state of the system. For example, the particle density is related to the Green's function by $\langle n(x) \rangle = -i\hbar G(\mathbf{r}, t, \mathbf{r}, t^+)$ (with $t^+ = \lim_{\epsilon \rightarrow 0}(t + \epsilon)$). Similar expressions can be found for expectation values of kinetic energy, total energy, etc.

For future reference, we will define four different types of Green's functions:

$$G^r(\mathbf{r}, t, \mathbf{r}', t') = -i\theta(t - t') \left\langle \{\psi(\mathbf{r}, t), \psi^\dagger(\mathbf{r}', t')\} \right\rangle, \quad (2.30a)$$

$$G^a(\mathbf{r}, t, \mathbf{r}', t') = i\theta(t' - t) \left\langle \{\psi(\mathbf{r}, t), \psi^\dagger(\mathbf{r}', t')\} \right\rangle, \quad (2.30b)$$

$$G^<(\mathbf{r}, t, \mathbf{r}', t') = i \left\langle \psi^\dagger(\mathbf{r}', t') \psi(\mathbf{r}, t) \right\rangle, \quad (2.30c)$$

$$G^>(\mathbf{r}, t, \mathbf{r}', t') = -i \left\langle \psi(\mathbf{r}, t) \psi^\dagger(\mathbf{r}', t') \right\rangle. \quad (2.30d)$$

These Green's functions are known as *retarded*, *advanced*, *lesser than*, and *greater than* Green's functions, respectively. They are not linearly independent and they obey the relationship $G^r - G^a = G^> - G^<$.

We can find the equation of motion for the Green's function by differentiating both sides of Eq. (2.29) and using the commutation relations of the field operators:

$$\begin{aligned} \left(i\hbar \frac{d}{dt_1} + \frac{\hbar^2}{2m} \nabla_1^2 \right) G(\mathbf{r}_1, t_1, \mathbf{r}'_1, t'_1) &= \delta(\mathbf{r}_1 - \mathbf{r}'_1) \delta(t_1 - t'_1) \\ &- i \int d\mathbf{r} w(\mathbf{r}_1 - \mathbf{r}) G_2(\mathbf{r}, t_1, \mathbf{r}_1, t_1; \mathbf{r}, t'_1, \mathbf{r}'_1, t'_1). \end{aligned} \quad (2.31)$$

G_2 is the two-particle Green's function. In order to close the system of equations, we would need to solve the equation of motion for G_2 , which would have a dependence on G_3 , the three-particle Green's function, which depends on the four-particle and so on until infinite order. This problem arises from the interaction term(s) in the Hamiltonian and

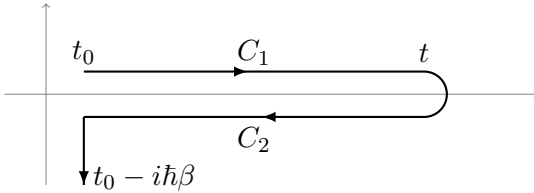


Figure 2.2: Time contour in complex plane. This contour is used to evaluate expectation values at time t from some initial condition specified at t_0 , with an additional propagation in the complex time direction to account for finite temperatures.

is the same hierarchy problem as discussed earlier in Sec. 2.2.3: if it was only comprised of single particle terms then the higher order Green's functions could be written in terms of products of two-particle functions.

To manage the infinite number of Green's functions, the typical approach is to put the interaction effects of all particles into a quantity known as the irreducible self-energy, represented by Σ . With some Fourier transforms, we end up with a much more tractable expression for the Green's function:

$$G(k, \omega) = G_0(k, \omega) + G_0(k, \omega)\Sigma(k, \omega)G(k, \omega), \quad (2.32)$$

where G_0 is the free particle Green's function. With this equation, we can write the Green's function as

$$G(k, \omega) = \frac{1}{\omega - \epsilon_k - \Sigma(k, \omega)}. \quad (2.33)$$

Notice that the self-energy term has the effect of moving the pole to a different energy away from ϵ_k and the problem has changed from finding the full Green's function to finding an expression for the self energy. In practice, this term is found by selecting the most relevant terms from a perturbation expansion for G , usually aided by drawing Feynman diagrams. These components we have now are all that is needed for the non-equilibrium formalism. More details on the mathematical derivation can be found in Refs. [55, 58, 63].

Continuing on to the non-equilibrium case, the system will often not return to initial state for asymptotically large times, so we must remove any references to $\pm\infty$. Before, it was a matter of moving t_0 to $-\infty$ and removing some of the complexity of our derivation, but now it must be taken into account. This general formulation of the theory is slightly more complicated than the equilibrium case, but it still bears a close resemblance to its predecessor.

The largest difference in the non-equilibrium case is that the Green's functions are now defined on a time *contour* rather just along the real time axis. That is, we are expanding time to the complex plane, where the many-body perturbation can be applied. That also means we must define a contour ordering operator $T_C[\dots]$ that orders the field operators on the contour. For shorthand notation, we will use $(1) \equiv (\mathbf{r}_1, \tau_1)$, with τ_1 being a point in the complex time plane. We can then write our contour-ordered Green's function as (with close similarity to Eq. (2.29))

$$G(1, 1') \equiv -i \left\langle T_C[\psi(1)\psi^\dagger(1')] \right\rangle. \quad (2.34)$$

(In these sections, we set $\hbar = 1$ to simplify notation.) Figure 2.2 shows the contour used in the non-equilibrium case. It starts at initial time t_0 (which takes into account the initial correlations of our system) and runs along the real axis to t and back. It is then continued in the imaginary time direction for finite temperatures.

Notice that since we have two time variables in our expression for G , and the contour in Fig. 2.2 has two branches labeled as C_1 (going to the right) and C_2 (going to the left), there are four possibilities for the form G takes:

$$G(1, 1') = \begin{cases} G^C(1, 1') & t_1, t_{1'} \in C_1 \\ G^>(1, 1') & t_1 \in C_2, t_{1'} \in C_1 \\ G^<(1, 1') & t_1 \in C_1, t_{1'} \in C_2 \\ G^{\bar{C}}(1, 1') & t_1, t_{1'} \in C_2 \end{cases}. \quad (2.35)$$

G^C is the causal or time-ordered Green's function as defined in Eq. (2.29), $G^<$ and $G^>$ are the lesser and greater Green's functions from Eq. (2.30c) and Eq. (2.30d), and $G^{\bar{C}}$ is the anti-time-ordered Green's function (the time ordering operation has the times reversed). Once again, there are only three linearly independent functions, as we have the relationship $G^C + G^{\bar{C}} = G^< + G^>$. We can recover expressions for the other two Green's functions via a linear combination of the lesser and greater functions:

$$G^r(1, 1') = \theta(t_1 - t_{1'})[G^>(1, 1') - G^<(1, 1')] \quad (2.36a)$$

$$G^a(1, 1') = \theta(t_{1'} - t_1)[G^<(1, 1') - G^>(1, 1')] \quad (2.36b)$$

We still need to transform our solution in order to properly perform a many-body perturbation, meaning that we need to separate out the terms which relate to h into the H_0 terms (single-particle) and H_i terms (many-body) as defined in Eq. (2.27). The details of this transformation are lengthy and can be found in Ref. [64], so we will just state the final result:

$$G(1, 1') = -i \frac{\langle T_C[S_C^i S_{C'}' \psi(1) \psi^\dagger(1')]\rangle_0}{\langle T_C[S_C^i S_{C'}']\rangle_0}. \quad (2.37)$$

The expectation value is taken with respect to the ground state of the non-interacting part of the Hamiltonian H_0 . The S values are contour integrals over the other parts of the Hamiltonian and are defined as

$$\begin{aligned} S_{C'}' &= \exp \left[-i \int_{C'} d\tau H_{H_0}'(\tau) \right] \\ S_C^i &= \exp \left[-i \int_C d\tau H_{H_0}^i(\tau) \right] \end{aligned} \quad (2.38)$$

C is the whole contour as shown in Fig. 2.2, while C' is just the part of the contour that goes from t_0 to t and closes back at t_0 .

Equation (2.38) is exact for any specified Hamiltonian and all time dependence is governed by the solvable part of the Hamiltonian H_0 . This means the density matrix is quadratic (and is simply given as proportional to $\exp(-\beta H_0)$) so Wick's theorem applies and we can construct Feynman diagrams in the non-equilibrium case as well. As in the

equilibrium case, the denominator cancels the disconnected diagrams and we can reason about which terms of the perturbation expansion are the most important. The equilibrium and non-equilibrium theories are thus structurally equivalent with a replacement of the real axis integrals with contour integrals.

Since the contour-ordered Green's function has the same perturbation expansion as the equilibrium formalism, we can make the same construction as in the previous section and assume that a self-energy functional can be defined such that it encapsulates the many-body effects of the system. From that, we create a similar Dyson equation to the equilibrium case:

$$\begin{aligned} G(1, 1') = & G_0(1, 1') + \int d^3x_2 \int_C d\tau_2 G_0(1, 2)U(2)G(2, 1') \\ & + \int d^3x_2 \int d^3x_3 \int_C d\tau_2 \int_C d\tau_3 G_0(1, 2)\Sigma(2, 3)G(3, 1'). \end{aligned} \quad (2.39)$$

We have implicitly made the assumption that the non-equilibrium term in the Hamiltonian can be represented by a one-body external potential U . An example relating this NEGF approach to Landauer is in Sec. A.6.2.

This Dyson expression is the general relationship between the orders of the Green's functions and is consequentially used to find the equations of motion for the four other types. This is the point where the application of this method becomes difficult: the solution requires the evaluation of a two-time integral to include the many-body interaction. The numerical integral carries with it a high computational cost, with time complexity scaling as the number of timesteps squared. However, the Markovian approach, discussed in Sec. 2.3.1, comprises a single time integral and scales linearly with the number of timesteps. In Chapters 5 and 6, we make the explicit connection between these two formalisms.

2.4 tDMRG/MPS

Section 2.2 provides a way to build numerically (and sometimes analytically) tractable expressions for the time evolution of a system. However, it assumes that the states of the system are close to a thermal distribution of the many-body system and there is no guarantee that this is the case. Depending on how the interactions are applied, the system can be in a much different state and the error introduced in the Wick approximation can be large. Additionally, there is no method for finding the magnitude of the error introduced without performing a higher order calculation, which might be infeasible given a large enough N .

An alternative method to calculating the time evolution is known as time-dependent matrix renormalization group (tDMRG). tDMRG provides a “numerically exact” solution to the quantum many-body problem for certain classes of systems, meaning that the error has a known magnitude and is controllable. This method allows for a calculation to an arbitrary accuracy while still providing a polynomial growth in the computational complexity. This technique is equivalent to the matrix product states (MPS) based time-evolving block decimation.¹⁰

In order to understand how these schemes work, following Ref. [66], we need to rework the representation of the general wavefunction from Eq. (2.7): $|\psi\rangle = \sum_{\tau} c_{\tau} |\tau\rangle$. The c_{τ} set of coefficients has N indices, one for each site in the system. The MPS formalism represents this object as an N index tensor. Pictorially, $|\psi\rangle$ looks like

$$|\psi\rangle \equiv \boxed{\text{---}}^{\tau_1} \text{---} \text{---} \text{---} \text{---} \text{---} \text{---} \text{---} \text{---} \text{---}^{\tau_N}. \quad (2.40)$$

The tensor is represented by the box and each one of the “legs” is an index, so an N dimensional tensor has N legs. This tensor network method provides a convenient way to

¹⁰It is a quirk of history that there are two formalisms that describe the same thing. DMRG was originally invented in 1992 and shown to work without a rigorous mechanistic insight. It wasn’t until 2004 that MPS was discovered that the insight as to why it did not fail, as other renormalization schemes did, was systematically explored [65].

describe tensors as well as operations between them. For example, a vector-vector inner product is . Each vector has one index (represented by the line coming out of each box) and connecting them together is a contraction over that index (performing the product). There are no free legs in the result so it is a scalar. Similarly, a matrix-vector product is , with the free index meaning that the result is a vector.

Under this formalism, the c_{τ} tensor is the fundamental object: it contains the information about the state of the entire system and the time evolution of system observables are calculated from it. Any general operator that acts on the system can be expressed as

$$\mathcal{O} = \sum_{\tau\tau'} c_{\tau\tau'} |\tau\rangle\langle\tau'| \equiv \begin{array}{c} \tau_1 \quad \dots \quad \tau_N \\ \hline | & | & | & | & | & | & | & | \\ \tau'_1 & & & & & & & \tau'_N \end{array}. \quad (2.41)$$

For the operator, there are twice as many free indices, and it is convenient to separate them into “input” and “output” sides in this picture representation. Applying the operator to the state can then be represented by

$$\mathcal{O} |\psi\rangle \equiv \begin{array}{c} \tau_1 \quad \dots \quad \tau_N \\ \hline | & | & | & | & | & | & | & | \\ \tau'_1 & & & & & & & \tau'_N \end{array} \downarrow \begin{array}{c} \tau_1 \quad \dots \quad \tau_N \\ \hline | & | & | & | & | & | & | & | \\ \tau'_1 & & & & & & & \tau'_N \end{array} \Rightarrow |\psi'\rangle \quad (2.42)$$

When the operator is applied to the state, all the internal indices that match are contracted and the resulting object is a new N index tensor. The complex conjugate or bra state is represented by changing the side that the indices are coming out of. For instance, the normalization condition on a wavefunction is shown as

$$\langle\psi|\psi\rangle \equiv \begin{array}{c} \text{---} \\ \hline | & | & | & | & | & | & | & | \\ \text{---} \end{array} = 1. \quad (2.43)$$

At this point the formalism is largely the same as how it was originally introduced in previous sections. We have shifted around the representation of the states and operators slightly, but it is still fundamentally the same concept. The advantage here comes from the fact that we can easily see that we can change the representation of the state to

$$|\psi\rangle \equiv \begin{array}{cccccccccc} & \tau_1 & & & & & & & & \tau_N \\ & \square \end{array}. \quad (2.44)$$

So now instead of a single N index tensor, we have factored the wavefunction into the product of N tensors with three indices each. Every interior connection is a matrix multiplication, making the wavefunction

$$|\psi\rangle = \sum_{\tau_1, \tau_2, \dots, \tau_N} M^{\tau_1} M^{\tau_2} \dots M^{\tau_N} |\tau_1, \tau_2, \dots, \tau_N\rangle, \quad (2.45)$$

where each M is a two dimensional matrix. If we were to factor an arbitrary state into this form, then we would not gain anything in terms of space complexity. However, if the state were close to what is known as a product state, then the maximum dimension, χ , of each matrix M can be limited to something much smaller than that needed for an arbitrary state. For example, the vacuum state is an eigenstate of the system and so to represent that in this form, each M only needs to be size one by one. There are N total matrices with an index that can go between d values, so the total space complexity is Nd to hold the state, whereas the original tensor needs d^N terms to represent the same thing. Especially when working with states that are near product states (as time evolution processes tend to provide), this representation efficiently captures the state.

By decomposing the state into matrices that are indexed on individual sites, we are imposing a notion of locality onto the wavefunction representation. The states that are most efficiently represented in matrix product form are those that are lacking a excess of entanglement. We can still use this representation to examine systems where correlations develop (and indeed it would not be very useful if that were not the case) but the underlying assumption is that they are limited and do not grow exponentially.

Therefore, we can limit χ to a reasonable value, one that still accurately represents the state but needs much less space to store.

This is only half the picture, however. The application of an arbitrary operator as shown in Eq. (2.41) can mix up all the indices and generate correlations, of which will factor into an inefficient form. The solution to this is to impose the same notion of locality onto the operator representation as well:

$$\mathcal{O} \equiv \begin{array}{ccccccccccccc} & \tau_1 & & & & & & & & & & & \tau_N \\ \textcircled{O} = & \square \\ & \tau'_1 & & & & & & & & & & & \tau'_N \end{array}, \quad (2.46)$$

or with using products of matrices,

$$\mathcal{O} = \sum_{\substack{\tau_1, \tau_2, \dots, \tau_N \\ \tau'_1, \tau'_2, \dots, \tau'_N}} W^{\tau_1, \tau'_1} W^{\tau_2, \tau'_2} \dots W^{\tau_N, \tau'_N} |\tau_1, \tau_2, \dots, \tau_N\rangle \langle \tau'_1, \tau'_2, \dots, \tau'_N|. \quad (2.47)$$

Once again, any arbitrary operator would not decompose into this form efficiently, but if we limit ourselves to a subset of local or “mostly local” operators then this remains an efficient form. More importantly, applying an operator to a state means a contraction only along one index for each lattice site, meaning that the operator can be applied efficiently as a smaller matrix product for each site rather than a large operator over all indices of the system. This operation is then order $Nd\chi^2$ time complexity to perform, rather than d^{2N} . We have again limited the computation to a polynomial rather than exponential execution time.

A time evolution operator that is completely factorizable into this form is not particularly interesting on its own, as it would mean that each of the sites is effectively non-interacting. However, we can get close to this form by working with operators that we can factor into matrices that involve few adjacent sites. For this, we introduce the complete time evolution operator for a given Hamiltonian.

If we integrate both sides of Eq. (2.1), then the general form for the time evolution operator—that is, the operator $\mathcal{U}(t)$ that brings the wavefunction from $|\psi(0)\rangle$ to $|\psi(t)\rangle$ —is

$$\mathcal{U}(t) = e^{-i\mathcal{H}t/\hbar}. \quad (2.48)$$

This expression is a matrix exponential of the complete Hamiltonian, and is therefore difficult to calculate. In order to make it more tractable, we will focus on a class of Hamiltonians that describe a one-dimensional lattice with a many-body interaction term. As before, the general form for \mathcal{H} is then

$$\mathcal{H} = \sum_{\{i,j\}\sigma} h_{ij\sigma} c_{i\sigma}^\dagger c_{j\sigma} + \sum_i U_i c_{i\uparrow}^\dagger c_{i\uparrow} c_{i\downarrow}^\dagger c_{i\downarrow}, \quad (2.49)$$

where the curly brackets indicate a sum over nearest neighbors. With this form, particles can move between adjacent sites and develop entanglement between them, but the only way one can get from one end to another is to go through all the intermediate sites.

This Hamiltonian allows us to perform a Suzuki-Trotter (ST) expansion [67] on the exponential time evolution operator. An ST expansion is similar to a series expansion except that the norm is conserved and the resulting operators are unitary, leading to a minimization of the accumulation of error. We first break the Hamiltonian in Eq. (2.49) into two parts, $\mathcal{H} = \mathcal{H}_{\text{odd}} + \mathcal{H}_{\text{even}}$, with

$$\mathcal{H}_{\text{odd}} = \sum_{i \text{ odd}} \left(\sum_{\sigma} h_{i,i+1,\sigma} c_{i\sigma}^\dagger c_{i+1\sigma} + U_i c_{i\uparrow}^\dagger c_{i\uparrow} c_{i\downarrow}^\dagger c_{i\downarrow} \right) \quad (2.50a)$$

$$\mathcal{H}_{\text{even}} = \sum_{i \text{ even}} \left(\sum_{\sigma} h_{i,i+1,\sigma} c_{i\sigma}^\dagger c_{i+1\sigma} + U_i c_{i\uparrow}^\dagger c_{i\uparrow} c_{i\downarrow}^\dagger c_{i\downarrow} \right). \quad (2.50b)$$

Then, for a small timestep δ , the time evolution operator can be approximated by

$$\mathcal{U}(\delta) = e^{-i(\mathcal{H}_{\text{odd}} + \mathcal{H}_{\text{even}})\delta/\hbar} \approx e^{-i\mathcal{H}_{\text{odd}}\delta/(2\hbar)} e^{-i\mathcal{H}_{\text{even}}\delta/\hbar} e^{-i\mathcal{H}_{\text{odd}}\delta/(2\hbar)}. \quad (2.51)$$

This approximation becomes exact in the limit of small time steps, $\mathcal{U}(t) = \lim_{\delta \rightarrow 0} \mathcal{U}(\delta)^{t/\delta}$, so the general method of time evolving the state is to choose a sufficiently small δ and

then iteratively evolve forward in time. All of the operators in each of \mathcal{H}_{odd} and $\mathcal{H}_{\text{even}}$ commute with each other, so they can be further broken down into single operators acting on pairs of sites. Graphically, we have decomposed our operator into the form

$$\mathcal{U}(\delta) \equiv \begin{array}{c} \tau_1 \\ \vdots \\ \text{---} \\ \vdots \\ \tau_N \end{array} \quad \begin{array}{c} \tau'_1 \\ \vdots \\ \text{---} \\ \vdots \\ \tau'_N \end{array} = \begin{array}{ccccc} & & & & \\ \text{---} & \text{---} & \text{---} & \text{---} & \text{---} \\ \text{---} & \text{---} & \text{---} & \text{---} & \text{---} \\ \text{---} & \text{---} & \text{---} & \text{---} & \text{---} \\ \text{---} & \text{---} & \text{---} & \text{---} & \text{---} \\ \text{---} & \text{---} & \text{---} & \text{---} & \text{---} \end{array} . \quad (2.52)$$

Each block in this representation takes in two adjacent lattice sites and performs the infinitesimal time evolution step, which is then fed forward to the other set of adjacent sites and so forth.

At this point, the time evolution operator is not fully decomposed into MPO form, so when a block is applied to the state it merges the two adjacent matrices into a single three-index tensor, which then must be re-decomposed into the MPS in order to keep efficiently storing the state and applying the subsequent operators:

$$\begin{array}{c} \tau_2 \quad \tau_3 \\ \vdots \\ \text{---} \\ \vdots \\ \tau_2 \quad \tau_3 \end{array} \Rightarrow \begin{array}{c} \tau_2 \quad \tau_3 \\ \vdots \\ \text{---} \\ \vdots \\ \tau_2 \quad \tau_3 \end{array} \Rightarrow \begin{array}{c} \tau_2 \quad \tau_3 \\ \vdots \\ \text{---} \\ \vdots \\ \tau_2 \quad \tau_3 \end{array} . \quad (2.53)$$

The application of the operator increases the dimension of M from χ to $d^2\chi$, so the size must be reduced to keep within an imposed limit. To do this, we must truncate the local Hilbert space in a manner that minimizes the error. First, the new matrix L , after applying a time evolution block, W , is

$$L_{\alpha\beta}^{\tau_i, \tau_{i+1}} = \sum_{\tau'_i \tau'_{i+1} \gamma} M_{\alpha\gamma}^{\tau'_i} M_{\gamma\beta}^{\tau'_{i+1}} W_{\tau'_i \tau'_{i+1}}^{\tau_i \tau_{i+1}} . \quad (2.54)$$

To return L into a local form, a singular value decomposition (SVD) is performed to factorize the matrix. The indices α and β in the expression for L continue on to the rest

of the MPS and the τ indices remain free, so the SVD is done to each of d^2 combinations over τ . The SVD provides

$$L_{\alpha\beta}^{\tau_i, \tau_{i+1}} \rightarrow \sum_{\gamma} U_{\alpha\gamma}^{\tau_i} \lambda_{\gamma} (V^{\dagger})_{\gamma\beta}^{\tau_{i+1}} = \sum_{\gamma} M'_{\alpha\gamma}^{\tau_i} M'_{\gamma\beta}^{\tau_{i+1}}, \quad (2.55)$$

where the new matrices M' are $M'_{\alpha\gamma}^{\tau_i} = U_{\alpha\gamma}^{\tau_i} \sqrt{\lambda_{\gamma}}$ and $M'_{\gamma\beta}^{\tau_{i+1}} = (V^{\dagger})_{\gamma\beta}^{\tau_{i+1}} \sqrt{\lambda_{\gamma}}$. The SVD is exact for a given matrix L , so we still need to truncate the Hilbert space to keep the state from growing on each application of the time evolution operator and time to perform this operation scales as $Nd^2\chi^3$. The decomposition provides a way to do this, as the values, λ , found during the process are what is known as Schmidt coefficients [68].

These coefficients provide a well-defined measure of the degree of quantum entanglement between the two halves of the system: site i and everything to the left and site $i+1$ plus everything to the right. More specifically, the von Neumann entropy [68] between these two halves, $-\sum_{\gamma} |\lambda_{\gamma}|^2 \log |\lambda_{\gamma}|^2$, is zero only if the two sides are in a product state. The MPS representation of the wavefunction has the least amount of computational complexity for low quantum entanglement, so essentially the values of λ provide a measure of which states to include such that we are using the available space most efficiently.

Since the index γ is internal to the decomposition in Eq. (2.55), we are free to choose whatever dimension for it that we would like, which, in turn, alters the size of the new M' matrices. In order to retain the exact decomposition, the dimension of γ would need to be the minimum of the dimension of α and β . However, with this approximation we can truncate the sum over γ to include the most important terms. Typically, the process involves sorting λ in decreasing order, then keeping the terms that are greater than some small cutoff value, ϵ , up to a maximum of χ terms.¹¹

We now have three controllable sources of error that we can use to converge our final solution:

¹¹An important component to keep in mind here is that the truncation of the local Hilbert space destroys the normalization, so that also needs to be accounted for at some point during these operations.

1. δ , the time difference taken for each forward time step. The ST expansion is exact for $\delta \rightarrow 0$, so this needs to be taken as small as possible. Since the time evolution operator is applied sequentially, the time complexity grows as $1/\delta$. The difference in space complexity is negligible because typically only information on certain observables is stored with each time step rather than the a complete state.
2. ϵ , the cutoff value for Hilbert space truncation. This is included to keep the Hilbert space from immediately growing exponentially and saturating the number of states. It is usually set somewhere on the order of 10^{-9} and adjusted to confirm convergence on the other two terms. The computational complexity of this depends on the specific details of the system and how quickly the correlations can grow.
3. χ , the maximum number of states kept per site. The larger this value is, the closer to the exact solution this representation becomes. However, this parameter also carries with it the highest computational penalty. The space complexity for storing the state is $Nd\chi^2$, the time to apply a time evolution step and the factorization component grows as $Nd^2\chi^3$. For most types of one-dimensional systems, the value for χ is somewhere around 500 to 5000 and it is typically used as the main convergence parameter.

Modification of these parameters and monitoring the error allows us to find the calculated dynamics to an arbitrary degree of precision, without an exponential growth in the computational complexity.

Following the same method, the ground state of a many-body system can be found through an imaginary time evolution: applying $\mathcal{U}(-i\hbar\tau) = e^{-\mathcal{H}\tau}$ iteratively (with small τ and normalization) will drive the system towards a global ground state. All of the eigenstates decay proportionally to their eigenvalue, so the lowest one eventually dominates. In practice, it may be more efficient or stable to use a standard DMRG approach, rather than imaginary time evolution, but the basic concepts remain the same.

2.5 Conclusion

The toolbox for modern theoretical work in physics is enormous. In this Chapter (and the associated Appendices), we provided an “end-to-end” introduction to the mathematical concepts used in this thesis. That is, starting from fundamental concepts and building out to the latest work.

Chapter 3: Energy-resolved Atomic Scanning Probe

The time dynamics of quantum systems are naturally connected to the concept of a density of states. In non-interacting systems, it defines the energy occupation and distribution of particles. When the system is out of equilibrium, it determines what portion of the system is available for transport, as in the Landauer and NEGF formalism discussed in Chapter 2. In this Chapter, we extend this concept to all interacting systems—even those that do not have well-defined quasi-particles—and discuss an operational definition of the local density of states, as defined by Eq. (2.13). This Chapter contains work performed in collaboration with Chih-Chun Chien and Massimiliano Di Ventra.

3.1 Introduction

The density of states is a concept that permeates all of physics, from enabling the description of the fundamental phases of matter to quantifying surface features and defects. The density of states, however, cannot generally be defined for many-body systems, except when, e.g., quasi-particles emerge from the underlying interactions. Here, we give an operational definition of the local density of states for both interacting and non-interacting systems: When a steady-state current of particles—electrons, atoms, etc.—can be sustained between the many-body system of interest, \mathcal{S} , and a narrow energy band of non-interacting states, the probe \mathcal{P} , this indicates that \mathcal{S} supports an infinite reservoir

of particles at that energy, i.e., it has a finite density of states. We demonstrate that ultra-cold atomic lattices—which are increasingly employed in the simulation of many-body phenomena [36, 69–72]—are a natural platform for implementing this concept. Using this operational definition, we elucidate puzzling features in interaction-induced transport and visualize the spatial dependence of the atom density in inhomogeneous, interacting lattices.

The scanning tunneling and atomic force microscopes are arguably the most versatile instruments for probing materials, molecules, structures, and devices. From imaging surface defects to probing local electronic structure to testing novel devices, they have given the means to comprehend structures and behavior at their most basic level and with minimal disturbance. Despite the level of detail and information provided by these instruments, many phenomena have proven resistant to quantitative theoretical interpretation and modeling. Increasingly, the use of tunable systems to mimic, e.g., condensed matter systems has been used to probe physical behavior in a way not possible with traditional techniques. In this direction, recent experimental work demonstrated the expansion of an atomic cloud [73], transport of quantum correlations and phase coherence [74], and the presence of quantum effects in neutral matter transport [27, 32]. This approach holds great promise in advancing our understanding of the natural world, especially many-body and out-of-equilibrium behavior.

3.2 Model

In this Chapter, we give the local density of states (LDOS) an operational definition in terms of steady-state particle currents. The basic premise is that for a system to sustain a steady-state current into a narrow energy reservoir, it must have a finite density of states at that energy. We show how to implement this definition and apply it to many-body systems. As we seek to harness and control quantum behavior for a new generation of technologies, such as quantum computers, spintronic devices, and beyond, this approach

to quantifying physical phenomena will yield an unprecedented level of detail and help in determining the underlying theoretical description of many strongly interacting systems.

We start by recalling the operation of the scanning tunneling microscope (STM) to measure the LDOS, $D(\mu)$, at frequency offset μ , in some region of a surface. For a typical measurement, the tip distance is held constant while the sample bias, $-V$, is changed, leading to a steady-state current given by [75, 76]

$$I \approx I_0 \int_{-eV/\hbar}^0 D(\omega) d\omega. \quad (3.1)$$

The LDOS is found from the differential conductance,

$$D(\mu) \propto \left. \frac{dI}{dV} \right|_{eV/\hbar=\mu}. \quad (3.2)$$

At small bias—or when the system is well-described by non-interacting electrons—this gives an accurate depiction of the native state at the surface.

When the system has strong many-body interactions, such as a poorly screened electronic impurity, the applied bias will disturb the natural state of the surface by disrupting the nearby electron density. This effect can be limited, however, by an alternative setup that uses a narrow band probe, \mathcal{P} , that scans in energy, rather than increasing an applied bias, to interrogate the many-body system, \mathcal{S} . In this setup, the current into a narrow reservoir of bandwidth $4\omega_{\mathcal{P}}$ at a frequency offset μ is proportional to the LDOS,

$$I \approx -e\omega_{\mathcal{P}} \int_{\mu-2\omega_{\mathcal{P}}}^{\mu+2\omega_{\mathcal{P}}} D(\omega) d\omega \approx -4e\omega_{\mathcal{P}}^2 D(\mu) \quad (3.3)$$

so long as $\omega_{\mathcal{P}}$ is small relative to variations of $D(\omega)$. Both empty and filled states can be probed in this way by changing the filling of \mathcal{P} . This setup requires tunability of \mathcal{P} : Its chemical potential, occupation, bandwidth/hopping, and contact magnitude/location with \mathcal{S} need to be modifiable without compromising its non-interacting behavior. In other words, this setup may find its realization with the capabilities provided by

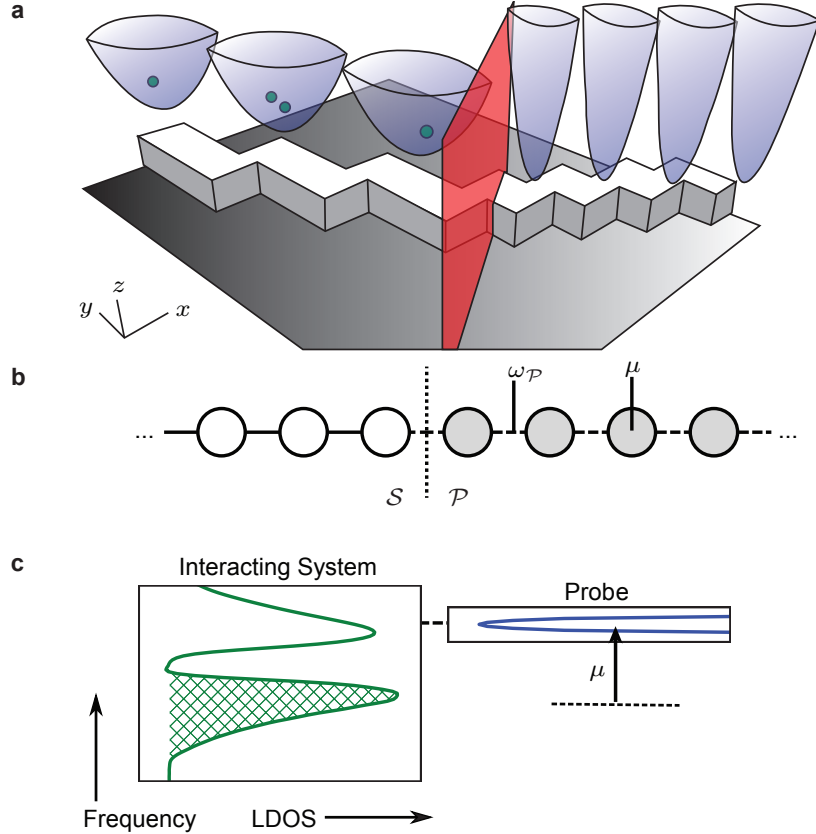


Figure 3.1: Energy-resolved atomic scanning probe. To measure the many-body LDOS, an interacting system, \mathcal{S} , is placed in contact with a non-interacting, narrow band probe, \mathcal{P} . (a) The cold-atom traps are fabricated via a controlled geometry of patterned magnets, which determine spatially-inhomogeneous coupling rates and trapping frequencies. A laser sheet is initially present to prevent the flow of atoms from \mathcal{S} to \mathcal{P} until a measurement is performed. (b) This system is modeled by a 1D lattice with inhomogeneous hopping rates and onsite frequencies in \mathcal{S} and \mathcal{P} . (c) A representation of the setup in frequency space shows narrower range of frequencies and offset of the probe.

ultra-cold atoms in artificial lattice potentials. A schematic of a magnetically trapped implementation of this setup is shown in Fig. 3.1.

3.3 Thin Band Probe

The Hamiltonian, H , for this setup is

$$H_S + H_C - \hbar\omega_P \sum_{i \in \mathcal{P}} (c_i^\dagger c_{i+1} + \text{h.c.}) + \hbar\mu \sum_{i \in \mathcal{P}} c_i^\dagger c_i, \quad (3.4)$$

where ω_P and μ are the hopping and *relative* onsite frequencies respectively (i.e., the trapping frequencies for a cold-atom system, which can be controlled via magnetic potentials) and c_i^\dagger (c_i) are the creation (annihilation) operators of site i . H_S is the many-body Hamiltonian of \mathcal{S} . H_C is the contact Hamiltonian between \mathcal{S} and \mathcal{P} , which we also take to having hopping frequency ω_P , which gives a weak contact to a narrow band.

A laser sheet prevents contact between \mathcal{S} and \mathcal{P} while they are loaded with atoms and cooled to their independent ground states. One can also excite \mathcal{S} by a quench or some other process; the operational definition of the LDOS also extends its applicability to nonequilibrium conditions, in addition to many-body systems. At $t = 0$, the sheet is removed. Then the composite system evolves, giving rise to the current I , which yields the LDOS at frequency μ according to Eq. (3.3). The measurement is repeated for each μ of interest.

As noted above, the experimental realization of this approach requires tunability of the hopping frequencies (the probe bandwidth) and the onsite frequencies (the probe offset), among other parameters. The trap depth and spacing controls the hopping and this can be tuned via the magnitude of the trapping potential. The onsite frequency is related to the ground state of each well, which can be modified by controlling the shape of the potential in each well. This potential can be created by atom chips with magnetic fields generated by patterned circuits of magnetic materials [77–80] or through spatial light modulation (SLM) techniques [81–83], as illustrated in Fig. 3.1. In \mathcal{S} , the interactions can be controlled by using a Feshbach resonance [84] to alter the scattering length, allowing for simulation of different types of many-body systems, such as strength of interactions and spatial dependence. By engineering a series of magnetic potentials

with differing onsite energies and contact locations, one can measure the LDOS as a function of frequency at any location within \mathcal{S} .

With this method, we examine a system of interest with Hamiltonian

$$H_{\mathcal{S}} = -\hbar\omega_{\mathcal{S}} \sum_{i \in \mathcal{S}, \sigma} (c_{i,\sigma}^\dagger c_{i+1,\sigma} + \text{h.c.}) + \hbar \sum_{i \in \mathcal{S}} U_i n_{i,\uparrow} n_{i,\downarrow}, \quad (3.5)$$

where $\omega_{\mathcal{S}}$ is the characteristic tunneling frequency, $n_{i,\sigma} = c_{i,\sigma}^\dagger c_{i,\sigma}$ is the number operator, and U_i is the interaction frequency. The two components may refer to the spins of electrons or internal states of ultracold atoms. When inter-spin interactions are present, $H_{\mathcal{P}}$ is expanded in a similar manner to include spin. For numerical calculations, we use $\omega_{\mathcal{S}} = 1$ kHz, a typical cold-atom tunneling frequency [72].

We first examine a spin-polarized, non-interacting system \mathcal{S} : $U_i = 0$ for all i , which can be both solved exactly for the current [85, 86] and the result compared to the exact LDOS (see Sec. 3.5). Figure 3.2c shows the reconstruction of the LDOS using a finite lattice and time average. There is quantitative agreement between the exact LDOS and that from the energy-resolved probe. The dominant source of error in the LDOS is the finite probe bandwidth $\omega_{\mathcal{P}}$, not the length of the lattice or the time of the average (Fig. 3.2d and e). This demonstrates that cold-atom systems or many-body simulations are well suited to implement this method, which are limited to finite lengths and times. As $\omega_{\mathcal{P}} \rightarrow 0$, the total lattice length, $N \rightarrow \infty$, and the averaging time, $|\mathcal{T}| \rightarrow \infty$, the exact LDOS would be recovered.

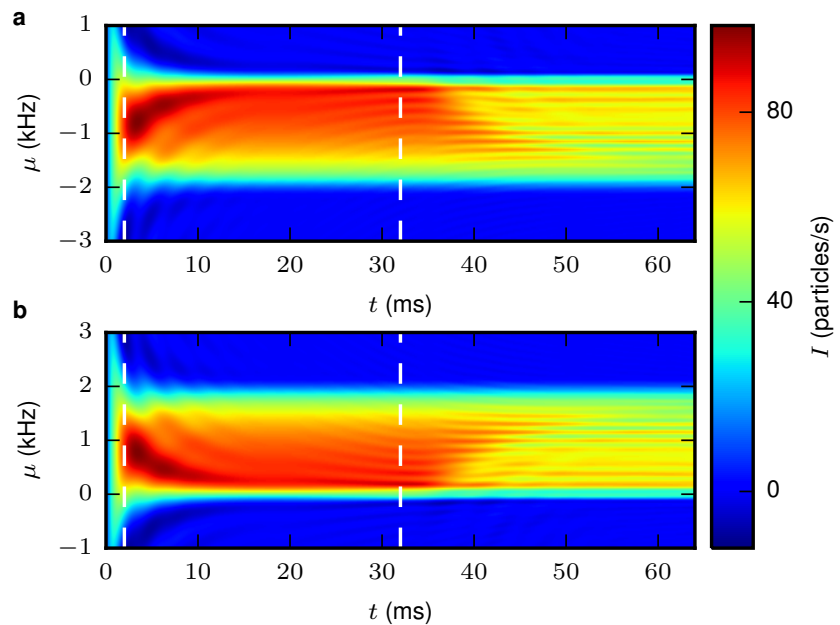


Figure 3.2: Non-interacting, fermionic LDOS. The electronic current versus time for the (a) occupied S states—using an initially empty P —and (b) unoccupied S states in a 1D lattice versus μ , the shift in onsite frequency of P . Here, the total lattice length, N , is 64, the bandwidth of the probe is 400 Hz, and the dotted lines indicate the region averaged for the current, $t \in \mathcal{T} = [2 \text{ ms}, 32 \text{ ms}]$ (to minimize the influence of transient currents and edge effects).

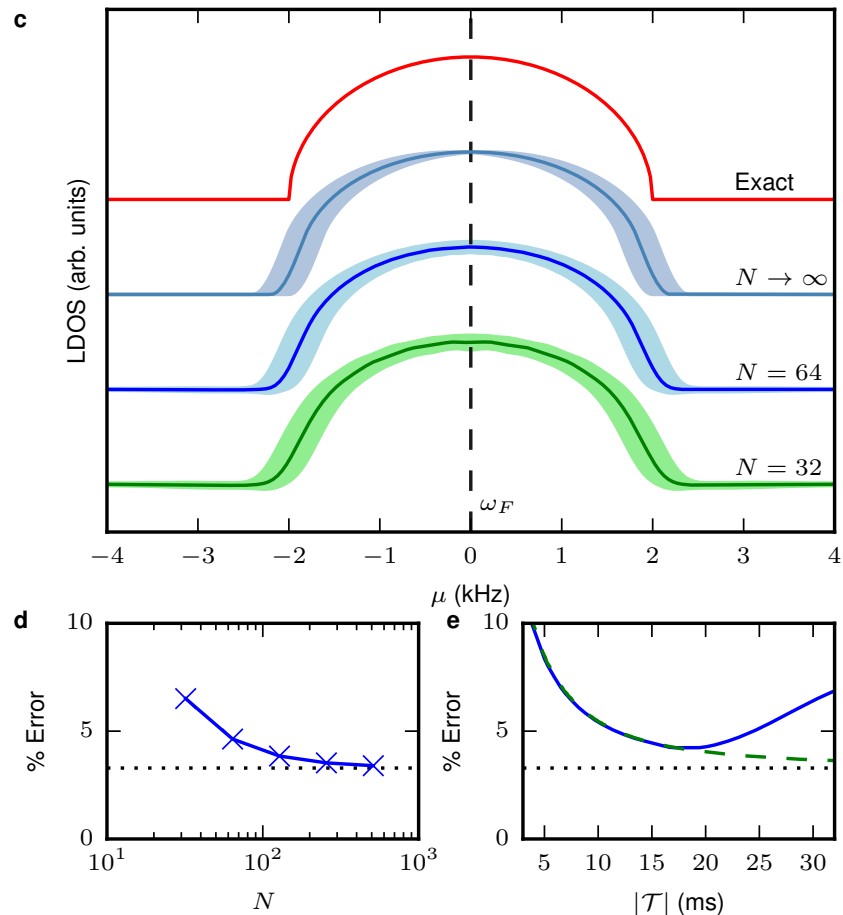


Figure 3.2: (Continued) (c) The average currents are proportional to the LDOS for \mathcal{S} , displayed here with an offset for clarity. The shaded regions represent the error calculated using the standard deviation of the current in the region \mathcal{T} combined with a broadening error of size $2\omega_P$. The Fermi level, ω_F , is found from where the two measurements connect. (d) Integrated error of the normalized LDOS versus total lattice size and (e) versus averaging time, $|\mathcal{T}|$, (blue solid line is $N = 32$, green dashed line is $N = 512$). The baseline error (when $N \rightarrow \infty$, the dotted line in (d) and (e)) is set by the finite $\omega_P = \omega_S/10$, which broadens the true LDOS. For short lattices and times, the error in the LDOS is already small. Thus, even modest cold-atom systems or numerical many-body calculations can effectively reconstruct the LDOS.

3.4 Interacting System Simulation

We now apply the same approach to an interacting system with a constant $U_i = U$. Figure 3.3 shows the LDOS of a Mott-insulator like state. As the interaction strength increases, the band splits and a gap forms between the occupied and unoccupied bands, as is typical for a Mott insulator. However, the Fermi frequency, $\omega_F \approx U/2$, and the occupied band is shifted to higher frequency. The observations also agree with predictions from Green's function in the hopping-only and interaction-only limits (see Sec. 3.5). In Ref. [50], it was found that there is a filling-dependent, conducting-to-nonconducting transition as a function of U for interacting-induced transport: An inhomogeneous quench in U , where the interaction strength is taken from 0 to a finite value for half the lattice, drives particles from that half of the lattice to the other (non-interacting) half so long as U is not too strong and the filling not too large. Figure 3.3b demonstrates that it is this shift of the occupied bands to higher frequency that aligns occupied states in the interacting side to open states in the non-interacting side, allowing particles to flow. As U is increased further, eventually only the tail of the occupied band is aligned with open states, thus giving a decreasing current.

When spatial dependence of the density of states is of interest, the probe can be used in a way analogous to a “scanning-mode”: The probe can be coupled to the system at any point along its length through a right angle construction, as shown in Fig. 3.4a. Examining a system with spatially inhomogeneous interactions—e.g., a linear decrease in the induced U , Fig. 3.4b—can determine both how the particle density shifts in space and energy. Figure 3.4c shows the occupied and unoccupied LDOS of this inhomogeneous lattice as a function of position. The spatial decrease of the interactions forces particles to the region with small interactions, where at the very end the lattice has an LDOS similar to a non-interacting system. Just near the non-interacting boundary, however, a large peak in occupied density of states forms, i.e., states pinned well below the Fermi level. On the interacting side, the number of particles is small with an LDOS just

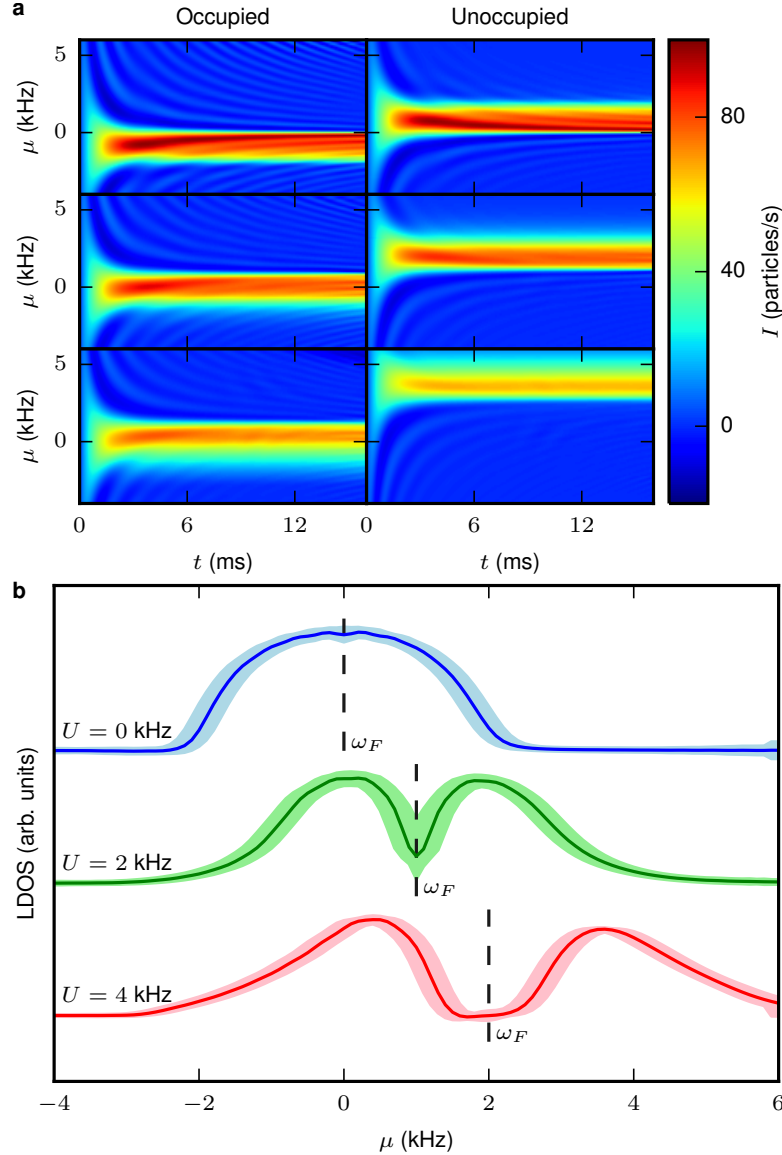


Figure 3.3: Many-body, fermionic LDOS. The time-dependent current was found using numerical many-body calculations for the (a) occupied and unoccupied states of a 1D lattice with a constant onsite interaction term $U_i = 0 \text{ kHz}$, 2 kHz , 4 kHz (from top to bottom), and total size $N = 32$. (b) The resulting LDOS for $U \in \{0 \text{ kHz}, 2 \text{ kHz}, 4 \text{ kHz}\}$, displayed with an offset for clarity, using the same averaging procedure as performed as in Fig. 3.2, with the shaded regions indicating the standard deviation of the current combined with the probe broadening error. Note that a steady-state still forms as the system ceases to be a true insulator once it is connected to the non-interacting probe. As U increases, a gap forms between the occupied and unoccupied bands, in addition to causing a pronounced broadening of both of the bands

below the Fermi level. An even-odd effect is visible, which is due to finite lattice effects, creating oscillations away from the boundaries.

3.5 Methods

The non-interacting lattice is exactly solvable for both the current and the LDOS. For the current, we need the retarded Green's function for a semi-infinite lattice with onsite frequency μ and hopping frequency $\omega_{\mathcal{P}}$, which is [86, 87]

$$g_{\mathcal{P}}^r(\omega) = (1/2\omega_{\mathcal{P}}^2) \left[(\omega - \mu) - i\sqrt{4\omega_{\mathcal{P}}^2 - (\omega - \mu)^2} \right]. \quad (3.6)$$

Using this expression, the current for the infinite lattice, $N \rightarrow \infty$, is given by the Landauer formula,

$$I = \frac{e}{2\pi} \int_{-\infty}^{\infty} d\omega [f_{\mathcal{S}}(\omega) - f_{\mathcal{P}}(\omega)] T(\omega), \quad (3.7)$$

where $f_{\mathcal{S}(\mathcal{P})}$ are the initial particle distributions (Fermi-Dirac distributions or completely filled/empty) in $\mathcal{S}(\mathcal{P})$ and $T(\omega)$ is the transmission coefficient.

$$T(\omega) = \frac{4 \operatorname{Re} \left[\sqrt{4\omega_{\mathcal{P}}^2 - (\omega - \mu)^2} \right] \operatorname{Re} \left[\sqrt{4\omega_{\mathcal{S}}^2 - \omega^2} \right]}{\left| \mu + i\sqrt{4\omega_{\mathcal{P}}^2 - (\omega - \mu)^2} + i\sqrt{4\omega_{\mathcal{S}}^2 - \omega^2} \right|^2}. \quad (3.8)$$

Implementing the setup with $f_{\mathcal{P}}(\omega) \in \{0, 1\}$ gives the reconstructed LDOS as simply a sum of the occupied and unoccupied states, and also directly yields the Fermi level, ω_F . In the main text, the system of interest \mathcal{S} is half filled and in its zero temperature ground state. Here we show, for simplicity, how the LDOS of a fully filled non-interacting system can be mapped out. The current in this case is $I = \frac{e}{2\pi} \int_{\mu-2\omega_{qp}}^{\mu+2\omega_{qp}} T(\omega) d\omega$. When $\omega_{\mathcal{P}} \ll \omega_{\mathcal{S}}$, only $\sqrt{4\omega_{\mathcal{P}}^2 - (\omega - \mu)^2}$ is changing significantly while $\sqrt{4\omega_{\mathcal{S}}^2 - \omega^2}$ is relatively smooth. Thus, we can integrate out the rapidly changing part and substitute the averaged value for the smooth part, which leads to

$$I \approx e \left(\frac{\omega_{\mathcal{P}}}{\omega_{\mathcal{S}}} \right)^2 \sqrt{4\omega_{\mathcal{S}}^2 - \mu^2}. \quad (3.9)$$

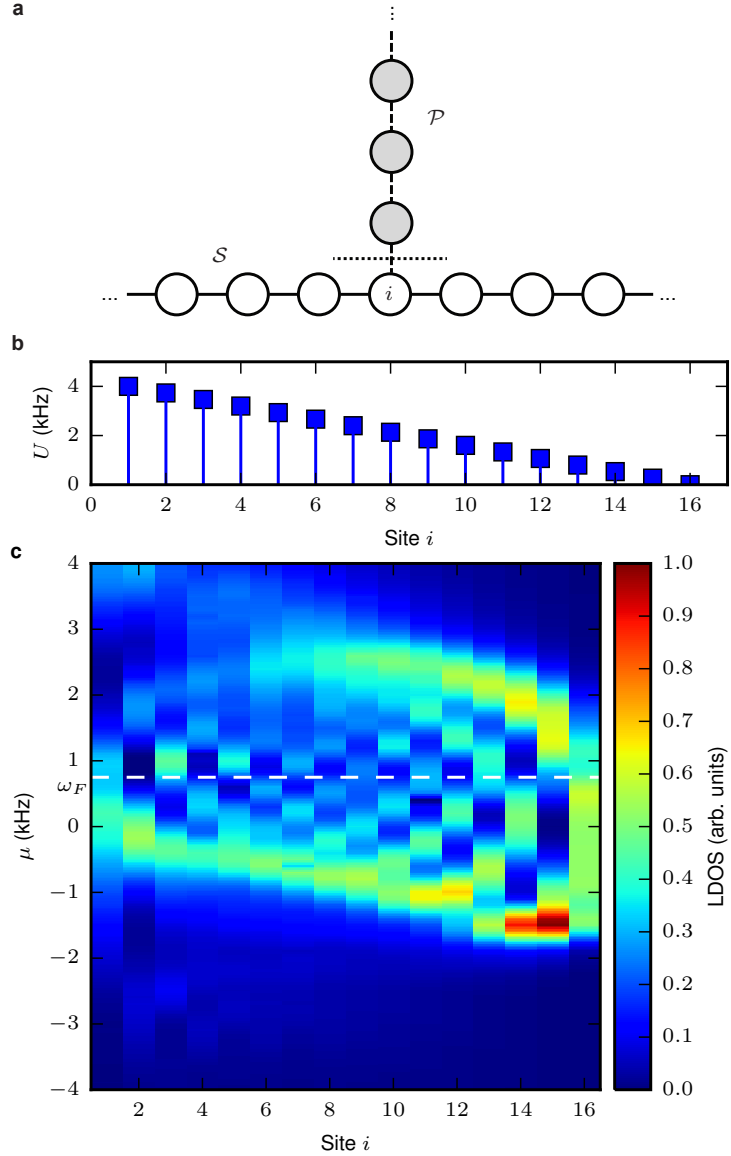


Figure 3.4: The “scanning-mode” of the energy-resolved probe. (a) Perpendicular geometry with \mathcal{S} as the interacting system and \mathcal{P} as the probe. The LDOS calculation was repeated for each site $i \in \mathcal{S}$. (b) \mathcal{S} has an inhomogeneous interaction profile: a linear decrease from $U = 4$ kHz on one end to $U = 0$ kHz on the other. (c) The LDOS for occupied and unoccupied states as a function of frequency offset μ and contact lattice position i . The weakly-interacting region of the system allows more particles to occupy lower frequency states, while the more strongly-interacting side forces the open states well beyond the Fermi level. In addition, an even-odd effect is visible, which is due to the finite size of the lattice, creating oscillations from the boundary.

When compared to Eq. (3.3), the exact LDOS, $D_{\text{ex}}(\mu) = \sqrt{4\omega_S^2 - \mu^2}/(4\omega_S^2)$, for a non-interacting \mathcal{S} can be extracted. The remaining terms in the full expression broaden the reconstructed LDOS by approximately the probe bandwidth, $4\omega_P$, which thus has to be small enough to discriminate features in the LDOS of \mathcal{S} and, when using a cold-atom setup, the bandwidth should be large enough to get an appreciable current.

For systems in the thermodynamic limit, the LDOS is related to the real-space Green's function by [88]

$$D(\mathbf{r}, \omega) = -\frac{1}{2\pi} \text{Im} [g^r(\mathbf{r}, \mathbf{r}, \omega)]. \quad (3.10)$$

The Green's function of the Hubbard model, interestingly, are known in the two limits where $U = 0$ and $\omega_S = 0$. This allows us to better understand our results. When $U = 0$, the Green's function of the last site of an semi-infinite chain is given in Eq. (3.6). Thus, $D(\omega) = \sqrt{4\omega_S^2 - \omega^2}/(4\omega_S^2)$, which agrees with the Landauer formula shown above. When $\omega_S = 0$, the Green's function on a selected site is [89]

$$g_S^r(\omega) = \frac{1}{2\pi} \left(\frac{1 - (n/2)}{\omega - \omega_0} + \frac{n/2}{\omega - \omega_0 - U} \right). \quad (3.11)$$

Here n is the occupation number and ω_0 is the onsite frequency term, which plays the role of chemical potential. At half filling, one may choose $\omega_0 = 0$. By analytic continuation $\omega \rightarrow \omega - i0^+$, we obtain $D(\mu) = (1/4\pi^2)\{[1 - (n/2)]\delta(\mu - \omega_0) + (n/2)\delta(\mu - \omega_0 - U)\}$. Thus, there are two peaks at ω_0 and $\omega_0 + U$. Away from the isolated limit, the two peaks broaden into two bands centered around ω_0 and $\omega_0 + U$, and this agrees with our observation shown in Fig. 3.3.

In order to extract the LDOS from real-time measurements on finite lattices, the current must be averaged over a finite time, i.e., the current will be in a quasi-steady state. The estimate of the LDOS is thus

$$D(\mu) \propto \frac{1}{|\mathcal{T}|} \int_{\mathcal{T}} I(t) dt. \quad (3.12)$$

As $|\mathcal{T}|, N \rightarrow \infty$, this will converge to the true steady state. As we demonstrate, already for very small lattices an accurate LDOS can be obtained and thus only modest resources are needed.

The numerical calculations are performed as follows: For the non-interacting system, the current was found from the numerical integration of the equations of motion [85, 86]. The transient current when the probe is placed in contact with the system is damped on the characteristic tunneling time and the recurrence time is proportional to the lattice size, which determine both the lower and upper limits to the time region \mathcal{T} given a finite lattice length. We use $\mathcal{T} = [2 \text{ ms}, N/2 \text{ ms}]$, where N is the lattice length. We can also define an exact error for the non-interacting case,

$$\% \text{ Error} = 100\% \cdot \frac{\sqrt{\int [D(\mu) - D_{\text{ex}}(\mu)]^2 d\mu}}{\sqrt{\int D_{\text{ex}}(\mu)^2 d\mu}}, \quad (3.13)$$

where $D_{\text{ex}}(\mu)$ is the exact LDOS.

The uncertainty due to probe broadening is found from the assumption that an state can be contribute to the current anywhere within the probe bandwidth of $4\omega_q p$, which results in error, $\sigma_+(\mu)$, of

$$D(\mu) - \max [D(\mu), D(\mu - 2\omega_p), D(\mu + 2\omega_p)] \quad (3.14)$$

for the positive μ side and, $\sigma_-(\mu)$,

$$D(\mu) - \min [D(\mu), D(\mu - 2\omega_p), D(\mu + 2\omega_p)] \quad (3.15)$$

for the negative side. This is combined with the standard deviation error from \mathcal{T} for a final error of

$$\sigma_{\text{tot}}^\pm = \sqrt{\sigma_\pm^2 + \sigma_{\text{stdev}}^2}. \quad (3.16)$$

For the interacting systems, we perform time-dependent, density matrix renormalization group calculations [15, 90] within the ITensor tensor product library [91]. In all simulations, the time step was reduced until the calculation converged with respect to energy conservation and the maximum matrix bond dimension was allowed to increase without bound. The energy cutoff was set to $10^{-9}\omega_S$. The averaging is done in the region $\mathcal{T} = [2 \text{ ms}, N/2 \text{ ms}]$, as with the non-interacting case.

3.6 Conclusion

The density of states is a concept of immense importance to all areas of physics. We provide an operational definition of the LDOS for many-body systems, applicable to in- and out-of-equilibrium cases, fermionic or bosonic system, etc. The core principle is that for a steady-state current to flow into an empty, narrow probe band, there must be occupied states at that energy (similarly for a full narrow band and unoccupied states). We demonstrate that a cold-atom setup will allow for the measurement of this operational definition: The many-body LDOS can be extracted with minimal disturbance to the system. A related setup, where tunable cold-atom systems are used to more controllably—i.e., with less disturbance to the native state—implement Eqs. (3.1) and (3.2), is also beneficial, but the narrow band setup we propose minimizes the total current flowing and all other disturbances, more so than that of a mimicking of the STM. The ability to probe the undisturbed density and occupation of states versus energy and position illuminates the structure of many-body systems and allows one to make progress in the theoretical description of underlying physical processes.

Chapter 4: Interaction-Driven Electronic Transport

The previous Chapter discussed the formation of a steady state from an interacting system, initially in its own ground state, that was coupled to another system at $t = 0$. Alternatively, it is possible to generate a steady-state condition though manipulating the interaction strength. Here, we examine a system, which starts in the non-interacting ground state, which is perturbed by the switching on of an inhomogenous interaction. This Chapter contains work performed in collaboration with Chih-Chun Chien and Massimiliano Di Ventra and the full version is found in Ref. [50].

4.1 Introduction

Advances in experimental studies of quantum transport of ultra-cold atoms in optical lattices [27, 69, 70, 73, 92] draw attention to different aspects of systems out of equilibrium. In conventional condensed matter settings, an electrical current is induced by applying a voltage difference across the sample. The interaction of the charge carriers are usually homogeneous, except near impurities. In contrast, ultra-cold atoms are charge neutral and so far the motion of an atomic cloud has been generated by placing the cloud away from its equilibrium position [73] or by a sudden shift of the minimum

of its trapping potential or its distortion [27, 69, 70, 92]. The interactions are generated by either adding another species of atoms [73] or tuning magnetic-field controlled collisions [70, 92].

In this Chapter we instead suggest a method to drive a mass current of atoms via *local tuning of interactions*. This, in turn, reveals interesting phenomena otherwise difficult to observe in conventional solid state systems. A key to realize interaction-induced transport is controllable inhomogeneous interactions – a novel possibility offered by optically tunable collisions of ultra-cold atoms. The optical Feshbach resonance (OFR) [93–96] is a promising technique for controlling interactions *locally* using focused laser beams. For instance, the spatial modulation of density using the OFR of bosons [94] demonstrates the power of controllable inhomogeneous interactions. Other exotic equilibrium structures may also be generated by using this tool [97].

We also point out that these optically controlled interactions can be *time dependent*. Suddenly turning on the interactions, for instance, will drive the system out of equilibrium. Thus, instead of using external driving mechanisms such as a voltage bias, it is possible, with suitable initial conditions and patterns of interactions, to induce a mass current. We show that for reasonably weak interactions the mass current of fermions is similar to a charge current in electronic systems. Further, increasing the interaction strength leads to the atomic equivalent of negative differential conductance, where the current reaches a maximum value and then subsequently decreases. A mean-field approximation predicts that this decrease leads to a conducting-to-nonconducting transition after the interaction strength exceeds some threshold (dependent on the filling). This transition may be explained by a mismatch of energy spectra between the interacting and non-interacting parts of the system, but this argument does not rule out other possible current-carrying states.

Time-dependent density-matrix renormalization group (td-DMRG) simulations [98], as well as a higher-order approximation, demonstrate that indeed a conducting to non-conducting transition should exist in the strongly interaction-imbalanced regime when

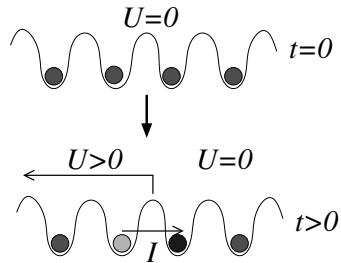


Figure 4.1: Schematic plot of the experimental set up we simulate. Non-interacting ultra-cold fermions are loaded into the lowest energy state of a 1D homogeneous optical lattice. At $t = 0$, a focused laser beam then induces on-site repulsive interactions of the Hubbard type on the left half of the lattice. Due to the imbalance of interactions, a mass current is induced. We emphasize that there is no need to “mechanically” set the atoms out of equilibrium by tilting a potential nor is it necessary to introduce additional species of atoms or dissipation. Moreover, this setup may also be implemented to study quench dynamics [104]. The gray dots emphasize that atoms may be in a superposition of different quantum states.

the initial state is not far away from a band insulator. The threshold value for the transition, however, differs from different approaches. Importantly, the many-body negative differential conductance remains at all levels of approximation. This is the counterpart to negative differential conductivity observed in solid-state structures [99, 100], where changes in the carrier density or subdivisions of the Brillouin zones cause non-monotonic dependence of the current on the external field strength. We note that, recently, negative mobility of cold atoms in temporally modulated optical lattices [101] and negative differential conductance in fermion-boson mixture in optical lattices [102] have been discussed. We propose, alternatively, that one may observe negative differential conductance in a setup where the optical lattice potential is static and by tuning the interactions in real space. We focus on fermions but notice that, for the Bose-Hubbard model, Ref. [103] considers the sudden connection of a superfluid and a Mott insulator with different chemical potentials and found a mass current as well.

4.2 Interaction-induced Transport

In our approach – which explicitly follows the dynamics of mass transport – we implement the micro-canonical formalism (MCF) [55, 105] as in Refs. [85, 106] which monitors the evolution of the correlation matrix. When applied to a system of noninteracting atoms on a 1D optical lattice suddenly losing the atoms on the right half of the lattice, MCF shows very different dynamics for bosons and fermions [85]. While the bosonic current decays to zero in the thermodynamic limit, the fermionic current exhibits a quasi steady-state current corresponding to a plateau in the current as a function of time. Importantly, the MCF is designed for finite closed quantum systems so it is particularly suitable for studying the dynamics of ultra-cold atoms. Although our proposed setup can be applied to bosons, to explore their dynamics theoretically one has to consider also the effect of the quasi-condensate which renders the analysis more involved. Therefore, here we focus only on fermions.

We consider $N_{p\sigma}$ ($\sigma = \uparrow, \downarrow$) two-component fermions, with $N_{p\uparrow} = N_{p\downarrow}$, loaded into a 1D optical lattice of size N , see Fig. 4.1. This type of finite-length 1D lattice may be generated by inserting a thin optical barrier [107] into a ring of optical lattice [108]. The resulting C-shaped lattice is geometrically identical to the setup here. This confining potential creates a uniform lattice and does not require a background harmonic trapping potential parallel to the lattice. The background interactions are assumed to be negligible. The system is initially described by the tight-binding tunneling Hamiltonian $H_0 = -\bar{t} \sum_{\langle ij \rangle, \sigma} c_{i\sigma}^\dagger c_{j\sigma}$, where $\langle ij \rangle$, \bar{t} , $c_{i\sigma}^\dagger$ ($c_{i\sigma}$) denote nearest-neighbor pairs, the hopping coefficient, and the creation (annihilation) operator of site i , respectively. The unit of time is $t_0 \equiv \hbar/\bar{t}$ and is about few ms for reasonable lattice depths [85].

The initial state corresponds to the lowest energy state of H_0 , with no correlations between up and down spin states (see, e.g., Refs. [85, 106]). The system is then set out of equilibrium by introducing interactions among atoms on the left half of the lattice by, e.g., optically-induced collisions using a focused laser beam. Here we concentrate on moderate repulsive interactions and non-integer filling. This allows us to focus on the

dynamics induced by the interactions and avoid unnecessary confusions about possible equilibrium phase transitions such as the Bardeen-Cooper-Schrieffer instability or the Mott-insulating phase in uniform and static interacting systems [23]. We model an instantaneous switch-on of the interactions with a sharp interface between the interacting and non-interacting regions and relax the former condition later on.

The Hamiltonian generating the dynamics is

$$H_e = H_0 + \sum_{i \in L} U \hat{n}_{i\sigma} \hat{n}_{i\bar{\sigma}}. \quad (4.1)$$

Here $\hat{n}_{i\sigma} = c_{i\sigma}^\dagger c_{i\sigma}$, U is the onsite repulsive coupling constant, L denotes the left half of the lattice, and $\bar{\sigma}$ is the opposite of σ . This model should be appropriate for moderate lattice depth [109]. Since \bar{t} can be tuned by the lattice depth and U can be tuned by OFR, U/\bar{t} can span a broad range so our study should be relevant to experiments.

The equations of motion for the correlation matrix are $i(\partial \langle c_{i\sigma}^\dagger c_{j\sigma} \rangle / \partial t) = \langle [c_{i\sigma}^\dagger, H_e] c_{j\sigma} \rangle + \langle c_{i\sigma}^\dagger [c_{j\sigma}, H_e] \rangle$, where $[\cdot, \cdot]$ denotes the commutator of the corresponding operators. The explicit expression can be found using standard anti-commutation relations. After some algebra, one gets

$$i \frac{\partial \langle c_{i\sigma}^\dagger c_{j\sigma} \rangle}{\partial t} = \bar{t} X_\sigma - U (\langle c_{i\bar{\sigma}}^\dagger c_{i\bar{\sigma}} c_{i\sigma}^\dagger c_{j\sigma} \rangle)_{i \in L} + U (\langle c_{i\sigma}^\dagger c_{j\sigma} c_{j\bar{\sigma}}^\dagger c_{j\bar{\sigma}} \rangle)_{j \in L}. \quad (4.2)$$

Here $X_\sigma \equiv \langle c_{i+1,\sigma}^\dagger c_{j\sigma} \rangle + \langle c_{i-1,\sigma}^\dagger c_{j\sigma} \rangle - \langle c_{i\sigma}^\dagger c_{j+1,\sigma} \rangle - \langle c_{i\sigma}^\dagger c_{j-1,\sigma} \rangle$ and $n_{i\sigma} = \langle \hat{n}_{i\sigma} \rangle$. We solve Eq. (4.2) both at the mean-field level and by adding higher-order correlations.

The mean-field level solution can be obtained by Wick decomposition of $\langle c_{i\bar{\sigma}}^\dagger c_{i\bar{\sigma}} c_{i\sigma}^\dagger c_{j\sigma} \rangle$ as $\langle c_{i\bar{\sigma}}^\dagger c_{i\bar{\sigma}} \rangle \langle c_{i\sigma}^\dagger c_{j\sigma} \rangle$ since no spin-flip mechanisms are present. This is the standard Hartree-Fock approximation. The equations are closed after this approximation. Thus the dynamics after the interaction is switched on can be monitored by integrating Eq. (4.2) with the initial condition $c_{ij\sigma}(t=0)$ given by the lowest energy state of the non-interacting Hamiltonian. We update Eq. (4.2) in a symmetric fashion so that $\langle c_{i\sigma}^\dagger c_{j\sigma} \rangle = \langle c_{i\bar{\sigma}}^\dagger c_{j\bar{\sigma}} \rangle$

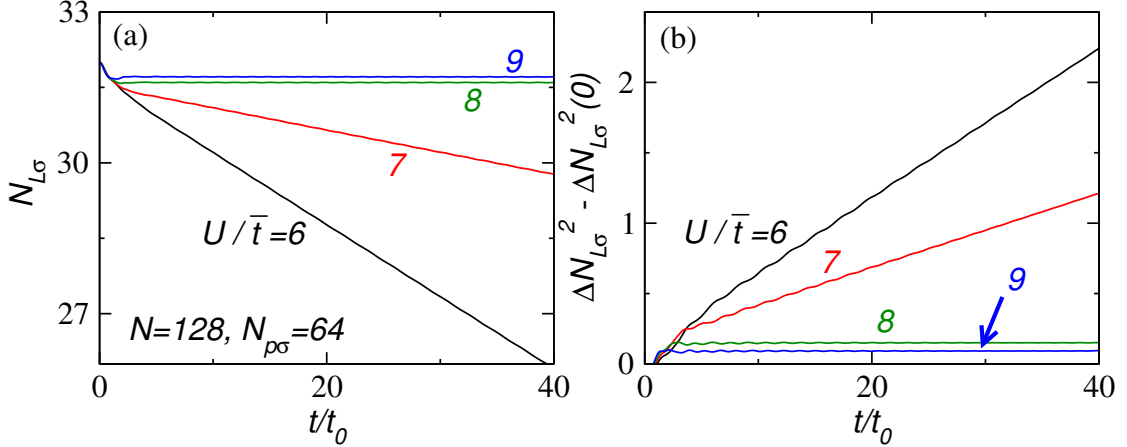


Figure 4.2: Mean-field particle number and number fluctuation dynamics. (a) $N_{L\sigma}$ and (b) $\Delta N_{L\sigma}^2 - \Delta N_{L\sigma}^2(t=0)$ with $N = 128$ and $N_{p\sigma} = 64$ for each species from mean-field dynamics.

at any time. Later on we will also go beyond mean-field by developing a higher-order approximation and by performing td-DMRG simulations.

In addition to the current $I_\sigma = 2\bar{t}\text{Im}\langle c_{N/2,\sigma}^\dagger c_{N/2+1,\sigma} \rangle$, we also evaluate the particle number on the left half lattice, $N_{L\sigma} = \langle \hat{N}_{L\sigma} \rangle$ and its fluctuations $\Delta N_{L\sigma}^2 = \langle \hat{N}_{L\sigma}^2 \rangle - \langle \hat{N}_{L\sigma} \rangle^2$, which is another property that can be determined experimentally. Here $\hat{N}_{L\sigma} = \sum_{i \in L} \hat{n}_{i\sigma}$. Explicitly,

$$\Delta N_{L\sigma}^2 = \sum_{i=1}^{N/2} n_{i\sigma} (1 - n_{i\sigma}) - 2 \sum_{i < j}^{N/2} |c_{ij\sigma}|^2. \quad (4.3)$$

Right before the interactions are switched on, there can be initial number fluctuations due to the wave nature of the initial quantum state. We thus present $\Delta N_{L(\sigma)}^2 - \Delta N_{L(\sigma)}^2(t=0)$ which reflects the change of the number fluctuations due to the interaction-induced dynamics.

4.3 Results and Discussions

Figure 4.2 shows the particle number and its fluctuations of the left half lattice with $N = 128$ and $N_{p\sigma} = 64$ for each species. Since the system size is finite, there is reflection of the current off the boundary after a revival time but we focus on dynamics before this revival occurs. As U/\bar{t} increases, one can see that instead of inducing more fermions to move from the left to the right, above a certain threshold value the transport is no longer observed within a reasonable time scale (e.g., $t \leq (N/2)t_0$). This corresponds to a conducting-nonconducting transition and it can be found at other ratios of $f \equiv N_{p\sigma}/N$. In general the threshold U_c/\bar{t} decreases as f increases. We will show that this is because for higher filling the onsite interaction energy dominates more easily. One can see this transition even better in the average current itself.

We note that it has been shown that with suitable initial conditions non-interacting fermions can develop a quasi steady-state current (QSSC) [85, 110]. This is so also for the present interacting case. The fermionic current is shown in Figure 4.3(a) for $N = 128$ and $N_{p\sigma} = 64$ for each species. The current may be measured by the protocol of Refs. [85, 111]. The plateaus shown in $I_\sigma(t)$ indicate the existence of QSSCs. To smooth over small oscillations, we define an averaged current as $\langle I_\sigma \rangle \equiv (1/30t_0) \int_{10t_0}^{40t_0} dt I_\sigma(t)$ and plot $\langle I_\sigma \rangle$ as a function of U/\bar{t} for $N_{p\sigma} = 32, 64, 96$ in Fig. 4.3(b). For small U/\bar{t} we clearly see that the averaged current increases linearly with U/\bar{t} . Then the dependence deviates from a linear form before the conducting-nonconducting transition. For even larger U/\bar{t} , $\langle I_\sigma \rangle$ decreases until no finite averaged current can be found. The non-monotonic dependence of $\langle I_\sigma \rangle$ on U resembles the negative differential conductivity observed in conventional solid-state devices [99, 100]. In the strongly interaction-imbalanced regime, we found oscillations in the density profile and further studies may connect those oscillations to the charge domains in solid-state devices exhibiting negative differential conductivity.

The interaction term thus acts as a bias on the left half lattice if U/\bar{t} is small. Here we investigate the validity of this statement. By extracting the slope of the linear part of $\langle I_\sigma \rangle$ for small U/\bar{t} , one can study how efficient the interaction can induce a current. The

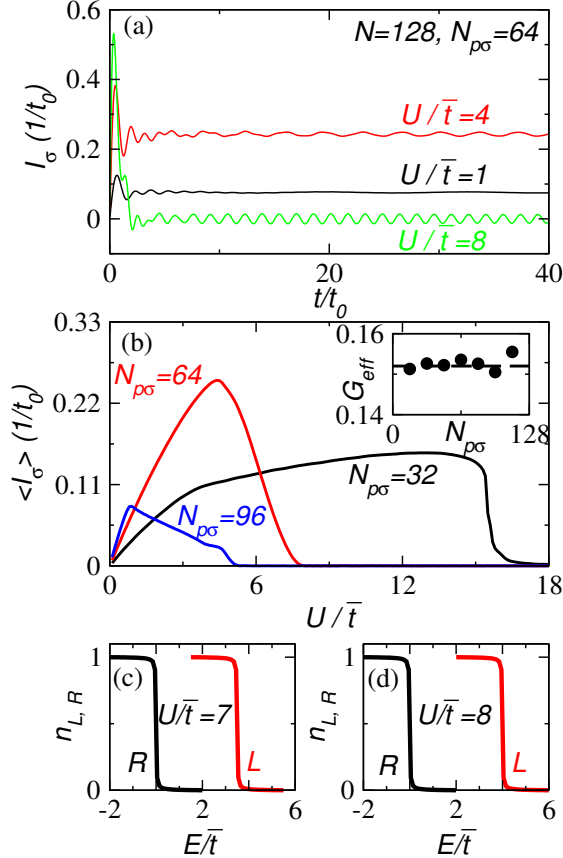


Figure 4.3: Average current dynamics and energy spectra. (a) I_σ and (b) $\langle I_\sigma \rangle$ of the fermionic case with $N = 128$ and $N_{p\sigma} = 64$ for each species from mean-field dynamics. The inset of (b) shows $G_{eff} \equiv f^{-1} d\langle I_\sigma \rangle / dU$ (in units of $2\pi/h$) for small U/\bar{t} as a function of $N_{p\sigma}$ for $N = 128$, where $f = N_{p\sigma}/N$ is the initial filling factor. The dashed line shows $G_0 \approx 0.152$ in this unit. The energy spectra of the left (L) and right (R) half lattices when U is switched on are shown for $U/\bar{t} = 7$ (c) and $U/\bar{t} = 8$ (d). Here $N = 128$ and $N_{p\sigma} = 64$.

inset of Fig. 4.3(b) shows the effective conductance $G_{eff} \equiv f^{-1} d\langle I_\sigma \rangle / dU$ as a function of $N_{p\sigma}$ for a fixed N , where $f = N_{p\sigma}/N$ is the initial filling factor. As $N_{p\sigma} \rightarrow N$ the system approaches a band insulator¹ and there is only a tiny range of U/\bar{t} where a finite $\langle I_\sigma \rangle$ exists. This could contribute to some inaccuracy of the extraction of the slope close to $N_{p\sigma} \rightarrow N$. Nevertheless, as shown on the inset of Fig. 4.3(b) the effective conductance is close to the ideal quantized conductance $G_0 = (2\pi\hbar)^{-1}$ for arbitrary initial filling.

¹For a single-band model of fermions considered here, $N_{p\sigma}/N = 1$ corresponds to a band insulator and no current can flow even in the presence of inhomogeneous interactions.

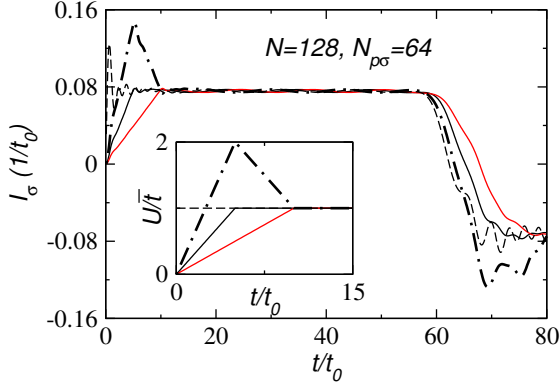


Figure 4.4: Currents induced by different ways of switching-on the interaction. A sudden switch-on of the interaction (dashed line), linear switch-ons with switching times $t_m = 5t_0$ (black) and $t_m = 10t_0$ (red), and a multi-step switch-on (dot-dash line). The inset shows the time dependence of U for the four cases. Here $N = 128$ and $N_{p\sigma} = 64$.

This establishes the feasibility of using a weak inhomogeneous interaction as an efficient driving force for inducing a current and its correspondence with a bias, $\Delta\mu = fU$.

In the weak interaction regime, we found another interesting phenomenon. By considering different ways of switching on the interaction, one may wonder whether the system will reach the same magnitude of the QSSC. We simulate different switching-on scenarios by introducing a time scale t_m such that the interaction grows from zero to its full value during t_m and remains a constant after that. Figure 4.4 shows that despite different time-dependences of the interaction, the system always reaches the same magnitude of the QSSC. We have also checked other more complicated functional forms for switching on the interaction and found the same QSSC. Importantly, even if the system is over-excited by a spike in the time dependence of U , when U comes back to a constant value the height of the QSSC coincides with the case of a sudden switch-on of the interaction as shown on Fig. 4.4. Thus the magnitude of the QSSC is robust (memory-less) against different ways the interaction is switched on. This feature makes the interaction-induced transport appealing for making devices since a steady output (the QSSC) is insensitive to the transient behavior of the driving force (the interaction).

When the optically-induced interactions are switched on, it is possible that the onsite

potential could be shifted due to the increase of the kinetic energy of the atoms interacting with the incoming photons. We study possible effects by adding an extra term $V \sum_{i \in L, \sigma} \hat{n}_{i\sigma}$ to H_e of Eq. (4.1) to simulate this effect with a positive V . This shift of the onsite potential acts like a bias so one might expect that more current will flow to the other side. However, the negative differential conductance and the mean-field conducting-nonconducting transition are robust against this positive potential shift. The energetic mechanism described below will make it clear why a positive potential shift will not affect the results qualitatively, thus showing that it is not sensitive to this type of modification of the Hamiltonian.

We now discuss the reason behind the negative differential conductance and the conducting to non-conducting transition, which is energetic in nature. In order to obtain a “macroscopic” steady-state current, αN particles must be transferred from the left to the right halves, where α is some small proportionality constant. However, this entails a change in energy, as the particle density decreases on the site with interactions, and this effect must be compensated by an energy change due to rearrangement of the single particle states. To be more concrete, immediately after interactions are turned on, the system is still in the ground state of H_0 . However, the energy has shifted to

$$E = E_0 + U \sum_{i \in L} \langle n_{i\sigma} n_{i\bar{\sigma}} \rangle_0 = E_0 + U \sum_{i \in L} \langle n_{i\sigma} \rangle_0 \langle n_{i\bar{\sigma}} \rangle_0, \quad (4.4)$$

where Wick’s theorem has been applied since the system is in the ground state of H_0 . The subscript of $\langle \dots \rangle$ denotes the time when the expectation is taken. For half-filling, this gives an energy $E = E_0 + UN/8$. For arbitrary filling f , it is

$$E \approx E_0 + f^2 UN/2, \quad (4.5)$$

where the expression is approximate since not all site occupation numbers will be exactly f (for each spin component).

The energy at some later time will still be E (since no further changes have been made to the Hamiltonian), but will have the form

$$E = \langle H_0 \rangle_t + U \sum_{i \in L} \langle n_{i\sigma} \rangle_t \langle n_{i\bar{\sigma}} \rangle_t \quad (4.6)$$

in the mean-field approximation. Assuming the αN atoms are taken uniformly from the left half, the energy is

$$E \approx \langle H_0 \rangle_t + f^2 UN/2 - \alpha f UN. \quad (4.7)$$

Taking the difference of Eq. (4.7) and Eq. (4.5), and using energy conservation, gives $\langle H_0 \rangle_t - E_0 \approx \alpha f UN$. However, the quantity $\langle H_0 \rangle_t - E_0$ can not be arbitrary, since we have a finite bandwidth. Regardless of whether one has an interacting or noninteracting state, the largest energy change due to the H_0 contribution is $4\bar{t}\alpha N$, corresponding to taking the αN particles from the lowest part of the band (on the left half) to the highest part (on the right half). This gives

$$\alpha f UN \lesssim 4\bar{t}\alpha N \longrightarrow U \lesssim 4\bar{t}/f \quad (4.8)$$

and thus results in a threshold value of U . Beyond this value of U , a macroscopic current can not flow within the mean-field approximation and when the particles are taken uniformly from the interacting lattice. We remark that here we consider the lowest energy band of the optical lattice. If the interaction energy exceeds the band gap separating different bands, the system may re-enter a conducting state. We also remark that energy mismatches can result in other interesting phenomena as discussed in Refs. [112, 113].

To demonstrate this energetic mechanism, Fig. 4.3(c) and (d) show the energy spectra of the left (L) and right (R) half lattices when U is switched on for $N = 128$ with $N_{p\sigma} = 64$. When $U/\bar{t} = 7$ (panel (c)), there is still an overlap between the two spectra and exchanging atoms in an energy-conserving fashion is possible. For $U/\bar{t} = 8$ (panel (d)), there is no overlap between the two spectra and the system evolves into a nonconducting

state. This also explains why the phenomenon of negative differential conductance is robust against an additional positive onsite bias. Any further increase of the onsite energy separates the two energy spectra of the left and the right sides even farther so the nonconducting state remains. Importantly, this energetic mechanism applies to other types of setups for studying transport phenomena.

However, other possibilities may occur in interacting systems for large U/\bar{t} when a homogeneous conducting state is no longer favorable. From Eq. (4.6) and the discussion below Eq. (4.8), states could be generated that have an inhomogenous density which would give enough “energetic relief” to allow a macroscopic current to flow.² In the mean-field solution, however, such current-carrying state could not be found. Here we emphasize that the nonconducting state is *dynamically generated* and thus is very different from the widely-discussed Mott insulating phase at integer fillings, which is an equilibrium ground state. We now consider a higher-order approximation and also td-DMRG simulations.

4.4 Higher-order Correlations and td-DMRG

In order to determine the accuracy of the mean-field simulations above, we also perform simulations with higher-order correlations and with td-DMRG [98]. In the higher-order approximation, we keep two-particle correlations, rather than truncating at the single-particle level. In this approximation, we preserve the two particle correlation functions, i.e., we do not use a Wick decomposition at the two-particle level. Rather, we decompose the three-particle correlation functions into products of single-particle correlation

²We found density modulations in the *nonconducting* state, too.

functions and two-particle correlation functions, e.g.,

$$\begin{aligned} \left\langle c_{i\sigma}^\dagger c_{j\sigma} c_{k\sigma}^\dagger c_{l\sigma} c_{m\bar{\sigma}}^\dagger c_{n\bar{\sigma}} \right\rangle &= \frac{1}{3} \left(\left\langle c_{m\bar{\sigma}}^\dagger c_{n\bar{\sigma}} \right\rangle \left\langle c_{i\sigma}^\dagger c_{j\sigma} c_{k\sigma}^\dagger c_{l\sigma} \right\rangle \right. \\ &\quad + \left\langle c_{i\sigma}^\dagger c_{j\sigma} \right\rangle \left\langle c_{m\bar{\sigma}}^\dagger c_{n\bar{\sigma}} c_{k\sigma}^\dagger c_{l\sigma} \right\rangle - \left\langle c_{i\sigma}^\dagger c_{l\sigma} \right\rangle \left\langle c_{k\sigma}^\dagger c_{j\sigma} c_{m\bar{\sigma}}^\dagger c_{n\bar{\sigma}} \right\rangle \\ &\quad \left. + \delta_{jk} \left\langle c_{i\sigma}^\dagger c_{l\sigma} \right\rangle \left\langle c_{m\bar{\sigma}}^\dagger c_{n\bar{\sigma}} \right\rangle \right. \\ &\quad - \left\langle c_{k\sigma}^\dagger c_{j\sigma} \right\rangle \left\langle c_{i\sigma}^\dagger c_{l\sigma} c_{m\bar{\sigma}}^\dagger c_{n\bar{\sigma}} \right\rangle + \left\langle c_{k\sigma}^\dagger c_{l\sigma} \right\rangle \left\langle c_{i\sigma}^\dagger c_{j\sigma} c_{m\bar{\sigma}}^\dagger c_{n\bar{\sigma}} \right\rangle \\ &\quad \left. + \delta_{jk} \left\langle c_{i\sigma}^\dagger c_{l\sigma} c_{m\bar{\sigma}}^\dagger c_{n\bar{\sigma}} \right\rangle \right). \quad (4.9) \end{aligned}$$

This allows us to include all of the two-particle correlation functions in the simulation. Since there are three ways to decompose the three-particle correlation functions, we chose to average the contributions of each in order to increase the numerical stability of the simulation. We note that inclusion of the two-particle correlations is only a short time approximation and the simulations can become unstable for intermediate to long times. Thus we have restricted these simulations to short times. The results for the average current presented in the main text are therefore limited to relatively short time scales for large values of U . This means that the averaging partially truncates oscillations and there will be some artifacts associated with this truncation.

The details of the td-DMRG simulations are given in their respective figure captions. We note that td-DMRG has been applied to study the dynamics of different cold-atom systems [114].

Figure 4.5 shows the results for $U/\bar{t} = 2$, $N = 40$, and $N_{p\sigma} = 20$ for the three different methods. They all agree qualitatively, giving rise to a quasi steady state. Keeping track of the higher-order correlations significantly improves the accuracy of the simulation. Furthermore, the results suggest that for small U/\bar{t} the transient time to reach a quasi steady state is only a few t_0 while the duration of the QSSC can extend much longer. Thus for reasonably large lattices, the observation of an interaction-induced QSSC and the conducting-nonconducting transition is feasible.

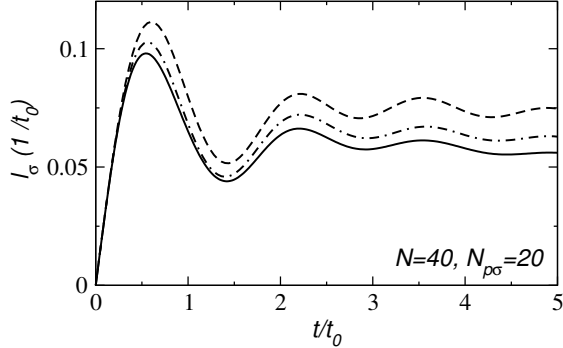


Figure 4.5: Current versus time for varying levels of approximation. The mean-field approximation (dashed line), the higher-order approximation including two-particle correlations (dash-dot), and td-DMRG (solid line) are shown for $U/\bar{t} = 2$. Here $N = 40$ and $N_{p\sigma} = 20$. For td-DMRG, we did a series of simulations using matrix-product state (MPS) dimensions 500, 2000, and 3000. The td-DMRG results shown are converged.

Figure 4.6 shows the average current versus U . We note that inclusion of higher order correlations limits our analysis to shorter times than above. This means that the averaging partially truncates oscillations and the effect of this partial truncation is to give a finite value to $\langle I_\sigma \rangle$ even when a longer average would give zero. This will be more prominent for shorter averages, i.e., in the absence of transient effects, one expects that the truncation will give a residual contribution of $\langle I_\sigma \rangle \propto 1/U$, as U gives the frequency scale of oscillations (for large U). The inset of Figure 4.6 gives this tail: for filling greater than $1/2$, the average current is consistent with this interpretation. For filling equal to $1/2$, the results are ambiguous. Most importantly, all methods clearly display the negative differential conductance, and, thus, this phenomenon should be observable in experiments.

If the initial state is not far from a band-insulator (see the cases with $N = 40$ and $N_{p\sigma} = 30, 35$), the td-DMRG simulations show a conducting-nonconducting transition for large U . Thus this dynamically generated conducting-nonconducting transition should be observable in experiments. For the half-filling initial state, a current carrying state is observed within our simulation range, but the magnitude of the current in this state is decreasing as U is increased as happened with the higher order correlation case.

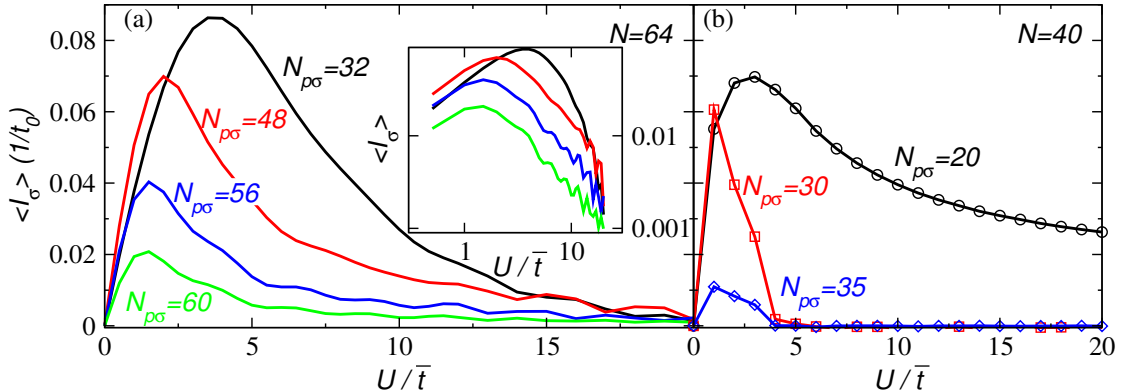


Figure 4.6: Average current versus U . (a) $\langle I_\sigma \rangle$ of the fermionic case with $N = 64$ and $N_{p\sigma} = 32, 48, 56, 60$ (labeled next to each curve) from the simulations with two-particle correlations. The averaged current is computed from $t = 0$ to $t = 2.5t_0$. The inset of the plot shows the average current plotted on a log scale, which shows that it does indeed vary as $1/U^\alpha$ where α tends towards 1 as the filling increases ($\alpha \approx 2.95, 1.59, 1.43, 1.29$ for $N_{p\sigma} = 32, 48, 56, 60$ respectively). (b) $\langle I_\sigma \rangle$ of the fermionic case with $N = 40$ and $N_{p\sigma} = 15, 20, 30, 35$ (labeled next to each curve) from td-DMRG with MPS dimension 500. Simulations with higher MPS dimension indicate that these are accurate to within about 5%. The averaged current is computed from $t = 5.0t_0$ to $t = 10.0t_0$. Similar to Figure 4.3, the average current initially increases with U and then decreases, thus giving negative differential conductance. The td-DMRG simulations indicate that a conducting-nonconducting transition can exist for large U for fillings larger than half filling.

4.5 Conclusion

In summary, we have shown that one may use time-dependent inhomogeneous interactions of ultra-cold atoms to explore non-equilibrium physics not easily realizable in conventional solid-state setups. For weak-interactions, the response of the system is similar to condensed matter systems where a bias is applied. This response is robust against possible transient behavior of the driving force. The application of inhomogeneous interactions gives rise to negative differential conductance, which is a many-body, atomic analog of this phenomenon in solid-state systems. Furthermore, a dynamically generated conducting-nonconducting transition is predicted from different simulations and its observation in experiments could provide another example of nonequilibrium phase

transitions. Our work sheds light on the physics of complex systems out of equilibrium and may help in the design of devices in the thriving field of atomtronics [115].

Chapter 5: Landauer’s Formula with Finite-Time Relaxation

The previous two Chapters examined transport in a closed-system configuration: a system initially starts in some ground state and then is perturbed and the dynamics are examined. In this Chapter, we shift our focus to examining transport in the context of a larger system, by including electronic reservoirs. These reservoirs act as electron sources and sinks and seek to establish a steady-state current across a region between them. We calculate the steady-state current when relaxation of electrons is present. We also demonstrate that a simple equation of motion emerges, which is suitable for efficiently simulating time-dependent transport. The work in this chapter was authored in collaboration with Kirill A Velizhanin and was published in Ref. [51].

5.1 Introduction

The prototypical example of electron transport in nano- and meso-scale junctions is a small conducting region connected to two electron reservoirs. When the confinement in this region is strong, the rigorous treatment of quantum effects becomes crucial. The Landauer formalism [54, 55] is a well-known method for describing these systems, which is based on an energy-dependent transmission probability for the region of interest. This method has been successfully applied to ballistic transport [116], quantized conductance [117, 118], quantum point contacts [119], cold-atom systems [29, 86], and

broadly in the area of nanoscale electronics [55, 120, 121]. However, the viewpoint on which the Landauer formula is based neglects the effect of relaxation mechanisms, the dynamics of the region of interest, and many-body interactions. Put differently, the text-book Landauer approach [55, 122, 123] implicitly assumes that deviation from the equilibrium distribution in the external reservoirs is negligible. Moreover, the relaxation of the electrons in the junction region is only due to the contact with the electrodes. When the timescale for relaxation at the electrodes is comparable to that in the junction, the physical behavior cannot be captured by the Landauer formalism.

An alternative method to calculate the transport properties is to work with a closed system and explicitly solve for the dynamics [55, 105, 110, 124]. This approach has been applied to study molecular conductance [125, 126] and induced cold atom transport [50, 85, 86], where the latter closely approximates a closed system, giving an ideal application of this approach. The limitation of this method, however, is that the recurrence time is proportional to the total system size, meaning that a large—and computationally expensive—reservoir is needed to fully eliminate transient effects and to examine dynamical perturbations on top of an otherwise steady-state current. This is not feasible in most situations, especially if one is interested in complex, time-dependent many-body systems or the effect of relaxation (which would require the explicit incorporation of additional degrees of freedom such as phonons).

Transport in time-dependent structures, however, has emerged at the forefront of applications. Electronic sequencing [127–134] (via tunneling current through base pairs) and sensing [135–142] (e.g., protein fluctuations on/nearby carbon nanotube and graphene devices), in particular, require a rigorous treatment of the interplay between transport and changes of the junction or molecular structure. In other words, if the local relaxation of electrons near the junction is slower or on the same timescale as the changes in the junction (typically picoseconds) the interaction between these two processes can dramatically influence transport. Practical real-time approaches to transport that are naturally suited to these systems are therefore necessary. The formalism introduced by Jauho, Meir and Wingreen [58, 143, 144] (which has been used to describe the conduction in a

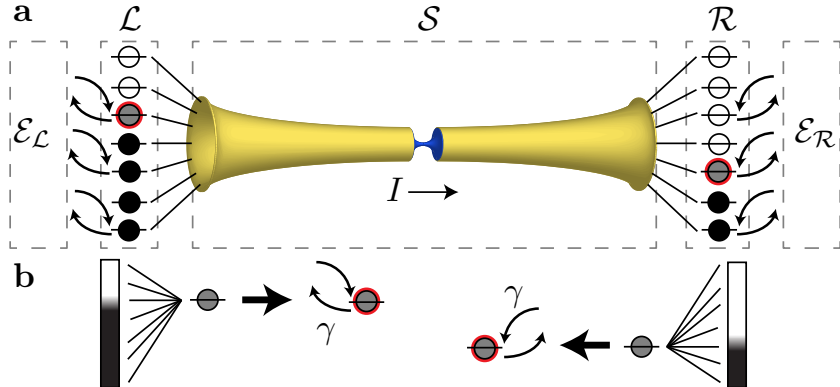


Figure 5.1: Schematic representation of the model. (a) System-reservoir-environment model, with yellow and blue representing the junction region (e.g., two leads connected by a junction)—the system of interest \mathcal{S} —and \mathcal{L} (\mathcal{R}) indicating the extended reservoirs. The presence of electron sources, sinks, and interactions (electron-electron, electron-phonon, etc.), here subsumed into the environments $\mathcal{E}_{\mathcal{L}(\mathcal{R})}$, causes the reservoirs to relax toward their respective equilibrium distributions, which, when an external bias is applied, will be at different chemical potentials. (b) Each reservoir state exchanges electrons with an environment (i.e., an external reservoir at some chemical potential), which gives rise to a non-zero relaxation rate γ . The imbalance of occupied states will drive a current through \mathcal{S} , where explicit (or implicit) relaxation mechanisms may or may not be present.

variety of systems, such as quantum dots [145–147], and layered semiconductors [148–150]) provides an exact formal solution to the time evolution, but involves two-time Green’s functions, making its use prohibitive in many applications. In this chapter, we show that in the absence of time dependence, one can recover the Landauer view with reasonably sized “extended reservoirs” and weak relaxation. The incorporation of explicit but finite reservoirs, however, also allows for one to examine the competition between time-dependence of the junction and the relaxation rate of the reservoir region.

In transport, external sources and sinks of electrons, together with electron-electron, electron-phonon, etc., interactions, maintain a potential difference across two large regions, which we call extended reservoirs. We develop an open system approach to transport that includes a finite electron lifetime representing the presence of these relaxation mechanisms. In particular, the extended reservoirs consist of a set of states

whose occupation is pushed towards equilibrium by the exchange of electrons with *implicit reservoirs* (the environment \mathcal{E}) at different chemical potentials. When a finite system is placed between them, an electric current will be driven across it. We derive a Landauer-like formula for this scenario and demonstrate that a finite relaxation time in the extended reservoirs gives rise to three distinct regimes of behavior, analogous to Kramers' turnover for chemical reactions [151]. A methodology similar to that below—one based on the concept of “extended reservoirs”—was proposed and developed for classical thermal transport [152, 153], where a corresponding crossover effect occurs (see also Ref. [154]).

5.2 Model

The Hamiltonian is $H = H_{\mathcal{L}} + H_{\mathcal{R}} + H_{\mathcal{S}} + H_{\mathcal{I}}$, where the explicit degrees of freedom are divided into three parts: the left extended reservoir (\mathcal{L}), the right extended reservoir (\mathcal{R}), and the system of interest (\mathcal{S}). The extended reservoir regions have a finite electron lifetime that pushes them towards equilibrium by allowing for the exchange of electrons with the external degrees of freedom in the implicit reservoir.¹ In other words, \mathcal{L} and \mathcal{R} are open to some larger environment \mathcal{E} (shown as $\mathcal{E}_{\mathcal{L}}$ and $\mathcal{E}_{\mathcal{R}}$ in Fig. 5.1), where the latter will be composed of degrees of freedom that are treated implicitly. Finally, $H_{\mathcal{I}}$ describes the interaction between \mathcal{S} and the left (\mathcal{L}) and right (\mathcal{R}) extended reservoirs. Figure 5.1 shows a schematic of this setup.

The left and right regions each contain N_r non-interacting electronic states with a Hamiltonian given by $H_{\mathcal{L}} = \sum_{k \in \mathcal{L}} \epsilon_k c_k^\dagger c_k$ and $H_{\mathcal{R}} = \sum_{k \in \mathcal{R}} \epsilon_k c_k^\dagger c_k$, where $k \in \mathcal{L}, \mathcal{R}$ indexes the single particle states and $c_k^\dagger (c_k)$ are their respective creation (annihilation) operators. The interaction Hamiltonian is described by $H_{\mathcal{I}} = \sum_{k \in \mathcal{L}, \mathcal{R}} \sum_{i \in \mathcal{S}} \hbar v_{ki} c_k^\dagger c_i + \text{h.c.}$, where $i \in \mathcal{S}$ indexes the system states (with associated operators c_i^\dagger, c_i). The v_{ki} are the hopping rates between the reservoir and system states. The method we describe will be

¹In some sense, we can say this is a grand canonical approach to transport when compared to the microcanonical approach of Ref. [105].

applicable to all dimensions, as this just changes the onsite energies in the Hamiltonian and hopping rates to the extended reservoirs. The system Hamiltonian, $H_{\mathcal{S}}$, is arbitrary, potentially including many-body or spin-dependent interactions, vibrational degrees of freedom, etc.

In the absence of \mathcal{S} , the extended reservoir states relax into their equilibrium occupations, i.e., their local density of electrons decays into a Fermi-Dirac distribution. The rate at which this occurs, denoted by γ , is controlled by the coupling strength between the reservoirs, \mathcal{L} and \mathcal{R} , and their environment, $\mathcal{E}_{\mathcal{L}(\mathcal{R})}$. Generically, γ captures the physical interaction with the environment that relax the reservoirs into equilibrium.² A lower bound on γ^{-1} can be estimated by the mean scattering time in the material, which is typically on the order of 1 fs to 10 fs for metals. However, γ is the relaxation rate to reach equilibrium, which can be much weaker (especially for, e.g., local disturbances to dissipate in confined geometries, at low temperature, or in the presence of weak electron-phonon interaction). Physically, each reservoir state is exchanging electrons with a larger external reservoir ($\mathcal{E}_{\mathcal{L}(\mathcal{R})}$) with an applied bias of $V_{\mathcal{L}(\mathcal{R})}$ and an infinite extent. The total externally applied bias is $V = V_{\mathcal{L}} - V_{\mathcal{R}}$, where we here take V to be in units of energy.

The general solution for the steady-states in this setup can be found by following the approach of Jauho, Meir, and Wingreen [144], where the reservoirs are taken to be infinite with a well-defined occupation and no relaxation. Indeed, when the whole $\mathcal{L} - \mathcal{S} - \mathcal{R}$ system is treated as some larger system \mathcal{S}' , the steady state is just the Meir-Wingreen solution, albeit with an unmanageably large number of degrees of freedom. Here, however, we are interested in calculating the transport properties of \mathcal{S} *by itself*, i.e., to what extent can the extended reservoirs \mathcal{L} and \mathcal{R} —finite in extent but with relaxation—capture the effect of infinite reservoirs in the normal approaches. As well, we want to determine what parameter ranges (e.g., realistic values of γ) are simulatable via a Markovian master equation approach. To this end, we will start with the Green's functions for the extended reservoir states uncoupled from the system, but still including

²The relaxation rate can also be energy dependent and this will reflect both the geometry and dimensionality of the whole setup. In this work, we take γ to be constant, independent of both k and \mathcal{L} or \mathcal{R} , for simplicity. This is easily relaxed, however.

a finite lifetime (note that, as we do in Sec. 6.1, one can start with all degrees of freedom treated explicitly, including $\mathcal{E}_{\mathcal{L}(\mathcal{R})}$, see Eq. (6.1)). For the lesser Green's function:

$$g_k^<(\omega) = \frac{i\gamma f_{\mathcal{L}(\mathcal{R})}(\omega)}{(\omega - \omega_k)^2 + \gamma^2/4}, \quad (5.1)$$

with $\hbar\omega_k = \epsilon_k$ and $f_{\mathcal{L}(\mathcal{R})}(\omega) = 1/(\exp[\beta(\hbar\omega - V_{\mathcal{L}(\mathcal{R})})] + 1)$ is the Fermi-Dirac distribution. This expression is within the wide-band approximation, see Sec. 6.1 for the general case. This leads to the single particle retarded and advanced Green's functions

$$g_k^{r(a)}(t, t') = \mp i\Theta(\pm t \mp t') \left\langle \{c_k^\dagger(t)c_k(t')\} \right\rangle = \mp i\Theta(\pm t \mp t') e^{-i\omega_k(t-t') - \gamma|t'-t|/2} \quad (5.2)$$

or $g_k^{r(a)}(\omega) = (\omega - \omega_k \pm i\gamma/2)^{-1}$ for the Fourier transform. The γ in both these equations reflects the finite lifetime of electrons in the extended reservoir regions. Starting with this broadened Green's function for the individual reservoir state, the steady-state current is

$$I = \frac{e}{2\pi} \int_{-\infty}^{\infty} d\omega [f_{\mathcal{L}}(\omega) - f_{\mathcal{R}}(\omega)] \times \text{tr} [\boldsymbol{\Gamma}^{\mathcal{L}}(\omega) \mathbf{G}^r(\omega) \boldsymbol{\Gamma}^{\mathcal{R}}(\omega) \mathbf{G}^a(\omega)]. \quad (5.3)$$

The quantity $\boldsymbol{\Gamma}_{ij}$ is the spectral density of the couplings between the system and the extended reservoirs

$$\boldsymbol{\Gamma}_{ij}^{\mathcal{L}(\mathcal{R})}(\omega) = \sum_{k \in \mathcal{L}(\mathcal{R})} v_{ik} v_{kj} \frac{\gamma}{(\omega - \omega_k)^2 + \gamma^2/4}, \quad (5.4)$$

with $i, j \in \mathcal{S}$. $\mathbf{G}^{r(a)}(\omega)$ are the exact retarded and advanced Green's functions for the system only but in the presence of the left and right extended reservoirs and including relaxation in the latter.

Equation (5.3) is similar to the traditional Landauer formula. However, the density of states of a single extended reservoir state is broadened to a Lorentzian due to the inclusion of a finite relaxation time. When no interactions are present, Eq. (5.3) can be interpreted in terms of a relaxation-dependent transmission coefficient, $T_\gamma = \text{tr}[\boldsymbol{\Gamma}^{\mathcal{L}} \mathbf{G}^r \boldsymbol{\Gamma}^{\mathcal{R}} \mathbf{G}^a]$.

This relaxation gives rise to different physical regimes of behavior and also an effective equation of motion that can be used to examine transport in more complex time-dependent scenarios. We first describe the different regimes of behavior for an example system.

5.3 Results

When the reservoir states are symmetrically coupled to the system, i.e., when the distribution of energies ϵ_k and couplings v_{ki} are the same for each $k \in \mathcal{L}$ and its corresponding $k \in \mathcal{R}$, the spectral density, Eq. (5.4), is proportional to the imaginary part of the inverse of $\mathbf{G}^{r(a)}(\omega)$. This results in a simplified expression for the current,

$$I = -\frac{e\gamma}{2\pi} \sum_{k \in \mathcal{L}} \sum_{i,j \in \mathcal{S}} v_{ik} v_{kj} \times \int_{-\infty}^{\infty} d\omega \frac{[f_{\mathcal{L}}(\omega) - f_{\mathcal{R}}(\omega)]}{(\omega - \omega_k)^2 + \gamma^2/4} \text{Im}[\mathbf{G}_{ij}^r(\omega)]. \quad (5.5)$$

In the example below, we make use of this simplified expression.

5.3.1 Single-Site Homogeneous System

Equation (5.3) is valid for any system—including those with many-body interactions—with a finite relaxation time. In what follows, however, we will focus on a homogeneous system in which the combined $\mathcal{L} - \mathcal{S} - \mathcal{R}$ system is a 1D lattice with hopping rate J : $H = \sum_{n \in \mathcal{L}, \mathcal{R}, \mathcal{S}} \hbar J (c_n^\dagger c_{n+1} + \text{h.c.})$. The quantity J sets the frequency scale, where the bandwidth $W = 4J$. Note that in this example, the total coupling to the system and the bandwidth are both determined by J . Typically, J^{-1} is in the range 0.1 fs to 1 fs for conducting materials. We choose to work with hopping rates rather than energies as this gives more transparent expressions.

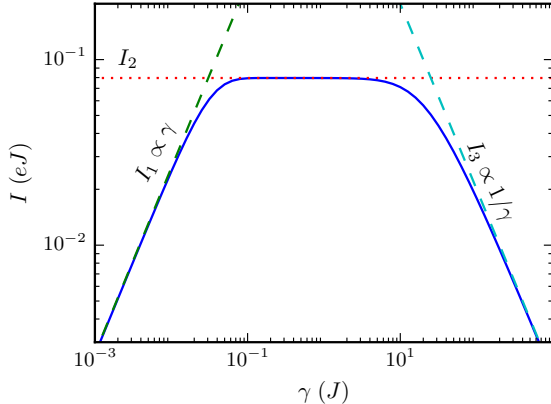


Figure 5.2: Regimes of the electronic current. The steady-state current, Eq. (5.5) (or Eq. (5.3)), of the single-state system connected to two 1D extended reservoirs of size $N_r = 64$. The potential difference is $V = 0.5J\hbar$ and the temperature is given by $\beta = 40(J\hbar)^{-1}$. The dashed lines show the approximations in the small and large γ regimes, and the dotted line is the Landauer calculation of the closed system, \mathcal{S} , with infinite \mathcal{L} and \mathcal{R} without relaxation. The small γ regime has a current increasing linearly with γ , as it dominates the rate at which electrons flow through the whole setup. In the large γ regime, the fast relaxation localizes electrons in the extended reservoir, causing the current to decay as $1/\gamma$. In the intermediate relaxation regime, the current matches that from a Landauer calculation.

The extended reservoir portion of H can be directly diagonalized via a sine transformation.³ That is, given $k \in \{1, \dots, N_r\}$, $\omega_k = -W/2 \cos[k\pi/(N_r + 1)]$. We can express the couplings with a single index, v_k for $k \in \mathcal{L}, \mathcal{R}$ (instead of v_{ki}). Using this notation, the couplings are

$$v_k = J\sqrt{2/(N_r + 1)} \sin[k\pi/(N_r + 1)]. \quad (5.6)$$

Again, in this special case of a uniform 1D lattice, J sets the hopping rate in both the extended reservoir region and between the system and extended reservoirs. Additionally, we will take the system to be a single site with no onsite energy so that $\mathbf{G}^{r(a)}(\omega) = 1/\left(\omega - 2 \sum_k v_k^2 g_k^{r(a)}(\omega)\right)$, where the sum over k is in either \mathcal{L} or \mathcal{R} (the factor of 2 reflects the symmetry of the setup).

³The transformation \mathcal{U} is applied to the subset of states in the reservoirs, and so the couplings to \mathcal{S} are determined by its matrix elements.

Figure 5.2 shows the calculation of the current I from Eq. (5.5) (or Eq. (5.3)) as a function of the relaxation rate γ for a reservoir size $N_r = 64$. There are three regimes visible: (1) a small γ regime with current I_1 , (2) an intermediate regime with I_2 , and (3) a large γ regime with I_3 . We first discuss the intermediate regime.

5.3.2 Intermediate Relaxation

Figure 5.2 shows that there is an intermediate range of γ for which the current is approximately flat. That is, in this crossover region between small and large values of γ , a plateau forms and subsequently elongates as the size of the extended reservoir increases (see Fig. 5.3). The current in this regime is the same as that predicted by a Landauer calculation for \mathcal{S} alone. That calculation gives the current as $I_2 = e/(2\pi) \int_{-W/2}^{W/2} d\omega [f_{\mathcal{L}}(\omega) - f_{\mathcal{R}}(\omega)] T(\omega)$. In linear response, this yields

$$I_2 \approx eVT(\omega_F)/(2\pi\hbar), \quad (5.7)$$

where $\hbar\omega_F$ is the Fermi level. In this example, the transmission coefficient at the Fermi level is $T(\omega_F) = 1$ and the plateau comes at the quantum of conductance, $I_2(\beta \gg J\hbar) \approx eV/(2\pi\hbar)$ (the transmission coefficient through part of a homogeneous lattice is unity, $T(\omega) = 1$, for all frequencies).⁴

Perfect transmission at the Fermi level ($T(\omega_F) = 1$) remains even if the hopping rate from the extended reservoir into the system is different (i.e., even if we have an inhomogeneity of the hopping rates at the interface to the system). In other systems, or in nonlinear response, though, the current—i.e., the level of the plateau—will be a complicated function of the total setup. As we discuss below, this will change when the current transitions into the other two regimes.

⁴At high temperature the current is $I_2(\beta \ll J\hbar) \approx eJ\beta V/(2\pi)$.

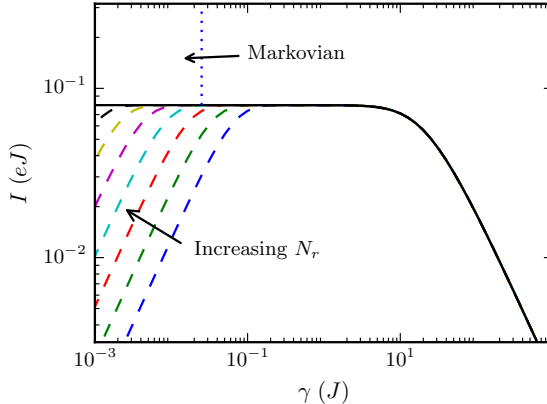


Figure 5.3: Expansion of the plateau. The steady-state current as a function of the relaxation rate γ for the $N_r \in \{32, 64, 128, 256, \dots\}$ systems (dashed lines) and the $N_r \rightarrow \infty$ limit, I_{23} (solid line). The parameters of the system are the same as in Fig. 5.2. In the limit that $N_r \rightarrow \infty$ and then $\gamma \rightarrow 0$, we recover the standard Landauer current. The vertical dotted line demarcates the regions where the Markovian master equation is valid and not valid. Since the size of the plateau grows linearly with N_r , the plateau will eventually extend into the region where the Markovian equation is valid, allowing for transport in this intermediate plateau regime to be simulated with the much simpler Markovian approach.

5.3.3 Small Relaxation

Figure 5.2 shows that the current increases linearly with γ when it is small. In this regime, electrons move from the left extended reservoir into the system much faster than the implicit reservoirs replenish the electrons in \mathcal{L} (and similarly for \mathcal{R}). The rate of the replenishment is the relaxation rate γ , as this determines how fast the states return back to their equilibrium occupation. Thus, when γ is small, electrons cannot be restored rapidly enough and this rate becomes the bottleneck for the current, and hence the current is essentially dependent only on γ .

When the system is noninteracting and γ is much less than the state spacing ($\gamma \ll W/N_r$), energy conservation guarantees that an electron coming out of state k (i.e., at energy ϵ_k) on the left, must exit the system at the same energy on the right. This allows the current to be broken into contributions from pairs of states, for which the pair can

also be labeled by k in this symmetric setup. The current flowing into the left reservoir state k from the environment $\mathcal{E}_{\mathcal{L}}$ is $I_k^{\mathcal{L}} = e\gamma(f_k^{\mathcal{L}} - n_k^{\mathcal{L}})$ and the current out of that state into the system is $I_k^{\mathcal{L}\mathcal{S}} = e\sigma(n_k^{\mathcal{L}} - n^{\mathcal{S}})$, where $f_k^{\mathcal{L}(\mathcal{R})}$ is the Fermi-Dirac distribution evaluated at the reservoir state frequency $f_{\mathcal{L}(\mathcal{R})}(\omega_k)$ and σ is the particle flow rate from the reservoir state into the system. Similar rate equations hold on the right side. In the steady state ($I_k \equiv I_k^{\mathcal{L}} = I_k^{\mathcal{L}\mathcal{S}} = \dots$) and when $\gamma \ll \sigma$ (i.e., the relaxation γ has to be weak enough that electrons are injected into an extended reservoir state much more slowly than they move into the system and are subsequently taken away from the interface between the system and extended reservoir), these equations give $I_k \approx e(\gamma/2)(f_k^{\mathcal{L}} - f_k^{\mathcal{R}})$, where $\gamma/2$ is the “reduced γ ” (i.e., it reflects that there are two interfaces, one at the left and one at the right). For different relaxation rates in \mathcal{L} and \mathcal{R} , the relevant quantity would be $\gamma_{\mathcal{L}}\gamma_{\mathcal{R}}/(\gamma_{\mathcal{L}} + \gamma_{\mathcal{R}})$. Summing over the contribution from all states k , the total current in this regime is

$$I_1 \approx e\gamma/2 \sum_k (f_k^{\mathcal{L}} - f_k^{\mathcal{R}}). \quad (5.8)$$

The sum over k is over a single set of states in the left or right, which are identical in the symmetric setup. Figure 5.2 plots Eq. (5.8) along with the full solution, showing agreement for small γ .

Essentially, Eq. (5.8) is just $e\gamma/2$ times a particle bias: There are $\sum_k (f_k^{\mathcal{L}} - f_k^{\mathcal{R}})$ open channels in the bias window—where an electron can move from an occupied state k on the left and go to an unoccupied state k on the right—and each contributes $e\gamma/2$ to the current. We note that the physics of this regime is the same as that observed in weakly coupled quantum dot systems, [155] in which case γ reflects a weak tunneling rate to the external electrodes which limits how fast the dot at the boundary can equilibrate with the electrode.

The transition from the small to intermediate regimes occurs when the current from Eq. (5.8) intersects the plateau current, Eq. (5.7). We can approximate Eq. (5.8) by $e\gamma/2(V/\hbar)N_r/W$, where V/\hbar is the bias window in terms of frequency, W/N_r is the frequency spacing of the reservoir states, and, thus $(V/\hbar)/(W/N_r)$ gives the number of

states in the bias window.⁵ The γ at which the transition occurs, which we will denote by γ_{12} , is

$$\gamma_{12} \approx W/(\pi N_r). \quad (5.9)$$

This value decreases inversely with N_r . Indeed, as seen in Fig. 5.3, this is responsible for the increasing size of the plateau region, as the transition to the large γ region is independent of N_r (which we will see below).

We note that this transition γ is equivalent to the condition necessary to be in the small gamma regime, $\gamma \ll W/N_r$. In more complex systems, or even just in nonlinear response, the transition γ can be dependent on many other factors besides just the mode spacing, such as the hopping rate to the system, the bias, etc. In other words, the transition from small to intermediate γ depends on the details of the setup.

5.3.4 Large Relaxation

When γ becomes large, Fig. 5.2 shows that the current “turns over” and starts to decay as $1/\gamma$. The strong relaxation (i.e., the fast relaxation rate) in this regime is effectively localizing electrons in the extended reservoir region. For currents to flow, electrons must remain coherent between the extended reservoir and the system. The relaxation limits this coherence to a time $\approx 1/\gamma$ and therefore the current is suppressed by this factor.

Alternatively, this can be seen by starting with Eq. (5.5). There, the Lorentzian is approximately constant ($1/\gamma$) in the relevant region of integration and the Green’s functions for the reservoir states, $g_k^{r(a)}$, are purely imaginary. The density of states, $\text{Im}[\mathbf{G}^r]$, is dominated by the contribution from the system in this example (see Sec. 5.3.4 for more details). In linear response, this gives

$$I_3 \approx \frac{e}{2\pi} \left(\frac{4\pi J^2}{\gamma} \right), \quad (5.10)$$

⁵Note that N_r should also be sufficiently large so that a significant number of states are within the bias window.

so long as $V \neq 0$. That is, the strong relaxation renormalizes the coupling to J^2/γ and, thus, the total electron flow through \mathcal{S} is limited by this factor.⁶ This also shows that the current in the large γ regime is independent of N_r , with the exception of potential discretization effects (when N_r is very small) that can cause mismatches in energy, and that the current is independent of the bias in this regime for the particular example we discuss.

Just as with the small γ regime, we can find the transition into the large γ regime. This occurs at $\gamma_{23} \approx 4\pi J^2 \hbar / V$, where we have denoted the transition γ as γ_{23} . Thus, while the behavior of the current in the large γ regime is independent of bias, the transition to this regime is dependent on the bias—decreasing the bias makes this transition occur at increasingly large values of γ .

We note that, unlike γ_{12} and γ_{23} , how the small and large γ behavior varies with γ is generally independent of the form of the system and the reservoir dispersion relation, but rather only depends on characteristic quantities such as the total coupling strength (between the system and extended reservoir) and relaxation rate.

5.3.5 Reservoir Continuum Limit

The $N_r \rightarrow \infty$ limit can be taken in Eq. (5.3) to regain a macroscopic electron reservoir, but with a finite relaxation time. In our example setup, the extended reservoirs become semi-infinite 1D lattices on each side. For this case, we can find the self-energy through either a recursion relation [86, 87] or by integrating the states directly:

$$\Sigma^{r(a)}(\omega) = \sum_k \frac{v_k^2}{\omega - \omega_k \pm i\gamma/2} \rightarrow \int \frac{v(\omega')^2 D(\omega') d\omega'}{\omega - \omega' \pm i\gamma/2}, \quad (5.11)$$

⁶This expression depends on the hopping rate to the system rather than the hopping rate in the extended reservoirs. As we show in Sec. 6.2.3, the current is related to the difference in real space occupation of the sites immediately adjacent to \mathcal{S} for the Markovian approach discussed below.

with $D(\omega') = dk/d\omega_k|_{\omega_k=\omega'}$. This expression gives a self-energy

$$\Sigma^{r(a)}(\omega) = \frac{8J^2}{W^2} \left(\omega \mp i\frac{\gamma}{2} - i\sqrt{\frac{W^2}{4} - \left(\omega \mp i\frac{\gamma}{2}\right)^2} \right). \quad (5.12)$$

Using this in Eq. (5.3) or Eq. (5.5) (with $\Gamma = 2\text{Im}\Sigma$) provides a semi-analytic expression for the exact current through the system in the infinite N_r limit, denoted by I_{23} . Figure 5.3 shows this quantity together with the solution for several finite N_r reservoirs.⁷ These show that as N_r increases the plateau will continually grow and, when $N_r \rightarrow \infty$, the small γ regime will be eliminated entirely.

The results above are for steady-state currents, which can be calculated from exact treatment of the $\mathcal{L} - \mathcal{S} - \mathcal{R}$ system. However, this neglects time-dependent effects present in \mathcal{S} . As we show in Sec. 6.2.3, Eq. (5.3) also describes the steady-state solution of the Markovian master equation (see also Eq. (2.22) from Sec. 2.3.1)

$$\dot{\rho} = -\frac{i}{\hbar} [H, \rho] + \sum_k \gamma_{k+} \left(c_k^\dagger \rho c_k - \frac{1}{2} \left\{ c_k c_k^\dagger, \rho \right\} \right) + \sum_k \gamma_{k-} \left(c_k \rho c_k^\dagger - \frac{1}{2} \left\{ c_k^\dagger c_k, \rho \right\} \right) \quad (5.13)$$

in the small γ regime and in part of the intermediate plateau region (so long as N_r is sufficiently large, see Fig. 5.3). This type of equation has been applied previously [46, 156–158]. It is often taken as a phenomenological equation for all regimes of γ , not as a weak-coupling approximation to a memory-less reservoir [42]. Our complete solution to both the full model (for all γ) and its Markovian counterpart enables us to put rigorous bounds on the latter’s validity, which we will now discuss.

In Eq. (5.13), the terms $\gamma_{k+} = \gamma f_k^\alpha$ and $\gamma_{k-} = \gamma(1 - f_k^\alpha)$, where $\alpha = \mathcal{L}(\mathcal{R})$ when $k \in \mathcal{L}(\mathcal{R})$, relax the extended reservoirs into an equilibrium defined by their isolated Hamiltonian when $H_{\mathcal{I}}$ is absent. That is, unlike the setup described above, this equilibrium is for the extended reservoir states at fixed energy $\hbar\omega_k$. This coincides with the concept of equilibrium above only when the broadening is sufficiently small. Larger γ , therefore, can give rise to unphysical behavior, such as residual currents at zero bias

⁷In addition, the $N_r \rightarrow \infty$ result can be expanded for small γ , yielding the lowest order contribution to the current as given by Landauer, $I_{23} \approx I_2 + O(\gamma^2)$.

(see Sec. 6.3). In particular, the relaxation in the extended reservoirs must be smaller than the thermal relaxation, $\gamma \ll 1/\beta\hbar$ (or, in terms of timescales, $\gamma^{-1} \gg 25$ fs at room temperature), otherwise electron occupation can be smeared well above the Fermi level. As well, if one has asymmetric \mathcal{L} and \mathcal{R} extended reservoirs—with the asymmetry characterized by an energy offset δ —one needs $\gamma \ll W^3V/\delta J^2\hbar$. Taking γ and N_r such that the current is on the plateau, $\gamma \approx W/N_r$, gives a requirement on the extended reservoir size, $N_r \gg \delta/V$, when δ is finite.⁸ This less strict condition (when compared to $\gamma \ll 1/\beta\hbar$) guarantees that superfluous currents will be negligible compared to the actual current at finite bias. Within these regimes, the Markovian master equation allows for the calculation of the *full time dynamics*. This formalism allows for the simulation of time-dependent effects or interactions and, notably, does so without the use of two-time Green’s functions or the use of memory kernels, which both drastically increase the complexity of the simulations.

5.4 Conclusion

In summary, we developed the concept of extended reservoirs to examine the effect of relaxation on transport and the validity of a Markovian master equation approach. In addition to providing the full, exact solution to both the Markovian and non-Markovian cases, we showed that the current displays a crossover behavior as the relaxation rate is varied, with a weak coupling limit proportional to γ and a strong coupling limit proportional to $1/\gamma$. These two regimes are “relaxation” dominated. The Landauer regime can be simulated through the use of a finite number of reservoir states and controlling the relaxation rate to be between these two regimes. The physical behavior in the presence of a finite reservoir is analogous to Kramers’ problem and thermal transport [152].

This approach naturally leads to the Markovian master equation, Eq. (5.13), for small-to-intermediate γ , which gives a suitable starting point for studying the real-time behavior

⁸Without an asymmetry, the anomalous current from the left reservoir to the right is canceled by the anomalous current from right to left.

of the current where the junction region is time-dependent. This formalism allows the electronic reservoirs to respond to dynamical components of the system (such as structural and energetic fluctuations) and relax back to equilibrium at a finite rate. The method, therefore, can be applied to help understand the role of fluctuations in determining transport properties, to assess the effectiveness of electronic sensing in aqueous solution, and to give a unified approach to simulating nanoscale devices out of equilibrium.

Chapter 6: Derivations and Analysis of Finite-Time Relaxation

Chapter 5 focused primarily in the physical consequences of a finite relaxation time and the associated electronic current. In this Chapter, we take an in-depth look at the mathematical derivation of the equations used, following the first principles derivations from the explicit forms of the Green's functions. We also examine the consequences of using the master equation, Eq. (5.13), as the basis for numerical calculations without regard to the regimes of validity.

6.1 Steady-State Current Derivations

The expressions from the previous chapter are based on a derivation of the steady-state current using the equilibrium condition of a single extended reservoir site. What follows in this section is a more complete derivation of the steady-state current.

6.1.1 Single Extended Reservoir State Green's Function

Let us consider a single electronic level of energy $\hbar\omega_k$ connected to a manifold of non-interacting states that comprise the *implicit* reservoir \mathcal{E}_k . The index k denotes the extended reservoir state that these states are coupled to. The $\mathcal{E}_{\mathcal{L}(\mathcal{R})}$ from earlier are

composed of all \mathcal{E}_k for $k \in \mathcal{L}(\mathcal{R})$. The Hamiltonian of this partial system is

$$H_k = \hbar\omega_k c_k^\dagger c_k + \sum_{\alpha \in \mathcal{E}_k} \hbar\omega_\alpha c_\alpha^\dagger c_\alpha + \sum_{\alpha \in \mathcal{E}_k} \hbar t_\alpha (c_\alpha^\dagger c_k + c_k^\dagger c_\alpha). \quad (6.1)$$

This Hamiltonian describes the systems shown in Fig. 5.1(b) above. For an implicit reservoir state α , the *isolated* Green's functions are

$$g_\alpha^>(t, t') = -\imath[1 - f(\omega_\alpha)]e^{-\imath\omega_\alpha(t-t')-\eta|t-t'|}, \quad (6.2)$$

$$g_\alpha^<(t, t') = \imath f(\omega_\alpha)e^{-\imath\omega_\alpha(t-t')-\eta|t-t'|}, \quad (6.3)$$

$$g_\alpha^r(t, t') = \theta(t - t') [g_\alpha^>(t, t') - g_\alpha^<(t, t')], \quad (6.4)$$

and

$$g_\alpha^a(t, t') = -\theta(t' - t) [g_\alpha^>(t, t') - g_\alpha^<(t, t')]; \quad (6.5)$$

or, in terms of their Fourier transforms,

$$g_\alpha^>(\omega) = -2\pi\imath[1 - f(\omega_\alpha)]\delta(\omega - \omega_\alpha), \quad (6.6)$$

$$g_\alpha^<(\omega) = 2\pi\imath f(\omega_\alpha)\delta(\omega - \omega_\alpha), \quad (6.7)$$

$$g_\alpha^r(\omega) = 1/(\omega - \omega_\alpha + \imath\eta), \quad (6.8)$$

and

$$g_\alpha^a(\omega) = 1/(\omega - \omega_\alpha - \imath\eta), \quad (6.9)$$

where η is the infinitesimal positive number and $f(\omega)$ is the Fermi-Dirac distribution. The subscript α on g_α is used to distinguish it from an extended reservoir state Green's functions (g_k) or the full system Green's functions (\mathbf{G}_{ij}) as used for the $\mathcal{L} - \mathcal{S} - \mathcal{R}$ system. For the interaction of one level with all the other levels, Eq. (6.1), we have (symbolically, on the Keldysh contour) $g_k = g_{0k} + g_{0k}\Sigma_k g_k$, with g_{0k} being the single

isolated *extended* reservoir site. Using the relation between on-contour and real-time non-equilibrium Green's functions [58], for the retarded Green's function we have

$$g_k^r(\omega) = g_{0k}^r(\omega) + g_{0k}^r(\omega)\Sigma_k^r(\omega)g_k^r(\omega), \quad (6.10)$$

where

$$\Sigma_k^r(\omega) = \sum_{\alpha \in \mathcal{E}_k} t_{\alpha}^2 g_{\alpha}^r(\omega) = \frac{1}{2\pi} \int d\omega' \frac{\gamma(\omega')}{\omega - \omega' + i\eta}. \quad (6.11)$$

Here, $\gamma(\omega) = 2\pi \sum_{\alpha} t_{\alpha}^2 \delta(\omega - \omega_{\alpha})$. Evaluating the integral, one obtains

$$\Sigma_k^r(\omega) = \frac{1}{2\pi} \mathcal{P} \int d\omega' \frac{\gamma(\omega')}{\omega - \omega'} - \frac{i\gamma(\omega)}{2} = E_k(\omega) - \frac{i\gamma(\omega)}{2}, \quad (6.12)$$

where $E_k(\omega)$ is a frequency-dependent energy shift and $\gamma(\omega)$ is a frequency-dependent relaxation rate. Similarly, the lesser self-energy is evaluated as

$$\Sigma_k^<(\omega) = \sum_{\alpha \in \mathcal{E}_k} t_{\alpha}^2 g_{\alpha}^<(\omega) = i\gamma(\omega)f(\omega). \quad (6.13)$$

The retarded Green's function of the extended reservoir site then becomes

$$g_k^r(\omega) = \frac{1}{\omega - [\omega_k + E_k(\omega)] + i\gamma(\omega)/2}. \quad (6.14)$$

As is seen, “friction” is in general non-Markovian, since the dephasing rate $\gamma(\omega)$ is frequency-dependent. The frequency shift, $E_k(\omega)$, is also non-Markovian in the same sense. Now let us find the full lesser Green's function. To this end we will use the Keldysh equation [58, 144]

$$g_k^<(\omega) = g_k^r(\omega)\Sigma_k^<(\omega)g_k^a(\omega), \quad (6.15)$$

resulting in

$$g_k^<(\omega) = \frac{i\gamma(\omega)f(\omega)}{(\omega - \omega_k - E_k(\omega))^2 + \gamma^2(\omega)/4}. \quad (6.16)$$

The important fact here is that the Fermi-Dirac distribution here is not evaluated at ω_k or at any other fixed frequency. Instead, it is evaluated at ω and, therefore, this factor is the same (at fixed ω) for any Green's function of any site within the same reservoir. In particular, it guarantees that the current vanishes when the Fermi-Dirac distribution is the same for the two extended reservoirs.

The often used wide band approximation would result in ω -independent γ and vanishing E_k . In this approximation, the result for the lesser Green's function is

$$g_k^<(\omega) = \frac{i\gamma f(\omega)}{(\omega - \omega_k)^2 + \gamma^2/4}. \quad (6.17)$$

In a similar manner, the retarded Green's function is

$$g_k^r(\omega) = \frac{1}{\omega - \omega_k + i\gamma/2}. \quad (6.18)$$

Accordingly, one has, using the identity $g_k^r(\omega) = [g_k^a(\omega)]^*$,

$$g_k^<(\omega) = -f(\omega) [g_k^r(\omega) - g_k^a(\omega)]. \quad (6.19)$$

6.1.2 Landauer-like Formula

We are following a notation similar to the original Meir-Wingreen paper [143]. The Hamiltonian of the system is

$$H = \sum_{k \in \mathcal{L}, \mathcal{R}} \epsilon_k c_k^\dagger c_k + \sum_{k \in \mathcal{L}, \mathcal{R}} \sum_{i \in \mathcal{S}} \hbar (v_{ki} c_k^\dagger c_i + v_{ik} c_i^\dagger c_k) + H_{\mathcal{S}}, \quad (6.20)$$

with $\epsilon_k = \hbar\omega_k$. Unlike the Meir-Wingreen scenario where such a Hamiltonian fully describes the steady-state since the sizes of left and right reservoirs are assumed to be infinite, here we take a finite number of extended reservoir states, but each such site k is connected to an implicit reservoir according to the Hamiltonian (6.1).

The time-dependent current from the left reservoir to the system can be written as [143]

$$I(t) = e \sum_{k \in \mathcal{L}} \sum_{j \in \mathcal{S}} \left[v_{kj} \mathbf{G}_{jk}^<(t, t) - v_{jk} \mathbf{G}_{kj}^<(t, t) \right]. \quad (6.21)$$

When the steady state is established, we can take the Fourier transform,

$$I = e \sum_{k \in \mathcal{L}} \sum_{j \in \mathcal{S}} \int \frac{d\omega}{2\pi} \left[v_{kj} \mathbf{G}_{jk}^<(\omega) - v_{jk} \mathbf{G}_{kj}^<(\omega) \right]. \quad (6.22)$$

Since the reservoir sites are non-interacting (in a two- or more-electron sense) we have the following Dyson equation [144]

$$G_{kj}^<(\omega) = \sum_{i \in \mathcal{S}} v_{ki} \left[g_k^r(\omega) \mathbf{G}_{ij}^<(\omega) + g_k^<(\omega) \mathbf{G}_{ij}^a(\omega) \right], \quad (6.23)$$

or equivalently

$$G_{ik}^<(\omega) = \sum_{j \in \mathcal{S}} v_{jk} \left[\mathbf{G}_{ij}^r(\omega) g_k^<(\omega) + \mathbf{G}_{ij}^<(\omega) g_k^a(\omega) \right]. \quad (6.24)$$

Using these identities, Eq. (6.22) can be rewritten as

$$I = e \sum_{k \in \mathcal{L}} \sum_{i,j \in \mathcal{S}} \int \frac{d\omega}{2\pi} v_{ki} v_{jk} \left\{ g_k^<(\omega) [\mathbf{G}_{ij}^r(\omega) - \mathbf{G}_{ij}^a(\omega)] - [g_k^r(\omega) - g_k^a(\omega)] \mathbf{G}_{ij}^<(\omega) \right\}. \quad (6.25)$$

We emphasize that even though $g_k(\omega)$ are single-particle non-interacting Green's functions, the corresponding quasiparticles do have finite lifetime because of their coupling to the implicit reservoirs, which is different from the original Meir-Wingreen formulation. For example, $g_k^>(\omega)$ are not delta functions with respect to ω , but rather Lorentzians (when the wide band limit is taken, Eq. (6.17)).

To proceed further we use (i) the Keldysh equation [58, 144], $\mathbf{G}^> = \mathbf{G}^r \Sigma^> \mathbf{G}^a$, and (ii) that the self-energy due to the interaction with reservoir sites is $\Sigma_{ij}^{r(a)} = \sum_k v_{ik} v_{kj} g_k^{r(a)}$, and (iii) the linear relation between real-time Green's functions $\mathbf{G}^> - \mathbf{G}^< = \mathbf{G}^r - \mathbf{G}^a$ [58].

Using these identities the current can be rewritten as

$$\begin{aligned} I = e \sum_{i,j \in S} \sum_{\alpha,\beta \in S} \sum_{k \in \mathcal{L}} \sum_{l \in \mathcal{L}, \mathcal{R}} & \int \frac{d\omega}{2\pi} v_{ki} v_{jk} v_{\alpha l} v_{l\beta} \mathbf{G}_{i\alpha}^r(\omega) \mathbf{G}_{\beta j}^a(\omega) \\ & \times \{g_k^<(\omega) [g_l^r(\omega) - g_l^a(\omega)] - [g_k^r(\omega) - g_k^a(\omega)] g_l^<(\omega)\}. \end{aligned} \quad (6.26)$$

Considering the equilibrium property of the isolated state k , Eq. (6.19), one gets

$$\begin{aligned} I = -e \sum_{i,j \in S} \sum_{\alpha,\beta \in S} \sum_{k \in \mathcal{L}} \sum_{l \in \mathcal{R}} & \int \frac{d\omega}{2\pi} v_{ki} v_{jk} v_{\alpha l} v_{l\beta} \mathbf{G}_{i\alpha}^r(\omega) \mathbf{G}_{\beta j}^a(\omega) \\ & \times [g_l^r(\omega) - g_l^a(\omega)] [g_k^r(\omega) - g_k^a(\omega)] \{f_{\mathcal{L}}(\omega) - f_{\mathcal{R}}(\omega)\}. \end{aligned} \quad (6.27)$$

It is clearly seen that once the Fermi-Dirac distribution becomes identical on the left and on the right, the current vanishes. Actually, any partial current also vanishes, i.e., the current for a specific choice of indices $m, n, \alpha, \beta, k, l$ and frequency ω , as of course is expected due to the necessary detailed balance at equilibrium.

A concise expression for the current can be written by introducing the spectral density

$$\Gamma_{ji}^{\mathcal{L}(\mathcal{R})}(\omega) = i \sum_{k \in \mathcal{L}(\mathcal{R})} v_{jk} v_{ki} [g_k^r(\omega) - g_k^a(\omega)], \quad (6.28)$$

and the expression for the current becomes

$$I = \frac{e}{2\pi} \sum_{i,j,\alpha,\beta \in S} \int_{-\infty}^{\infty} d\omega [f_{\mathcal{L}}(\omega) - f_{\mathcal{R}}(\omega)] \times \Gamma_{ij}^{\mathcal{L}}(\omega) \mathbf{G}_{j\alpha}^r(\omega) \Gamma_{\alpha\beta}^{\mathcal{R}}(\omega) \mathbf{G}_{\beta i}^a(\omega). \quad (6.29)$$

Using the matrix notation,

$$I = \frac{e}{2\pi} \int_{-\infty}^{\infty} d\omega [f_{\mathcal{L}}(\omega) - f_{\mathcal{R}}(\omega)] \times \text{tr} [\boldsymbol{\Gamma}^{\mathcal{L}}(\omega) \mathbf{G}^r(\omega) \boldsymbol{\Gamma}^{\mathcal{R}}(\omega) \mathbf{G}^a(\omega)]. \quad (6.30)$$

This expression is Eq. (5.3) from Sec. 5.2.

6.1.3 Small Relaxation, Continuum Limit

As an example, we examine a system that is a single noninteracting state. In this case, the continuous form for the extended reservoir self-energy from integrating the single site Green's functions, Eq. (5.12) from Sec. 5.3.5, is

$$\Sigma^{r(a)}(\omega) = \left(\omega \mp i\gamma/2 - i\sqrt{4J^2 - (\omega \mp i\gamma/2)^2} \right) / 2, \quad (6.31)$$

when $W = 4J$, and can be broken into the real and imaginary components

$$\begin{aligned} \text{Re } \Sigma^r(\omega) &= \frac{1}{4} \left[8(\omega^2 + 4J^2)\gamma^2 + 16(\omega^2 - 4J^2)^2 + \omega^4 \right]^{\frac{1}{4}} \\ &\quad \times \sin \left[\frac{1}{2} \tan^{-1} \left(\frac{-4\omega\gamma}{-4\omega^2 + \gamma^2 + 16J^2} \right) \right] + \frac{\omega}{2} \end{aligned} \quad (6.32)$$

$$\begin{aligned} \text{Im } \Sigma^r(\omega) &= -\frac{1}{2} \left[\left(\omega^2 - \frac{\gamma^2}{4} - 4J^2 \right)^2 + \omega^2\gamma^2 \right]^{\frac{1}{4}} \\ &\quad \times \cos \left[\frac{1}{2} \tan^{-1} \left(\frac{-4\omega\gamma}{-4\omega^2 + \gamma^2 + 16J^2} \right) \right] - \frac{\gamma}{4}. \end{aligned} \quad (6.33)$$

The term in the integral of Eq. (6.30) can then be written in terms of these components, and then expanded in γ and ω . Since both γ and ω appear as the same order in the expansion and the self-energy is small outside the band edge, the error in the ω integral is small when γ is small. In practice, the bias is typically also taken to be small. For a single central site,

$$\begin{aligned} T_\gamma(\omega) &= \text{tr} [\mathbf{\Gamma}^L(\omega) \mathbf{G}^r(\omega) \mathbf{\Gamma}^R(\omega) \mathbf{G}^a(\omega)] \\ &= \frac{(2 \text{Im } \Sigma^r(\omega))^2}{(\omega - 2 \text{Re } \Sigma^r(\omega))^2 + (2 \text{Im } \Sigma^r(\omega))^2} \approx 1 - \frac{\omega^2\gamma^2}{64J^4}. \end{aligned} \quad (6.34)$$

The first term is the transmission coefficient for a 1D lattice in the Landauer formula, so the correction is of order γ^2 .

6.1.4 Large Relaxation

As γ increases, the Green's function for a single reservoir site, Eq. (6.18), approaches $g_k^r(\omega) = -2/\gamma$ in the relevant region of integration (i.e., where the difference in Fermi distributions is non-negligible). The transmission coefficient in that region, then, is

$$T_\gamma(\omega) \approx -\frac{4}{\gamma} \sum_k v_k^2 \text{Im}[\mathbf{G}^r(\omega)]. \quad (6.35)$$

Using the explicit form for the total Green's function, with \mathcal{S} consisting of a single non-interacting state with frequency ω_s , this simplifies to

$$\begin{aligned} T_\gamma(\omega) &\approx \frac{4}{\gamma} \sum_k v_k^2 \left(\frac{4 \sum_k v_k^2 / \gamma}{(\omega - \omega_s)^2 + (4 \sum_k v_k^2 / \gamma)^2} \right) = \frac{1}{\gamma} \left(\frac{1/\gamma}{(\omega - \omega_s)^2 / (4J^2)^2 + (1/\gamma)^2} \right) \\ &\approx \frac{\pi}{\gamma} \delta \left(\frac{\omega - \omega_s}{4J^2} \right) = \frac{4\pi J^2}{\gamma} \delta(\omega - \omega_s), \end{aligned} \quad (6.36)$$

where we used that $\sum_k v_k^2 = J^2$ since the couplings v_k come from a unitary transformation times the total coupling to the system. When the bias window includes this peak and at zero temperature, the current in the large γ regime becomes

$$I_3 \approx \frac{2eJ^2}{\gamma}. \quad (6.37)$$

This expression is independent of the bias, as long as it is nonzero. As we noted earlier, the transition to this value of the current, though, does depend on the bias.

6.2 Markovian Master Equation

Above, we derived a Landauer formula for the $\mathcal{L} - \mathcal{S} - \mathcal{R}$ system, which results in a Markovian master equation for the real-time dynamics in the small-to-intermediate γ regime. As we show below, outside of this regime this formalism gives physically invalid results. In the appropriate region, though, it allows the direct calculation of the full

time dynamics and can be readily expanded to include many-body interactions or time-dependent terms. Here we will derive the full solution—in all regimes—to the Markovian master equation. Given the Hamiltonian

$$H = \sum_{k \in \mathcal{L}, \mathcal{R}} \epsilon_k c_k^\dagger c_k + \sum_{k \in \mathcal{L}, \mathcal{R}} \sum_{i \in \mathcal{S}} \hbar (v_{ki} c_k^\dagger c_i + v_{ik} c_i^\dagger c_k) + H_{\mathcal{S}}, \quad (6.38)$$

the starting point is the Markovian master equation,

$$\dot{\rho} = -\frac{i}{\hbar} [H, \rho] + \sum_k \gamma_{k+} \left(c_k^\dagger \rho c_k - \frac{1}{2} \{ c_k c_k^\dagger, \rho \} \right) + \sum_k \gamma_{k-} \left(c_k \rho c_k^\dagger - \frac{1}{2} \{ c_k^\dagger c_k, \rho \} \right), \quad (6.39)$$

with $\gamma_{k+} = \gamma f_k^\alpha$ and $\gamma_{k-} = \gamma(1 - f_k^\alpha)$, where $\alpha = \mathcal{L}(\mathcal{R})$ when $k \in \mathcal{L}(\mathcal{R})$, and $f_k^{\mathcal{L}(\mathcal{R})} = 1/(\exp[\beta(\epsilon_k - V_{\mathcal{L}(\mathcal{R})})] + 1)$ is the Fermi-Dirac distribution. The total applied bias is $V = V_{\mathcal{L}} - V_{\mathcal{R}}$. This form for γ_{k+} and γ_{k-} ensures that in the absence of the interaction $H_{\mathcal{I}}$, the extended reservoirs will relax into an independent equilibrium of their own Hamiltonians, $H_{\mathcal{L}}$ and $H_{\mathcal{R}}$. For simplicity, we have assumed that γ is the same in both the left and right regions, and for all k .

This master equation describes the evolution of a system in the presence of explicit reservoir states, with a different mechanism than used previously. The following will examine the behavior of Eq. (6.39) over the full range of the relaxation γ .

6.2.1 Single Extended Reservoir State Green's Function

In the absence of \mathcal{S} , the extended reservoir states decay into the equilibrium state, $\exp(-\beta H_{\mathcal{L}(\mathcal{R})})/Z$, i.e., the occupations decay to a Fermi-Dirac distribution as $e^{-\gamma t/2}$. This can be shown from the exact time-dependent lesser Green's function in a reservoir site uncoupled from \mathcal{S} , which is given by

$$g_k^<(0, t) = i \langle c_k^\dagger(t) c_k(0) \rangle = i \text{tr} [c_k^\dagger e^{Lt} c_k \rho_{eq}], \quad (6.40)$$

where $L\rho = d\rho/dt$ can be found from Eq. (6.39) and the superoperator L is the Lindbladian. The equilibrium state of the site has filling f_k , so $\text{tr} [c_k^\dagger c_k \rho_{eq}] = f_k$. In the Fock basis of a single state, the equilibrium state is

$$\rho_{eq} = \begin{pmatrix} 1-f_k & 0 \\ 0 & f_k \end{pmatrix}. \quad (6.41)$$

A Jordan-Wigner transformation maps the electron creation and annihilation operators onto spin operators, which allows us to write $c_k \rho_{eq} = (f_k \sigma_x + i f_k \sigma_y)/2$. For the equation of motion, Eq. (6.39), the Lindblad operator is block diagonal in the the σ_x, σ_y subspace and σ_I, σ_z subspace. This means we can separately solve for the dynamics using L of those two subspaces. If we wish to calculate the action on a generic operator $O = a_0 \sigma_I + a_x \sigma_x + a_y \sigma_y + a_z \sigma_z$, for the σ_x, σ_y subspace:

$$\begin{aligned} \sigma_x \frac{da_x}{dt} + \sigma_y \frac{da_y}{dt} &= -i[\omega_k c_k^\dagger c_k, a_x \sigma_x + a_y \sigma_y] \\ &\quad + \gamma_{k+} \left(c_k^\dagger (a_x \sigma_x + a_y \sigma_y) c_k - \frac{1}{2} \{c_k^\dagger c_k, a_x \sigma_x + a_y \sigma_y\} \right) \\ &\quad + \gamma_{k-} \left(c_k (a_x \sigma_x + a_y \sigma_y) c_k^\dagger - \frac{1}{2} \{c_k c_k^\dagger, a_x \sigma_x + a_y \sigma_y\} \right). \end{aligned} \quad (6.42)$$

Acting on both sides with $(1/2)\sigma_x$ tr gives $da_x/dt = -\gamma a_x/2 + \omega_k a_y$ with $\gamma = \gamma_{k+} + \gamma_{k-}$. Similarly with $(1/2)\sigma_y$ tr, giving $da_y/dt = -\gamma a_y/2 - \omega_k a_x$. Solving these equations of motion we obtain

$$e^{Lt} c_k \rho_{eq} = \sigma_x f_k / 2e^{-t\gamma/2+\omega_k t} + \sigma_y f_k / 2e^{-t\gamma/2-\omega_k t}. \quad (6.43)$$

Then acting with c_k and taking the trace gives

$$g_k^<(0, t) = ie^{-t\gamma/2+\omega_k t} f_k, \quad (6.44)$$

for $t \geq 0$. This can be readily employed to find the retarded and advanced Green's functions for the single state

$$g_k^{r(a)}(t, t') = \mp i\Theta(\pm t \mp t')e^{-i\omega_k(t-t')-\gamma|t-t'|/2}. \quad (6.45)$$

or its Fourier transform, $g_k^{r(a)}(\omega) = (\omega - \omega_k \pm i\gamma/2)^{-1}$. Physically, the reservoir sites are exchanging electrons with a larger external reservoir with an infinite number of electrons and states without memory. The lesser Green's function is also found to be

$$g_k^<(\omega) = -f_k [g_k^r(\omega) - g_k^a(\omega)] = \frac{i\gamma f(\omega_k)}{(\omega - \omega_k)^2 + \gamma^2/4}. \quad (6.46)$$

This expression recovers the original lesser Green's function, Eq. (6.17), except that the distribution is evaluated at the ω_k of the state, rather than being a continuum over ω . As we discuss below, this has the effect of broadening the density of states after they are occupied, rather than occupying after broadening.

6.2.2 Steady-State Current

The general solution to the steady-states of the master equation (Eq. (6.39)) can also be found in an analogous way to Jauho, Meir, and Wingreen and follows the same process as the derivation for Eq. (6.30). In this case we use the equilibrium relation from the previous section, Eq. (6.46), rather than using the one that has an ω -dependent distribution $f(\omega)$. In practice, this derivation is the same but with a filling, f_k , dependent on the reservoir energy, ϵ_k .

That is, after applying the Markovian equilibrium property, Eq. (6.46), the expression for the current, Eq. (6.27), is instead

$$\begin{aligned} I = -e \sum_{i,j \in S} \sum_{\alpha,\beta \in S} \sum_{k \in L} \sum_{l \in R} \int \frac{d\omega}{2\pi} v_{ki} v_{jk} v_{\alpha l} v_{l\beta} \mathbf{G}_{i\alpha}^r(\omega) \mathbf{G}_{\beta j}^a(\omega) \\ \times [g_l^r(\omega) - g_l^a(\omega)] [g_k^r(\omega) - g_k^a(\omega)] \{f_k - f_l\}. \end{aligned} \quad (6.47)$$

Again, a concise expression for the current can be written by introducing the spectral density

$$\Gamma_{ji}^{\mathcal{L}(\mathcal{R})}(\omega) = \imath \sum_{k \in \mathcal{L}(\mathcal{R})} v_{jk} v_{ki} [g_k^r(\omega) - g_k^a(\omega)], \quad (6.48)$$

and the population-weighted spectral density

$$\tilde{\Gamma}_{ji}^{\mathcal{L}(\mathcal{R})}(\omega) = \imath \sum_{k \in \mathcal{L}(\mathcal{R})} f_k v_{jk} v_{ki} [g_k^r(\omega) - g_k^a(\omega)], \quad (6.49)$$

where the Fermi-Dirac distributions are included. Then, the current can be written as

$$I = \frac{e}{2\pi} \int_{-\infty}^{\infty} d\omega \operatorname{tr} [\tilde{\Gamma}^{\mathcal{L}}(\omega) \mathbf{G}^r(\omega) \Gamma^{\mathcal{R}}(\omega) \mathbf{G}^a(\omega) - \Gamma^{\mathcal{L}}(\omega) \mathbf{G}^r(\omega) \tilde{\Gamma}^{\mathcal{R}}(\omega) \mathbf{G}^a(\omega)], \quad (6.50)$$

Note that, in this case, the integrand in Eq. (6.50) does not include the Fermi-Dirac distribution as a separate prefactor as in the Meir-Wingreen / Landauer formula, but rather appears as a convolution with a Lorentzian due to the inclusion of a finite relaxation time from the Markovian master equation.

When the reservoir states are symmetrically coupled to the system, a simplified expression results:

$$I = -\frac{e}{2\pi} \sum_{k \in \mathcal{L}} \sum_{i,j \in \mathcal{S}} v_{ik} v_{kj} (f_k^{\mathcal{L}} - f_k^{\mathcal{R}}) \times \int_{-\infty}^{\infty} \frac{d\omega \gamma}{(\omega - \omega_k)^2 + \gamma^2/4} \operatorname{Im}[\mathbf{G}_{ij}^r(\omega)]. \quad (6.51)$$

For this symmetric case, when the two extended reservoirs have the same chemical potential, the calculated current I is always equal to zero. However, in the asymmetric case, Eq. (6.47) can yield a non-zero current even with no applied bias. We will examine this fact in Sec. 6.3 in order to develop a bound for when the Markovian master equation is consistent with physical expectations.

6.2.3 Small and Large Relaxation Limits

In similar fashion, we can derive the limiting expressions for the steady-state current in the low and high relaxation rate regimes. The spectral function for a single reservoir site connected to an implicit bath is given by

$$A_k(\omega) = i [g_k^r(\omega) - g_k^a(\omega)] = \frac{\gamma}{(\omega - \omega_k)^2 + \gamma^2/4}. \quad (6.52)$$

If γ is very small, $A_k(\omega)$ approaches $2\pi\delta(\omega - \omega_k)$. Then $A_k(\omega)f_k \approx A_k(\omega)f_{\mathcal{L}(\mathcal{R})}(\omega)$, so long as $f(\omega)$ changes little over the width of $A_k(\omega)$, and the expression for the current can be rewritten as

$$I_1 \approx \frac{e}{2\pi} \int_{-\infty}^{\infty} d\omega [f_{\mathcal{L}}(\omega) - f_{\mathcal{R}}(\omega)] \times \text{tr} [\mathbf{\Gamma}^{\mathcal{L}}(\omega)\mathbf{G}^r(\omega)\mathbf{\Gamma}^{\mathcal{R}}(\omega)\mathbf{G}^a(\omega)]. \quad (6.53)$$

This recovers Eq. (5.3) from Sec. 5.2, where the spectral density and Green's functions include the relaxation rate γ . What this means is that the master equation can be used to simulate transport, provided that γ is in a suitable range. Even the intermediate regime can be accurately simulated, so long as N_r is sufficiently large.

Similarly for large γ , the integral within Eq. (6.51) can be calculated by transforming out from the frequency domain:

$$\int_{-\infty}^{\infty} \frac{d\omega \gamma}{(\omega - \omega_k)^2 + \gamma^2/4} \mathbf{G}_{ij}^r(\omega) = 2\pi \int_{-\infty}^{\infty} dt e^{-\omega_k - \gamma|t|/2} \mathbf{G}_{ij}^r(-t) \approx -i \frac{4\pi}{\gamma} \delta_{i,j}, \quad (6.54)$$

which applies to both interacting and non-interacting Green's functions. In the non-interacting case, this can be thought of an integration over the density of states for each site in \mathcal{S} . This yields an expression for the current in the large γ regime to be

$$I_3 \approx 2e/\gamma \sum_{k \in \mathcal{L}} \sum_{i \in \mathcal{S}} v_{ki}^2 (f_k^{\mathcal{L}} - f_k^{\mathcal{R}}), \quad (6.55)$$

where again the sum is over just a single set of k (either in the left or right extended reservoir, which are identical).

When \mathcal{S} consists of a single site, then the large- γ current is found to be

$$I_3 \approx 2e/\gamma \sum_{k \in \mathcal{L}} v_k^2 (f_k^{\mathcal{L}} - f_k^{\mathcal{R}}). \quad (6.56)$$

The sum of the v_k^2 terms is the transformation that diagonalizes the extended reservoir's single particle Hamiltonian.¹ Thus,

$$\sum_{k \in \mathcal{L}(\mathcal{R})} f_k^{\mathcal{L}(\mathcal{R})} v_k^2 / J^2 \rightarrow n^{\mathcal{L}(\mathcal{R})}, \quad (6.57)$$

where $n^{\mathcal{L}(\mathcal{R})}$ is the occupation of the extended reservoir state in real space at the site immediately adjacent to the system on the left (right). This makes a correspondence with a setup with just a single extended reservoir site on each end ($N_r = 1$), $I_3 \approx 2eJ^2(n^{\mathcal{L}} - n^{\mathcal{R}})/\gamma$. Essentially, the sites further away in the $N_r > 1$ case are effectively decoupled from the system as any flow of electrons away from those sites is suppressed due to the strong relaxation. Therefore, the current in the large γ regime is also independent of N_r with the exception of discretization effects.

In contrast to the Landauer-like formalism, the Markovian master equation allows for an explicit derivation showing only the occupation at the boundaries matter, i.e., all other electrons are prevented from flowing to the system by the strong relaxation. This is possible due to the well-defined occupation of each reservoir site. In the full model, the states are broadened and then occupied, so there is no equivalent transformation to a single edge site occupation like there is in the Markovian case.

We can, however, go further with the Markovian procedure. Within a small bias window, the reservoir coupling is approximately constant $v_k^2 \approx J^2/N_r$, and the sum of the occupation terms is approximately the total number of states within the bias window

¹This can also be seen working with directly with a diagonalized linear reservoir when $v_k = J\mathcal{U}_{k1}$, where \mathcal{U} is the unitary transformation that diagonalizes the single particle Hamiltonian.

$\sum_k(f_k^L - f_k^R) \approx VN_r/(W\hbar)$. Substituting this in, we find $I_3 \approx eV[2\pi J^2/(\gamma W)](2\pi\hbar)$. Comparing with Eq. (5.10), the large γ current here is additionally inversely related to the bandwidth and grows linearly with V . Thus, while there is similar physical behavior to the full model, the large γ current is quantitatively very different for the Markovian master equation, which reflects its lack of validity in this regime.

6.3 Validity of the Markovian Master Equation

This section quantifies the regimes where the master equation is physically valid. The Markovian master equation is always mathematically valid in that it gives proper quantum evolution. However, as we will see, it does not accurately represent the equilibrium state at larger values of γ , which, e.g., leads to spurious currents and a break down of detailed balance.

6.3.1 Broadening and the Fermi Level

The Markovian master equation broadens extended reservoir states across a wide range of ω when the relaxation rate γ is large. That is, even with the Fermi level fixed in the isolated extended reservoir, there is excessive electron occupation beyond this level in the open system (succinctly, the Markovian equation occupies the states then broadens them, rather than broadening then occupying). As an example, Fig. 6.1 shows the density of states times the occupation for both the full and Markovian approaches. For small γ , Fig. 6.1(a), the relaxation is weak enough that the states are still relatively localized in energy. However, for large γ , Fig. 6.1(b), the electronic occupation is smeared too much, and this allows current to flow even without a drop in chemical potential. This difference is most apparent for states at the Fermi level, $\omega_k \approx \omega_F$, as this is where the distribution is most rapidly changing.

In the two approaches, only the lesser Green's functions are different, and these only differ by the distribution function, $f(\omega)$ compared to $f(\omega_k)$. We quantify the error, Δ ,

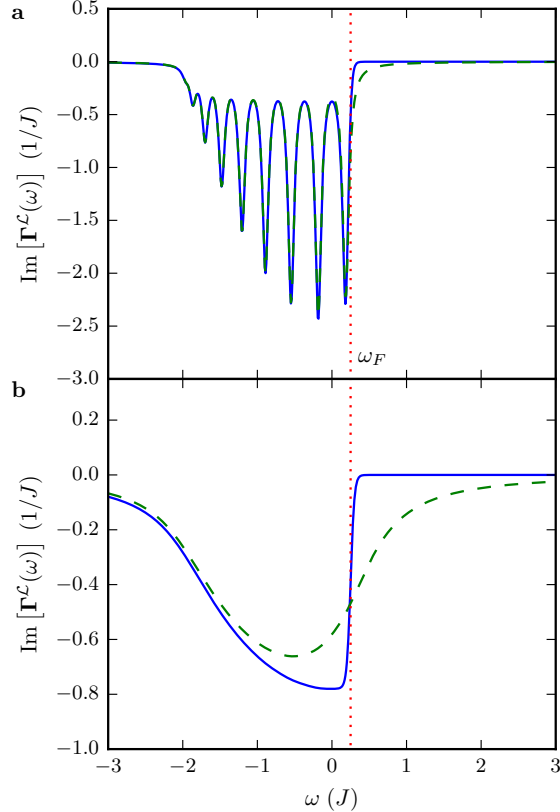


Figure 6.1: Spectral density and population-weighted spectral density for a 1D reservoir. The solid line is the spectral density, Eq. (6.48), times the Fermi-Dirac distribution and the dashed line is the population-weighted spectral density, Eq. (6.49). These correspond to the Landauer-like formula and the Markovian master equation method respectively. The number of reservoir states $N_r = 16$, bias and temperature are the same as previously, $\beta = 40(J\hbar)^{-1}$ and $\omega_F = 0.25J$, and the relaxation rate is (a) $\gamma = 0.1J$ and (b) $\gamma = J$.

between the two by the integrated absolute difference,

$$\Delta = \int_{-\infty}^{\infty} d\omega \frac{\gamma |f(\omega) - f(\omega_k)|}{(\omega - \omega_k)^2 + \gamma^2/4}. \quad (6.58)$$

To upper bound this error, we will use two features of Δ . One is that the error is maximal when the state ω_k is at the Fermi level, $\omega_k = \omega_F$. Two is that the Fermi

distribution can be replaced by the piecewise continuous function

$$f(\omega) \rightarrow \begin{cases} 1, & \omega \leq \omega_F - \frac{2}{\beta\hbar} \\ \frac{1}{2} - \frac{1}{4}\beta\hbar(\omega - \omega_F), & |\omega - \omega_F| < \frac{2}{\beta\hbar} \\ 0, & \omega \geq \omega_F + \frac{2}{\beta\hbar} \end{cases} \quad (6.59)$$

in order to obtain a bound of the error at the Fermi level. That is, this replacement has a greater absolute difference to $f(\omega_F) = 1/2$ than the original distribution function for all ω . Using these two features, the error for any ω_k is bounded by

$$\Delta \leq \arctan\left(\frac{-4}{\gamma\beta\hbar}\right) + \frac{\pi}{2} + \frac{\gamma\beta\hbar}{4} \ln\left(1 + \frac{16}{\gamma\beta\hbar}\right) \lesssim \frac{\gamma\beta\hbar}{4} \ln\left(\frac{1}{\gamma\beta\hbar}\right). \quad (6.60)$$

The condition for this error to be small is then $\gamma\beta\hbar \ll 1$. This can be interpreted as requiring that the broadening due to the relaxation must be smaller than the broadening caused by thermal processes. As well, it has a simple, intuitive mathematical meaning: The maximal slope of the Fermi-Dirac distribution should be much smaller than γ , so that the γ -induced smearing has no significant effect on the occupation.

Expanding on the above brief account, we can show that the error is maximal when ω_k is at the Fermi level by extremizing Δ ,

$$\frac{d\Delta}{d\omega_k} = \frac{d}{d\omega_k} \int_{-\infty}^{\infty} d\omega \frac{\gamma |f(\omega) - f(\omega_k)|}{(\omega - \omega_k)^2 + \gamma^2/4} = 0, \quad (6.61)$$

which can be rewritten as

$$\int_{-\infty}^{\infty} d\omega \frac{\gamma \text{sign}(\omega_k - \omega)(f'(\omega) - f'(\omega_k))}{(\omega - \omega_k)^2 + \gamma^2/4} = 0. \quad (6.62)$$

When ω_k is at the Fermi level, the term containing $f'(\omega_k)$ integrates to zero, as it is a symmetric function multiplied by an antisymmetric function around ω_k . Also when ω_k is at the Fermi level, $f'(\omega)$ is symmetric around ω_F (which comes from the relationship $f(\omega_F - \omega) = 1 - f(\omega_F + \omega)$ when $\omega_k = \omega_F$), so $f'(\omega_F - \omega) = f'(\omega_F + \omega)$. Thus, the integrand is antisymmetric and it evaluates to zero. This therefore gives an extremum

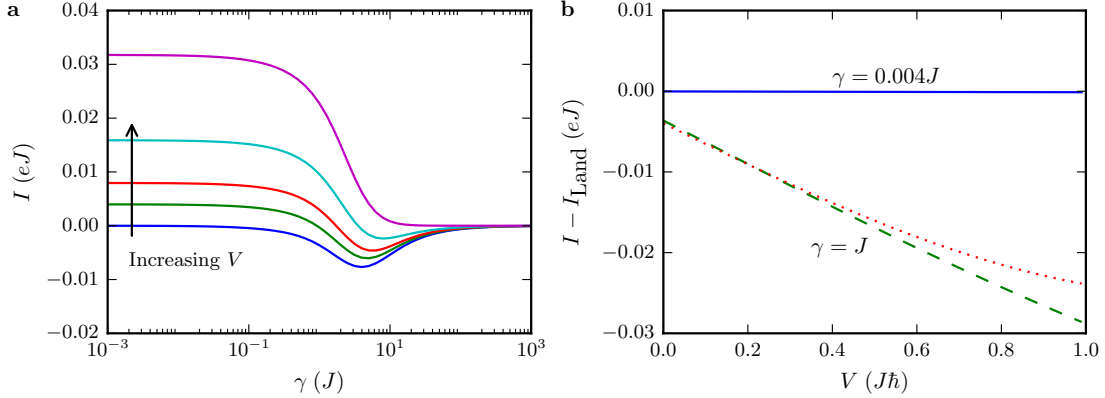


Figure 6.2: Asymmetric system response. (a) V the bias dependence of current I versus γ . The bias is $V \in \{0, 0.025, 0.05, 0.1, 0.2\}J\hbar$ from bottom to top. The reservoirs states are equally spaced with a bandwidth of $4J$, $\beta = 40(J\hbar)^{-1}$, and the left reservoir is shifted by $\delta_{\mathcal{L}} = 0.1J$ and the right is $\delta_{\mathcal{R}} = -0.1J$, making $\delta = 0.2J$. Note there is a negative current for no applied bias. (b) Difference between current I and a Landauer calculation I_{Land} versus the applied bias V for $N_r = \infty$. The solid line is near the peak current, $\gamma = 0.004J$, and the dashed line is $\gamma = J$. The dotted line is the approximation from low temperature and high bandwidth Eq. (6.64) for $\gamma = J$.

in the error. Moreover, when $\omega_k < \omega_F$, the slope is positive and when $\omega_k > \omega_F$, the slope is negative, therefore the error is maximal at the Fermi level. In the limiting cases, $\omega_k \rightarrow \pm\infty$, the total error Δ is zero, meaning that there is agreement when the state is far away from the Fermi level.

Additionally, bounds on the relaxation rate and the number of states required can be found for a given system by numerically integrating the spectral density above the Fermi level for the zero temperature case. This yields a direct measure of the improperly occupied high-energy states, even when they do not directly contribute to the electronic current.

6.3.2 Asymmetric Reservoirs

Next, we will examine a system in between asymmetric reservoirs. When the asymmetry of the \mathcal{L} and \mathcal{R} extended reservoir is due to a shift in their relative energies by δ , then

we have $\omega'_k = \omega_k + \delta/2$ for $k \in \mathcal{L}$ and $\omega'_k = \omega_k - \delta/2$ for $k \in \mathcal{R}$. Solving the equation of motion, Eq. (6.39), shows that there is a non-zero current for the zero applied bias ($V = 0$). Note that δ is a parameter that quantifies the asymmetry of the system.

Physically, the Fermi level on both reservoirs are identical, so the steady-state current between them should be zero. When the reservoir density of states is broadened by γ , the replacement of $f(\omega)$ by $f(\omega_k)$, as the Markovian model does, results in some electronic occupation above the Fermi level. This can give rise to an electronic current. Figure 6.2 shows the steady-state current I as a function of the relaxation γ for increasing values of the applied bias V .

To simplify the analytic forms for the steady-state current, we will introduce a system where the extended reservoirs are “Markovian” rather than 1D. The density of states for the 1D case is approximately constant near $\omega = 0$ as long as the bandwidth is large enough. For the following, the states in the reservoirs are equally spaced between frequencies ω_{\min} and ω_{\max} and then shifted by the asymmetry parameter δ , given $k \in \{1, \dots, N_r\}$: $\omega_k = (\omega_{\min} - \Delta/2) + \Delta k + \delta/2$ where the state spacing is $\Delta = (\omega_{\max} - \omega_{\min})/N_r$ and the couplings are constant $v_k = \sqrt{8J^2/(2\pi N_r)}$. Taking the limit as $N_r \rightarrow \infty$, the integral of the single particle Green’s functions yields for \mathcal{L}

$$\Sigma^{r(a)}(\omega) = \frac{8J^2}{2\pi W} \ln \left(\frac{\omega - \delta/2 - \omega_{\min} \mp i\gamma/2}{\omega - \delta/2 - \omega_{\max} \mp i\gamma/2} \right), \quad (6.63)$$

and similarly for \mathcal{R} . Here the bandwidth is $W = \omega_{\max} - \omega_{\min}$. The calculation of the steady-state current then continues as previously.

At zero temperature ($\beta \rightarrow \infty$), expanding the current for large bandwidth (and small V, δ), the leading terms are

$$I \approx \frac{eV(8J^2/W)}{\hbar\pi[\gamma + 2(8J^2/W)]} - \frac{8e\delta\gamma J^2}{\pi W^3}. \quad (6.64)$$

The first term gives the linear response current. For small γ , it is $eV/2\pi\hbar$. The second term gives a residual, unphysical current. So long as the asymmetry is small compared

to the bandwidth or γ is sufficiently small, this term will be negligible compared to the linear response contribution. Moreover, to accurately calculate results in the Landauer regime for steady states, γ needs to be of the order of W/N_r (this condition depends on the details of the setup, as discussed above regarding the small γ regime). Thus, so long as

$$\gamma \approx W/N_r \ll W^3 V / \delta J^2 \hbar \quad (6.65)$$

then the simulation will accurately predict steady state behavior. In other words, one needs $N_r \gg J^2 \delta \hbar / W^2 V$ (or, for our particular example earlier, $N_r \gg \delta / V$), which is a condition that is basically always fulfilled, to ensure the simulation gives accurate results in the Landauer regime. This covers both small and intermediate regimes discussed throughout the text.

6.4 Linear Reservoir with Equally Spaced States

The process of discretization of the states can have a large effect on the calculated current when using the master equation, particularly when the bias window lies completely in a gap between states. As an example, in the 1D lattice case, the extended reservoir portion of H can be directly diagonalized via a sine transformation. Thus, if one wished to study a large—but still finite—extended reservoir driving a current through a time-dependent junction, one could increase N_r by increasing the size of the reservoir in real space, a fact that also applies in higher dimensions. However, it can be more useful to instead take N_r states evenly spaced in energy and increase N_r by decreasing the spacing. That is, given $k \in \{1, \dots, N_r\}$, $\omega_k = -(W/2 + \Delta/2) + \Delta k$, where the state spacing is $\Delta = W/N_r$, places the states evenly within the energy band (note that $W = 4J$ for this model). In order for this to represent the 1D extended reservoir, the coupling constants to the system need to incorporate the local density of states for the real-space lattice at the boundary with the system. We can write the couplings with a single index, v_k for $k \in \mathcal{L}, \mathcal{R}$ (instead of v_{ki}), as the coupling to the system's boundaries only depend on k .

Using this notation, the couplings

$$v_k = 2(4J^2 - \omega_k^2)^{1/4} \sqrt{J/2\pi N_r}, \quad (6.66)$$

have a factor of $\sqrt{4J^2 - \omega_k^2}$, which is the local density of states for the 1D lattice. In the $N_r \rightarrow \infty$ limit, this choice of state discretization recovers the semi-infinite, real-space lattice.

6.5 Single-Site Reservoir Rate Equation

When the broadening γ is much smaller than the state spacing $\approx W/N_r$ and for a non-interacting system, conservation of energy requires that each electron entering the system from a site with a given energy ϵ_k also leave the system from the a site with the same energy. This allows the current to be broken into contributions from pairs of extended reservoir states, which can be calculated from a system of rate equations. We shall examine a three site system which consists of a single site from each of \mathcal{L} and \mathcal{R} (indexed by k) and a single site in \mathcal{S} . Further, we will assume different relaxation rates on the left and right, $\gamma_{\mathcal{L}}$ and $\gamma_{\mathcal{R}}$ respectively to make the appearance of a “reduced γ ” clear.

When γ is small, the effect of the environment $\mathcal{E}_{\mathcal{L}(\mathcal{R})}$ is to relax each extended state to a target filling, denoted by $f^{\mathcal{L}(\mathcal{R})}$, at a rate $\gamma_{\mathcal{L}(\mathcal{R})}$. This current due to relaxation is proportional to the difference between the onsite occupation of the reservoir state, $n^{\mathcal{L}(\mathcal{R})}$, and $f^{\mathcal{L}(\mathcal{R})}$. In linear response, the current from $\mathcal{E}_{\mathcal{L}}$ and the current into $\mathcal{E}_{\mathcal{R}}$ are

$$I_k^{\mathcal{L}} \approx e\gamma_{\mathcal{L}}(f_k^{\mathcal{L}} - n_k^{\mathcal{L}}), \quad (6.67)$$

$$I_k^{\mathcal{R}} \approx e\gamma_{\mathcal{R}}(n_k^{\mathcal{R}} - f_k^{\mathcal{R}}). \quad (6.68)$$

The current between \mathcal{S} and the reservoir states is proportional to a rate parameter σ times the difference in occupations:

$$I_k^{\mathcal{L}\mathcal{S}} \approx e\sigma(n_k^{\mathcal{L}} - n_k^{\mathcal{S}}), \quad (6.69)$$

$$I_k^{\mathcal{S}\mathcal{R}} \approx e\sigma(n_k^{\mathcal{S}} - n_k^{\mathcal{R}}). \quad (6.70)$$

The value of σ is related to the coupling between the reservoir and system and describes the particle flow rate. In the general case, this would be a function of the system-reservoir coupling and the total Green's function. For the example system, however, σ scales as $1/N_r$. In linear response, the conductance is independent of J and W , so the sum of the total current from all N_r states must be a constant.

In the steady state, all four of these currents— $I_k^{\mathcal{L}}$, $I_k^{\mathcal{R}}$, $I_k^{\mathcal{L}\mathcal{S}}$, $I_k^{\mathcal{S}\mathcal{R}}$ —must be equal, giving the solution

$$I_k = \frac{e\sigma}{\left(2 + \sigma \frac{\gamma_{\mathcal{L}} + \gamma_{\mathcal{R}}}{\gamma_{\mathcal{L}}\gamma_{\mathcal{R}}}\right)} (f_k^{\mathcal{L}} - f_k^{\mathcal{R}}). \quad (6.71)$$

The quantity $\gamma_{\mathcal{L}}\gamma_{\mathcal{R}}/(\gamma_{\mathcal{L}} + \gamma_{\mathcal{R}})$ is the “reduced γ ” between the two reservoirs and is simply $\gamma/2$ when the relaxation rates are equal. The small γ ($\gamma \ll \sigma$) approximation for Eq. (6.71) with equal relaxation rates is $I_k \approx e(\gamma/2)(f_k^{\mathcal{L}} - f_k^{\mathcal{R}})$, as used above.

This rate argument can be extended to the full $N_r \neq 1$ system by solving a system of $4N_r$ equations for each of the incoming and outgoing currents and then equating the total current into $n_{\mathcal{S}}$, $\sum_k I_k^{\mathcal{L}\mathcal{S}}$, with the total current leaving $\sum_k I_k^{\mathcal{S}\mathcal{R}}$. When $\gamma_{\mathcal{L}} = \gamma_{\mathcal{R}} = \gamma$, this yields the current through the system as

$$I \approx e\gamma/2 \sum_k (f_k^{\mathcal{L}} - f_k^{\mathcal{R}}) \frac{\sigma}{\sigma + \gamma}. \quad (6.72)$$

For small γ , this recovers the expression above. Additionally, the occupation of the central site, $n_{\mathcal{S}}$, is found to be equal to the mean target filling, $\sum_k (f_k^{\mathcal{L}} + f_k^{\mathcal{R}})/(2N_r)$. With a symmetrical distribution of reservoir state energies and bias window, then the central site onsite density is $1/2$.

Lastly, a full solution involving a different σ_k for each reservoir mode is obtainable. Assuming that the σ_k are symmetric between the left and right sides, the total current flow recovers Eq. (6.72) to the lowest order of γ . The relaxation strength limits the total current through the system and, so long as γ is sufficiently small, then the current is independent of the system-reservoir coupling.

6.6 Conclusion

Working from a realistic set of physical assumptions, namely implicit reservoirs that are kept at thermal equilibrium, we develop a set of equations that models electronic transport across all regimes. However, if one starts directly with the master equation, Eq. (2.22), then there are conditions under which it can fail in a particularly extreme way: by allowing a current to flow even if the reservoirs have the same chemical potential. The shift to an open system formalism makes some calculations more efficient, but care must be taken to ensure that the technique remains physically correct.

Chapter 7: Discord, Dephasing, and Steady States

The content in this Chapter examines the relationship between electronic correlations and steady-state transport scenarios. In particular, we explore the ballistic-to-diffusive transition in an open quantum system with an explicit dephasing term. In the model described here, this transition and the measure of quantum discord—and, in turn, the correlations—proceed continuously. The quantum discord decreases as the system becomes more diffusive, i.e., it becomes more classical. This work uses a simpler representation of an open quantum system—using Eq. (2.22)—which was later expanded into the formalism in Chapters 5 and 6.

7.1 Introduction

Solvable models of open quantum systems are important in the study of non-equilibrium systems [42]. In particular, open systems can be used to simulate transport processes at the nanoscale in cold-atom systems [159–161]. The dynamics of such systems can be found via a time evolution of the density matrix and can be extended to the steady-state regime, generally by either non-equilibrium Green’s function techniques [162] or by solving for the fixed points of the master equation that governs the density matrix. This Chapter focuses on the latter. We find the steady states of an driven fermionic lattice as it is taken from the ballistic to the diffusive regime through the use of explicit dephasing.

We show that there is a smooth decay of the quantum correlations—as quantified by discord [163]—as transport becomes more diffusive.

We consider a one-dimensional lattice with an internal Hamiltonian of

$$H = -\tilde{t} \sum_i c_i^\dagger c_{i+1} + \text{h.c.}, \quad (7.1)$$

where c_i^\dagger and c_i are fermionic creation and annihilation operators on site i respectively. The ends of this lattice are then attached to implicit reservoirs which drive the transport.

Initially, the system is set out of equilibrium by increasing the occupation on one side and decreasing it on the opposite. Then the system is allowed to time evolve until a quasi-steady-state equilibrium is reached before recurrence. In the limit of large reservoirs, this state would continue to exist indefinitely.

We consider the Markovian master equation in the Lindblad form (see Eq. (2.22))

$$\frac{d\rho}{dt} = \mathcal{L}\rho := -\imath[H, \rho] + \sum_k L_k \rho L_k^\dagger - \frac{1}{2} \left\{ L_k^\dagger L_k, \rho \right\}. \quad (7.2)$$

This forms the basis for the transporting lattice. In this state, the lattice displays zero resistivity and perfect conductivity. In order to examine the effects of an electrical impedance, this initial model is modified through a dephasing term, which is applied to every lattice site:

$$L_n = \sqrt{\kappa} c_n^\dagger c_n. \quad (7.3)$$

Since all the operators in the master equation are quadratic, the state of the system can be completely described by the elements of the correlation matrix $c_{ij} = \langle c_i^\dagger c_j \rangle$.

7.2 Discord

To calculate the quantum discord for our steady state or quasi-steady state solution, we first calculate a reduced density matrix over sections \mathcal{A} and \mathcal{B} by tracing out the rest of

the density matrix. The expression for the discord from \mathcal{A} to \mathcal{B} is given by Ref. [163]

$$\mathcal{D}(\Pi_{\mathcal{A}} : \mathcal{B}) = I(\mathcal{A} : \mathcal{B}) - J(\Pi_{\mathcal{A}} : \mathcal{B}) = H_{\mathcal{A}} - H_{\mathcal{AB}} + H(\mathcal{B}|\Pi_{\mathcal{A}}), \quad (7.4)$$

with the first term being the entropy in \mathcal{A} . We choose \mathcal{A} to be a single lattice site in the center of the lattice (with index k) and \mathcal{B} to be the site adjacent to it. This means that our entropy is then

$$H_{\mathcal{A}} = -\left\langle c_k^\dagger c_k \right\rangle \log \left\langle c_k^\dagger c_k \right\rangle - \left(1 - \left\langle c_k^\dagger c_k \right\rangle\right) \log \left(1 - \left\langle c_k^\dagger c_k \right\rangle\right), \quad (7.5)$$

with \log taken to be base 2. The next term is the entropy of the combined two systems, which is calculated by

$$H_{\mathcal{AB}} = \sum_i [-\lambda_i \log \lambda_i - (1 - \lambda_i) \log (1 - \lambda_i)], \quad (7.6)$$

where λ_i are the eigenvalues of the \mathcal{AB} correlation matrix. The last term is a conditional entropy on a measurement on k , which is calculated using the full density matrix.

7.2.1 General Measurement

The projection on a single site is a measurement of two orthogonal states:

$$|\psi_+\rangle = \cos \theta |0\rangle + e^{i\phi} \sin \theta |1\rangle \quad (7.7a)$$

$$|\psi_-\rangle = e^{-i\phi} \sin \theta |0\rangle - \cos \theta |1\rangle, \quad (7.7b)$$

with $|0\rangle$ and $|1\rangle$ corresponding to the unoccupied and occupied states on site k , respectively. The variables θ and ϕ parametrize the measurement over all possible combinations. We then write the elements of $\Pi_{\mathcal{A}}$ as

$$\pi_{\pm} = |\psi_{\pm}\rangle \langle \psi_{\pm}| \otimes \begin{pmatrix} 1 & 0 \\ 0 & 1 \end{pmatrix}. \quad (7.8)$$

That is, this operator only acts on a single site k and leaves the rest of the density matrix elements untouched. The probability of these outcomes are calculated by

$$p_{\pm} = \text{tr } \pi_{\pm} \rho = \langle \pi_{\pm} \rangle, \quad (7.9)$$

or for our particular class of states this means that the probability is equal to

$$p_+ = \cos^2 \theta \left\langle c_k^\dagger c_k \right\rangle + \sin^2 \theta \left(1 - \left\langle c_k^\dagger c_k \right\rangle \right), \quad (7.10)$$

and similarly for p_- . Once we have the probabilities, we calculate the entropy of the conditional states

$$\rho_{\mathcal{B}|\pi_{\pm}} = \text{tr}_{\mathcal{A}} \pi_{\pm} \rho_{\mathcal{AB}} / p_{\pm}. \quad (7.11)$$

The last term in Eq. (7.4) is then equal to

$$H(\mathcal{B}|\Pi_{\mathcal{A}}) = p_+ H_{\mathcal{B}|\pi_+} + p_- H_{\mathcal{B}|\pi_-}, \quad (7.12)$$

with $H_{\mathcal{B}|\pi_{\pm}} = -\text{tr} \rho_{\mathcal{B}|\pi_{\pm}} \log \rho_{\mathcal{B}|\pi_{\pm}}$. For our case, we minimize over site k using θ and ϕ as our control parameters. The full density matrix, ρ , from our reduced correlation matrix is used to calculate Eq. (7.12). We start with

$$\rho_{\mathcal{AB}} = \prod_k \left(\left\langle b_{k\sigma}^\dagger b_{k\sigma} \right\rangle b_{k\sigma}^\dagger b_{k\sigma} + \left\langle b_{k\sigma} b_{k\sigma}^\dagger \right\rangle b_{k\sigma} b_{k\sigma}^\dagger \right), \quad (7.13)$$

where $b_{k\sigma}^\dagger$ diagonalize the reduced \mathcal{AB} correlation matrix via a unitary transform U . Thus, we can replace them with

$$b_{k\sigma}^\dagger = \sum_i U_{ki}^* c_{i\sigma}^\dagger \quad \text{and} \quad b_{k\sigma} = \sum_i U_{ki} c_{i\sigma}, \quad (7.14)$$

where, lastly, $c_{i\sigma}$ is created in the full basis by means of a Jordan-Wigner transformation:

$$c_{i\sigma} = \begin{pmatrix} 1 & 0 \\ 0 & -1 \end{pmatrix}^{\otimes j-1} \otimes \begin{pmatrix} 0 & 0 \\ 1 & 0 \end{pmatrix} \otimes \begin{pmatrix} 1 & 0 \\ 0 & 1 \end{pmatrix}^{\otimes N-j}. \quad (7.15)$$

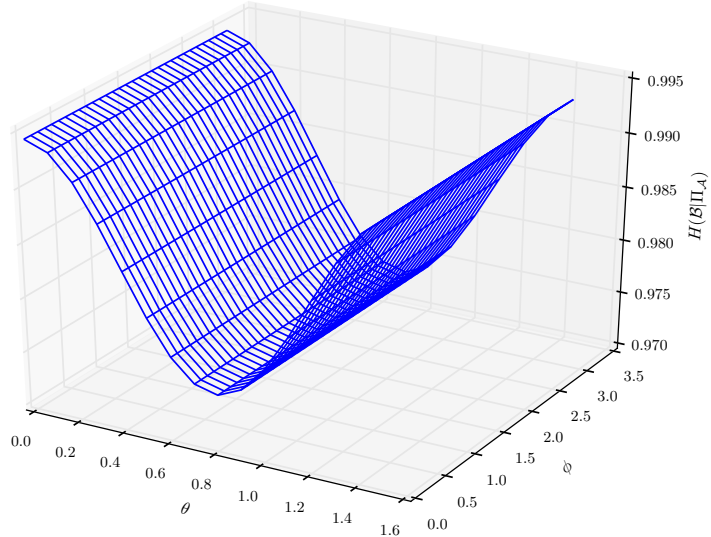


Figure 7.1: Calculation of the conditional entropy within a steady-state current. $H(\mathcal{B}|\Pi_{\mathcal{A}})$ as a function of the two angles, ϕ and θ , that specify the state. In this particular case, the lattice size $N = 8$, injection/depletion rate $\gamma = 1$ and $f = 1$ (see Sec. 7.4), dephasing $\kappa = 1$, and the measurement was performed with \mathcal{A} being site 3 and \mathcal{B} being site 4. The minimum value is independent of ψ and lies close to, but not precisely, $\theta \approx \pi/4$. Since only two sites are under examination, the minimization process is straightforward.

This gives us a 2^N by 2^N density matrix (with $N = 2$ in this case) which can then be applied to the projection operators.

For this system, the conditional entropy is largely independent of ϕ , and the minimized value lies close to $\theta \approx \pi/4$, as seen in Fig. 7.1. Some sample calculations are shown in Fig. 7.2 for an eight-site lattice with injection, depletion, and dephasing.

7.2.2 Particle Conserving Measurement

An alternative approach to the discord calculation is to perform a single-site measurement using a particle preserving projection on \mathcal{A} . This measurement is not parametrized

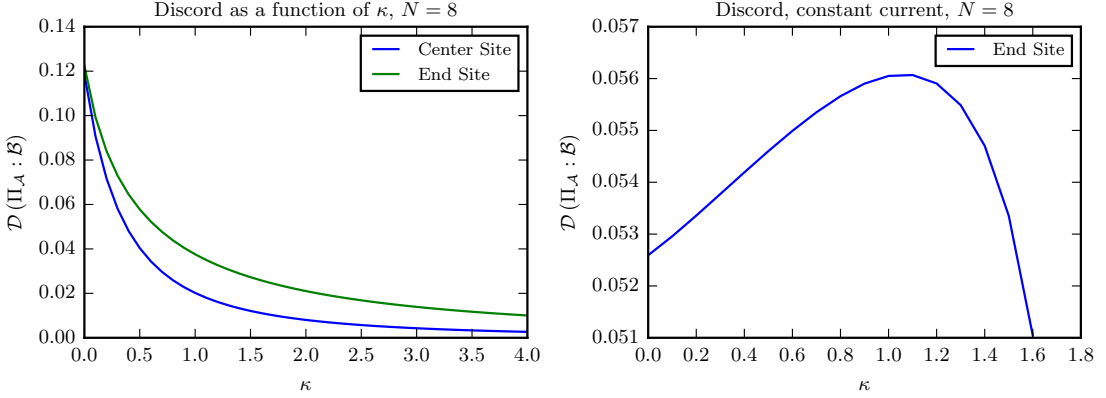


Figure 7.2: Minimum values of the quantum discord. (Left) Minimized discord as a function of the dephasing strength, κ , with constant injection/depletion rate, γ . The presence of the dephasing tends to reduce the total current and, consequently, the discord. (Right) When the current, I , is held constant by increasing γ as κ is increased, the discord initially increases.

as there is only one possible set:

$$\pi_+ = c_{k\sigma}^\dagger c_{k\sigma} \quad (7.16a)$$

$$\pi_- = c_{k\sigma} c_{k\sigma}^\dagger, \quad (7.16b)$$

and the probabilities are equal to

$$p_+ = \langle c_k^\dagger c_k \rangle = c_{k,k} \quad (7.17a)$$

$$p_- = 1 - \langle c_k^\dagger c_k \rangle = 1 - c_{k,k}. \quad (7.17b)$$

The remaining eigenvalue is

$$\lambda = \langle c_{k+1}^\dagger c_{k+1} \rangle = c_{k+1,k+1}, \quad (7.18)$$

and the remaining site is unchanged by the projection. The expression for the discord is thus

$$\begin{aligned} \mathcal{D}(\Pi_{\mathcal{A}} : \mathcal{B}) = & \sum_i \lambda_i \log \lambda_i + (1 - \lambda_i) \log(1 - \lambda_i) - c_{k,k} \log c_{k,k} - (1 - c_{k,k}) \log(1 - c_{k,k}) \\ & - c_{k+1,k+1} \log c_{k+1,k+1} - (1 - c_{k+1,k+1}) \log(1 - c_{k+1,k+1}), \end{aligned} \quad (7.19)$$

where λ_i are the eigenvalues of the two site correlation matrix:

$$\lambda_{\pm} = \frac{1}{2} \left(c_{k,k} + c_{k+1,k+1} \pm \sqrt{(c_{k,k} - c_{k+1,k+1})^2 + 4c_{k,k+1}^2} \right). \quad (7.20)$$

The expression for the discord using these eigenvalues is equal to the negative of the entropy of the original two-by-two correlation matrix plus the entropy of the same matrix with off-diagonal terms set to zero. When we perform this single site measurement, the correlation between systems \mathcal{A} and \mathcal{B} is destroyed.

7.2.3 Four Site, Particle Conserving Measurement

The discord calculation in Sec. 7.2.2 measured a single particle site, which could be in a superposition of up and down spins. Since we are more interested in the total particle movement in this system, we restrict our projective measurement to those that conserve particle number. Similar to the single site spin, we define the most general creation operator on two sites as

$$d_+^\dagger = \cos(\theta)c_i^\dagger + e^{i\phi}\sin(\theta)c_j^\dagger, \quad (7.21)$$

with its corresponding orthogonal piece as

$$d_-^\dagger = e^{-i\phi}\sin(\theta)c_i^\dagger - \cos(\theta)c_j^\dagger. \quad (7.22)$$

We then define our projectors as

$$\{\pi_k\} = \left\{ d_+^\dagger d_+ d_-^\dagger d_-, d_+ d_+^\dagger d_-^\dagger d_-, d_+^\dagger d_+ d_- d_-^\dagger, d_+ d_+^\dagger d_- d_-^\dagger \right\}, \quad (7.23)$$

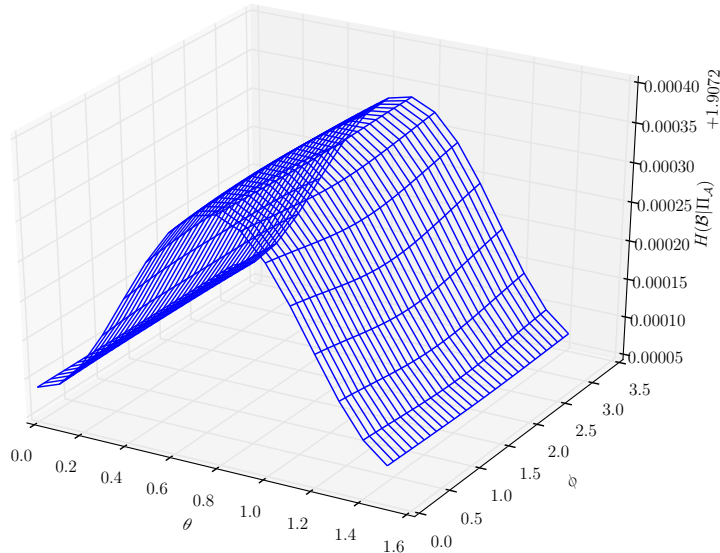


Figure 7.3: Conditional entropy of the two-site measurement. $H(\mathcal{B}|\Pi_{\mathcal{A}})$ as a function of the two angles specifying the state, ϕ and θ in Eq. (7.21) and Eq. (7.22). In this case, $N = 8$, $\Gamma = 1$, $f = 1$, $\kappa = 1$, and the measurement was performed with \mathcal{A} being sites 3 and 4 and \mathcal{B} being sites 5 and 6. Again, ϕ is irrelevant for the measurement, leading to a single θ that determines the difference.

and calculate discord the same way as in Eq. (7.4), only with four possible outcomes of the measurement rather than two. The conditional entropy on the measurement can be written entirely in terms of the correlation matrix:

$$c'_{i,j|\pi_k} = \frac{1}{p_k} \left\langle \pi_k c_i^\dagger c_j \pi_k \right\rangle, \quad (7.24)$$

where p_k is the probability of the measurement $\langle \Pi_k \rangle$. The application of a Wick decomposition to the expression in Eq. (7.24) gives a closed form for the new correlation matrix, although in practice it is easier to use the density matrix directly.

The plot of the conditional entropy for this measurement is shown in Fig. 7.3. Once again, the phase, ϕ was found to be irrelevant to the calculation of the conditional entropy, since off-diagonal elements of the correlation matrix are purely imaginary. The conditional entropy only varies by a relatively small amount over the whole range of

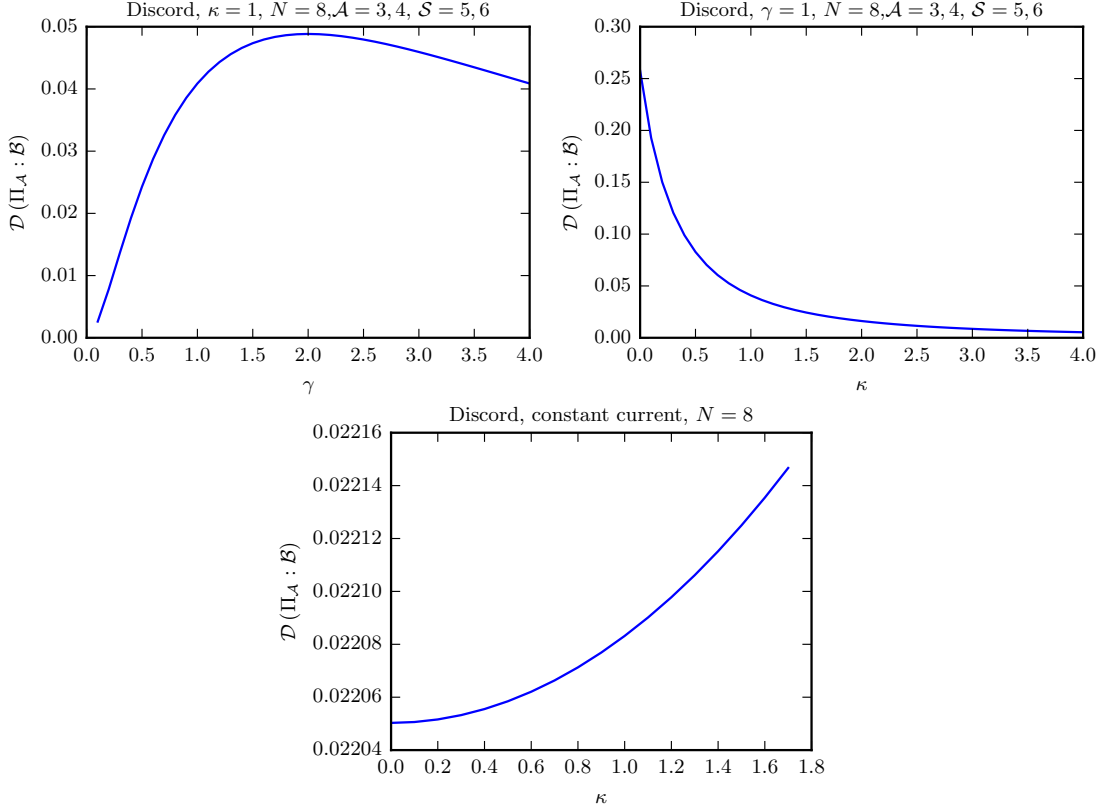


Figure 7.4: Minimized discord of the two-site particle basis measurement. In the eight-site system, the quantum discord was found as a function of (Top Left) γ , the injection term, and (Top Right) κ , the dephasing term. The bulk of the change of discord is due to the decrease or increase in current. (Bottom) When this is accounted for by increasing γ to compensate for κ and keep the current constant, the discord varies on a much smaller scale and increases.

measurements, so it is likely that the discord calculation is dominated by the entropy of the system and the system-environment terms. Figure 7.4 shows the minimized discord for the eight-site system as functions of the injection and the dephasing terms.

7.3 Analytical Results

With a known two-particle correlation matrix, the 4-by-4 density matrix is of the form

$$\rho = \begin{pmatrix} \alpha & 0 & 0 & 0 \\ 0 & \beta & \epsilon & 0 \\ 0 & \epsilon^* & \delta & 0 \\ 0 & 0 & 0 & \sigma \end{pmatrix}. \quad (7.25)$$

With a high resistivity, the current flowing though the lattice will limited, so the off-diagonal term, ϵ in Eq. (7.25), serves as an expansion parameter. Operating on this matrix for the $|+\rangle$ operator on site \mathcal{A} gives the conditional density matrix as (leaving off the normalization)

$$\rho_{\mathcal{B}|+} = \begin{pmatrix} \cos^2(\theta)\alpha + \sin^2(\theta)\delta & \epsilon \cos(\theta) \sin(\theta) \\ \epsilon \cos(\theta) \sin(\theta) & \cos^2(\theta)\beta + \sin^2(\theta)\sigma \end{pmatrix}, \quad (7.26)$$

and with $\langle -|$ gives

$$\rho_{\mathcal{B}|-} = \begin{pmatrix} \sin^2(\theta)\alpha + \cos^2(\theta)\delta & -\epsilon \sin(\theta) \cos(\theta) \\ -\epsilon \sin(\theta) \cos(\theta) & \sin^2(\theta)\beta + \cos^2(\theta)\sigma \end{pmatrix}. \quad (7.27)$$

These two density matrices yield probability of measurement for the $+$ and $-$ states equal to

$$p_+ = \cos^2(\theta)\alpha + \sin^2(\theta)\delta + \cos^2(\theta)\beta + \sin^2(\theta)\sigma, \quad (7.28a)$$

$$p_- = \sin^2(\theta)\alpha + \cos^2(\theta)\delta + \sin^2(\theta)\beta + \cos^2(\theta)\sigma. \quad (7.28b)$$

The $\rho_{B|+}$ density matrix yields eigenvalues of

$$\begin{aligned} \lambda_+ p_+ = & \frac{1}{2} (\pm \{ [\cos^2(\theta)\alpha + \sin^2(\theta)\delta]^2 - 2[\cos^2(\theta)\alpha + \sin^2(\theta)] \cdot [\cos^2(\theta)\beta + \sin^2(\theta)\sigma] \\ & + 4[\epsilon \cos(\theta) \sin(\theta)]^2 + [\cos^2(\theta)\beta + \sin^2(\theta)\sigma]^2 \}^{1/2} \\ & + \cos^2(\theta)\alpha + \sin^2(\theta)\delta + \cos^2(\theta)\beta + \sin^2(\theta)\sigma), \end{aligned} \quad (7.29a)$$

and for $\rho_{B|-}$ the eigenvalues are

$$\begin{aligned} \lambda_- p_- = & \frac{1}{2} (\pm \{ [\sin^2(\theta)\alpha + \cos^2(\theta)\delta]^2 - 2[\sin^2(\theta)\alpha + \cos^2(\theta)] \cdot [\sin^2(\theta)\beta + \cos^2(\theta)\sigma] \\ & + 4[-\epsilon \sin(\theta) \cos(\theta)]^2 + [\sin^2(\theta)\beta + \cos^2(\theta)\sigma]^2 \}^{1/2} \\ & + \sin^2(\theta)\alpha + \cos^2(\theta)\delta + \sin^2(\theta)\beta + \cos^2(\theta)\sigma). \end{aligned} \quad (7.29b)$$

Reapplication of the normalization divides the eigenvalues by the probabilities p_+ and p_- :

$$\lambda_+ = \frac{1}{2} \left\{ 1 \pm \sqrt{\frac{[\cos^2(\theta)\alpha + \sin^2(\theta)\delta - \cos^2(\theta)\beta - \sin^2(\theta)\sigma]^2 + 4[\epsilon \cos(\theta) \sin(\theta)]^2}{[\cos^2(\theta)\alpha + \sin^2(\theta)\delta + \cos^2(\theta)\beta + \sin^2(\theta)\sigma]^2}} \right\}, \quad (7.30a)$$

$$\lambda_- = \frac{1}{2} \left\{ 1 \pm \sqrt{\frac{[\sin^2(\theta)\alpha + \cos^2(\theta)\delta - \sin^2(\theta)\beta - \cos^2(\theta)\sigma]^2 + 4[\epsilon \sin(\theta) \cos(\theta)]^2}{[\sin^2(\theta)\alpha + \cos^2(\theta)\delta + \sin^2(\theta)\beta + \cos^2(\theta)\sigma]^2}} \right\}. \quad (7.30b)$$

Expanding the two previous expressions for small ϵ yields the expressions for the eigenvalues up to second order to be

$$\lambda_+ = \frac{1}{2} \left\{ 1 \pm \sqrt{\frac{[\cos^2(\theta)\alpha + \sin^2(\theta)\delta - \cos^2(\theta)\beta - \sin^2(\theta)\sigma]^2}{[\cos^2(\theta)\alpha + \sin^2(\theta)\delta + \cos^2(\theta)\beta + \sin^2(\theta)\sigma]^2}} \right\}, \quad (7.31a)$$

$$\lambda_- = \frac{1}{2} \left\{ 1 \pm \sqrt{\frac{[\sin^2(\theta)\alpha + \cos^2(\theta)\delta - \sin^2(\theta)\beta - \cos^2(\theta)\sigma]^2}{[\sin^2(\theta)\alpha + \cos^2(\theta)\delta + \sin^2(\theta)\beta + \cos^2(\theta)\sigma]^2}} \right\}. \quad (7.31b)$$

Next, we require the difference

$$H(p_+\rho_{\mathcal{B}|+} + p_-\rho_{\mathcal{B}|-}) - p_+H(\rho_{\mathcal{B}|+}) - p_-H(\rho_{\mathcal{B}|-}). \quad (7.32)$$

The first term in the expression undoes the normalization, so the combined density matrix is just Eq. (7.26) and Eq. (7.27) added together:

$$p_+\rho_{\mathcal{B}|+} + p_-\rho_{\mathcal{B}|-} = \begin{pmatrix} \alpha + \delta & 0 \\ 0 & \beta + \sigma \end{pmatrix} \quad (7.33)$$

with eigenvalues simply equal to the diagonal elements of this matrix. These two measurements of the entropy are close, with the small- ϵ expansion much simpler than the non-approximate minimization routine.

7.4 Open System Exact Solution

In the previous section, the one-dimensional lattice was modeled as an open quantum system. Using the master equation (7.2) from above, injection and depletion terms are added to the ends of the lattice by way of additional Lindblad operators:

$$\begin{aligned} L_{L+} &= \sqrt{\gamma f_L} c_1^\dagger & L_{L-} &= \sqrt{\gamma(1-f_L)} c_1 \\ L_{R+} &= \sqrt{\gamma f_R} c_N^\dagger & L_{R-} &= \sqrt{\gamma(1-f_R)} c_N, \end{aligned} \quad (7.34)$$

with γ being the coupling strength to the implicit reservoirs and f_L and f_R being the target occupation for the leftmost and rightmost sites, respectively. In the absence of a connecting lattice, the occupation of the first and last sites decay towards these values. Commonly, a parameter, f , is chosen such that $f_{L,R} = (1 \mp f)/2$ which keeps the coupled sites are symmetrically occupied.

The steady state of the system is such that

$$\frac{dc_{ij}}{dt} = \frac{d\langle c_i^\dagger c_j \rangle}{dt} = \text{Tr} \left(\frac{d\rho}{dt} c_i^\dagger c_j \right) = 0. \quad (7.35)$$

The time evolution of the correlation matrix can be expressed as a superoperator \mathbb{M} acting on c , $\mathbb{M}c = 0$. The steady state is found by solving for c using a matrix inversion on the vectorized correlation matrix and its corresponding superoperator. It is known to be a unique fixed point for symmetric injection and depletion [164]. For example, in the two site case, with $f = 0$, this reduces down to

$$\begin{pmatrix} -\gamma & i\tilde{t} & -i\tilde{t} & 0 \\ i\tilde{t} & -\gamma - \kappa & 0 & -i\tilde{t} \\ -i\tilde{t} & 0 & -\gamma - \kappa & i\tilde{t} \\ 0 & -i\tilde{t} & i\tilde{t} & -\gamma \end{pmatrix} \begin{pmatrix} \langle c_1^\dagger c_1 \rangle \\ \langle c_1^\dagger c_2 \rangle \\ \langle c_2^\dagger c_1 \rangle \\ \langle c_2^\dagger c_2 \rangle \end{pmatrix} = \begin{pmatrix} -\gamma \\ 0 \\ 0 \\ 0 \end{pmatrix}. \quad (7.36)$$

Multiplying the master equation (7.2) by $c_i^\dagger c_j$ on the right hand side and performing a trace leads to the general form for the time evolution of our correlation matrix:

$$\begin{aligned} \dot{c}_{i,j} &= i\tilde{t}(c_{i-1,j} + c_{i+1,j} - c_{i,j-1} - c_{i,j+1}) - \kappa c_{i,j}(1 - \delta_{i,j}) \\ &\quad - \frac{\gamma}{2}(1+f)(\delta_{i,1}c_{1,j}/2 + \delta_{j,1}c_{i,1}/2 - \delta_{i,1}\delta_{j,1} + \delta_{i,N}c_{N,j}/2 + \delta_{j,N}c_{i,N}/2) \\ &\quad - \frac{\gamma}{2}(1-f)(\delta_{N,i}c_{N,j}/2 + \delta_{N,j}c_{i,N}/2 - \delta_{i,N}\delta_{j,N} + \delta_{i,1}c_{1,j}/2 + \delta_{j,1}c_{i,1}/2). \end{aligned} \quad (7.37)$$

For $i = j = 1$ and assuming that the correlation matrix is tridiagonal ($c_{i,i+b} = 0$, $b > 1$), this expression becomes for the steady state:

$$-2\tilde{t} \text{Im } c_{1,2} - \gamma c_{1,1} + (\gamma/2)(1+f) = 0 \quad (7.38)$$

and for $i = j = N$:

$$-2\tilde{t} \text{Im } c_{N,N-1} - \gamma c_{N,N} + (\gamma/2)(1-f) = 0; \quad (7.39)$$

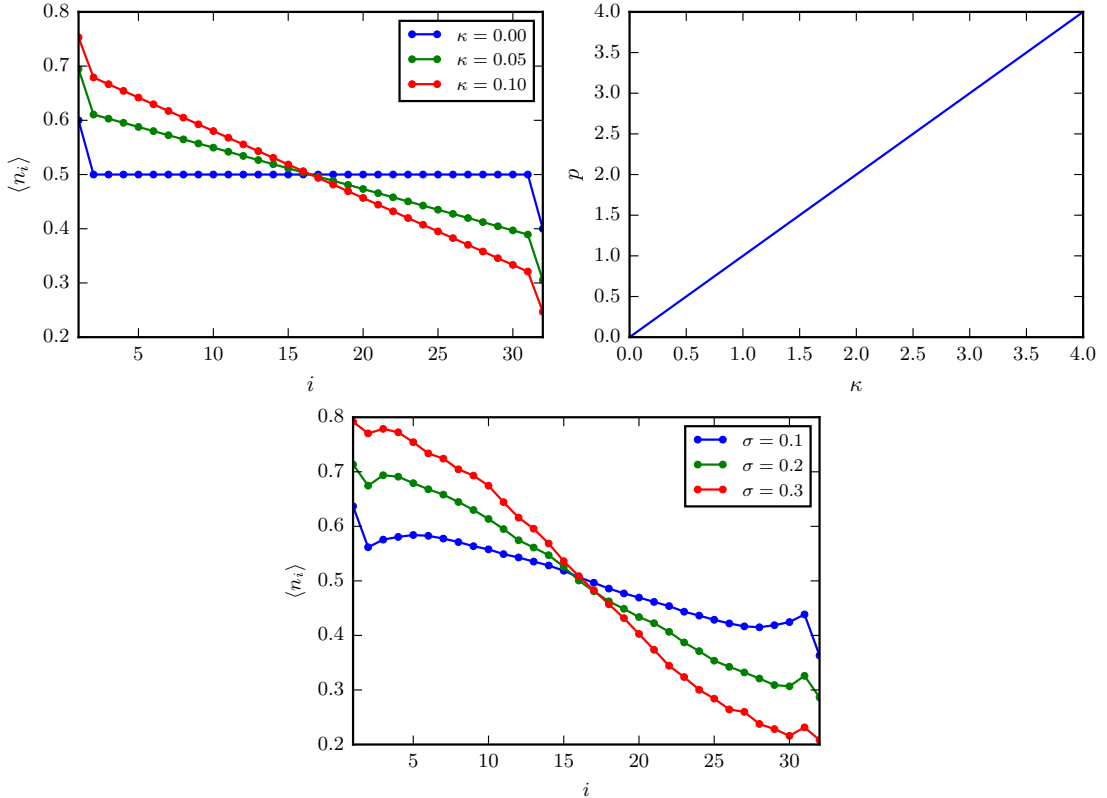


Figure 7.5: Simulation of dephasing-induced resistivity. (Top Left) Onsite densities for a lattice with length $N = 32$ with a fixed $\gamma = 1$, $f = 1$ injection and depletion terms, with increasing amounts of dephasing, κ . For $\kappa = 0$, the onsite density is constant, which corresponds to ballistic transport. As the dephasing term increases, the per-site density increases linearly between the two sides of the lattice, which indicates diffusive transport. The process occurs smoothly between the two as continuous transition. (Top Right) The resistivity as a function of κ , for constant γ and f , shows an exact correspondance between the two, as was found analytically. (Bottom) For comparison, a random onsite energy (with normal distribution standard deviation σ) is applied to each site in the lattice and the same density is calculated, with resulting values were averaged over multiple runs.

for $j = i + 1$

$$\tilde{t}c_{i+1,i+1} - \tilde{t}c_{i,i} + \kappa c_{i,i+1} = 0, \quad (7.40)$$

except for the end sites, which give the expressions

$$\tilde{t}c_{2,2} - \tilde{t}c_{1,1} + \kappa c_{1,2} - \gamma c_{1,2}/2 = 0 \quad (7.41)$$

and

$$\tilde{t}c_{N,N} - \tilde{t}c_{N-1,N-1} + \kappa c_{N-1,N} - \gamma c_{N-1,N} = 0. \quad (7.42)$$

Summing up all the pairs of expressions for Eq. (7.40) cancels all the internal pairs of onsite densities (assuming that the current is the same throughout the whole lattice):

$$-\tilde{t}c_{1,1} + \tilde{t}c_{N,N} - \kappa(N-1)c_{i,i+1} - \gamma c_{i,i+1} = 0. \quad (7.43)$$

Inserting our expressions for the end terms into this expression yields

$$-\tilde{t}\left(\frac{1+f}{2} - \frac{2\tilde{t}}{\gamma} \operatorname{Im} c_{i,i+1}\right) + \tilde{t}\left(\frac{1-f}{2} + \frac{2\tilde{t}}{\gamma} \operatorname{Im} c_{i,i+1}\right) + \iota[\kappa(N-1) + \gamma] \operatorname{Im} c_{i,i+1} = 0, \quad (7.44)$$

and solving for the nearest-neighbor correlations, and therefore the current, gives

$$\operatorname{Im} c_{i,i+1} = \frac{\gamma\tilde{t}f}{\gamma^2 + \kappa\gamma(N-1) + 4\tilde{t}^2}. \quad (7.45)$$

A local resistivity per site can be described as in Ref. [27]:

$$p = \frac{1}{Ia} \frac{\partial n_i}{\partial i}, \quad (7.46)$$

where I is the total current through the lattice and a is the lattice spacing. From

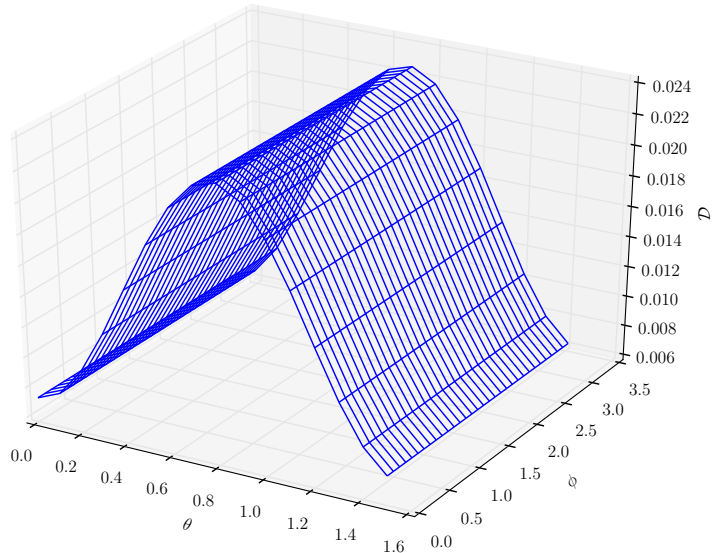


Figure 7.6: Discord of an interacting steady state. Two-site discord measurement of the interacting system steady state as a function of the measurement angles, ϕ and θ , with lattice size $N = 4$, injection/depletion of $f = 1$ and $\gamma = 1$, and density-density interaction strength of $U = 1$. Since the system only consists of a few sites the steady-state solution was found exactly. The discord is largely independent of the phase ϕ .

Eq. (7.40), this measure of the resistivity is exactly proportional to κ analytically. Figure 7.5 shows the onsite density for varying values of κ . As the dephasing increases, so does the slope and therefore the local resistivity, p . Using Eq. (7.46), the slope can be calculated numerically from the electronic density response.

7.5 Interacting System

An alternative method of providing resistivity in the system is to alter the Hamiltonian specified in (7.2) to include spin and an onsite density-density interaction instead of a dephasing term:

$$H = -\tilde{t} \sum_{i,\sigma} (c_{i\sigma}^\dagger c_{i+1\sigma} + \text{h.c.}) + U \sum_i c_{i\uparrow}^\dagger c_{i\uparrow} c_{i\downarrow}^\dagger c_{i\downarrow}. \quad (7.47)$$

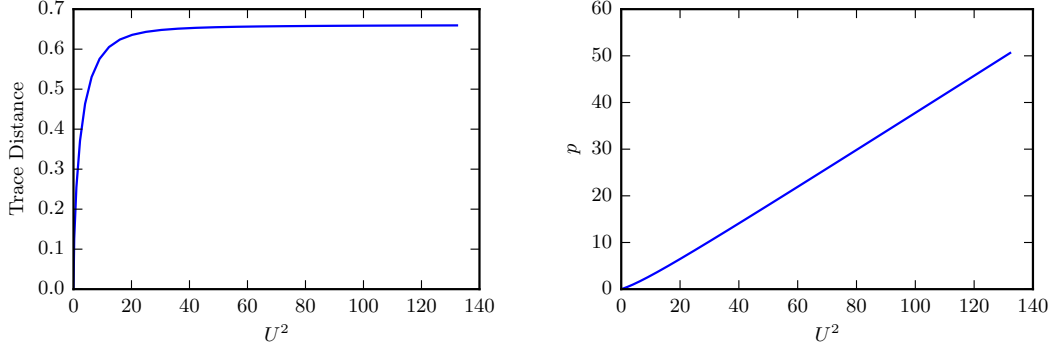


Figure 7.7: Resistivity from an interacting current. (Left) The presence of a many-body interaction term causes correlations to be developed in higher orders. The trace distance between the complete density matrix and one built from single particle correlations provides a measure of this difference. (Right) Resistivity can be directly calculated using Eq. (7.46) from the current response, as measured between the two center lattice sites. Here, $N = 4$, $f = 1$ and $\gamma = 1$, and the resistivity increases as a function of the interaction strength squared, U^2 .

The injection and depletion terms remain as previously shown in Sec. 7.4. The steady state of the full density matrix was then found via a fixed-point iteration of the Lindblad master equation, including spin.

The presence of the interaction term U generates higher order correlations that are not seen in the quadratic Hamiltonian case (Figure 7.7) but continues to restrict the flow of particles through the lattice. From numerical calculations, the measure of the resistivity through the center of the lattice is proportional to the interaction strength squared.

7.6 Conclusion

The application of onsite dephasing provides an alternative to induced disorder in creating diffusive systems. This matches intuition: as particles scatter off impurities or interact with one another, they will effectively lose correlations and become more localized, and use of the dephasing term provides an explicit decay to these states while providing a direct steady-state calculation. In cases where the scattering is strong—such as

in transport through extremely constricted regions—applying a random disorder would usually require either a time-dependent effect or many calculations with a new state in order to yield the resistivity. In addition, the quantum discord can provide a measurement of the level of correlations in electronic transport. In the model described here, this transition and the measure of quantum discord—and, in turn, the correlations—proceed continuously. This work establishes a quantitative connection between discord and resistivity and an analytical connection remains a subject for future work.

Chapter 8: Conclusion

Even though the fundamental nature of quantum physics has remained relatively unchanged since its inception in the 1920's, there is still much progress to be made in understanding time-dependent processes and mechanisms. The development of nanoscale sensing, the harnessing and control of structural fluctuations, and the advancement of next-generation materials require a treatment of electron transport beyond the level of traditional methods. In this thesis, we reported new theoretical and computational tools to help understand underlying physical processes in complex systems.

We discussed two complementary approaches of simulation of electron transport: quantum mechanically, using ultra-cold atoms as the constituent particles; and classically, performing numerical simulations on a classical computer. We developed an operational definition for the local density of states for strongly interacting particles, which can be used to study dynamical properties of a many-body system and provides a novel look at the state distribution. We also presented an in-depth examination of an interaction driven fermionic current with several levels of approximation.

In addition, we described a method of simulating a nanoscale electronic device through the use of an open quantum systems and discussed the considerations and limitations thereof. We show that an explicit treatment of the leads—in the presence of electronic

relaxation—yields a computationally efficient process for real-time simulation. Moreover, it gives a general simulation technique for finding periodic steady-states, the decay of local disturbances, and the real-time response to structural changes.

At present, there still remains a clear divide between equilibrium methods, which allow for a more rigorous and error-controlled approach, and those associated with time evolution, which often have require a greater amount of control and correctness checks. Whether or not an efficient, provably convergent method exists for all time-dependent systems continues to be an open problem. However, we have shown that a carefully constructed quantum or classical simulation can elucidate quantum physics at previously unobtainable level of detail.

Chapter 9: Bibliography

- [1] Louis De Broglie. *Recherches sur la théorie des quanta*. PhD thesis, Migration - université en cours d'affectation, 1924.
- [2] Erwin Schrödinger. Quantisierung als eigenwertproblem. *Ann. Phys.*, 385(13): 437–490, 1926.
- [3] Werner Heisenberg. Über den anschaulichen Inhalt der quantentheoretischen Kinetik und Mechanik. *Zeitschrift für Physik*, 43(3-4):172–198, 1927.
- [4] Paul AM Dirac. The quantum theory of the electron. In *Proceedings of the Royal Society of London A: Mathematical, Physical and Engineering Sciences*, volume 117, pages 610–624. The Royal Society, 1928.
- [5] John Von Neumann. Mathematische Gründlagen der Quantenmechanik. *Grundlehren der mathematischen Wissenschaften*, volume Bd, 38, 1932.
- [6] Paul AM Dirac. The quantum theory of the emission and absorption of radiation. In *Proceedings of the Royal Society of London A: Mathematical, Physical and Engineering Sciences*, volume 114, pages 243–265. The Royal Society, 1927.
- [7] Murray Gell-Mann. A schematic model of baryons and mesons. *Physics Letters*, 8(3):214–215, 1964.

- [8] Georges Zweig. An SU (3) model for strong interaction symmetry and its breaking. Version 1, 1964.
- [9] Peter W Higgs. Broken symmetries and the masses of gauge bosons. *Phys. Rev. Lett.*, 13(16):508, 1964.
- [10] Tony Freeth, Y Bitsakis, X Moussas, JH Seiradakis, A Tselikas, H Mangou, M Zafeiropoulou, R Hadland, D Bate, A Ramsey, et al. Decoding the ancient Greek astronomical calculator known as the Antikythera Mechanism. *Nature*, 444(7119):587–591, 2006.
- [11] Thomas Haigh, Mark Priestley, and Crispin Rope. Los Alamos bets on ENIAC: Nuclear Monte Carlo simulations, 1947-1948. *Annals of the History of Computing, IEEE*, 36(3):42–63, 2014.
- [12] L Piazza, TTA Lummen, Erik Quinonez, Y Murooka, BW Reed, B Barwick, and F Carbone. Simultaneous observation of the quantization and the interference pattern of a plasmonic near-field. *Nat. Commun.*, 6, 2015.
- [13] Emilia Morosan, Douglas Natelson, Andriy H Nevidomskyy, and Qimiao Si. Strongly correlated materials. *Adv. Mater.*, 24(36):4896–4923, 2012.
- [14] Robert G Parr. *Density functional theory of atoms and molecules*. Springer, 1980.
- [15] Guifré Vidal. Efficient classical simulation of slightly entangled quantum computations. *Phys. Rev. Lett.*, 91(14):147902, 2003.
- [16] Andrew John Daley, Corinna Kollath, Ulrich Schollwöck, and Guifré Vidal. Time-dependent density-matrix renormalization-group using adaptive effective Hilbert spaces. *J. Stat. Mech: Theory Exp.*, 2004(04):P04005, 2004.
- [17] Rachel Courtland. Gordon Moore: The man whose name means progress. *IEEE Spectrum*, March 2015.
- [18] Anne Meade, Jim Buckley, and John J Collins. Challenges of evolving sequential to parallel code: an exploratory review. In *Proceedings of the 12th International*

- Workshop on Principles of Software Evolution and the 7th annual ERCIM Workshop on Software Evolution*, pages 1–5. ACM, 2011.
- [19] David Kirk et al. NVIDIA CUDA software and GPU parallel computing architecture. In *ISMM*, volume 7, pages 103–104, 2007.
 - [20] Alejandro Duran and Michael Klemm. The Intel® many integrated core architecture. In *High Performance Computing and Simulation (HPCS), 2012 International Conference on*, pages 365–366. IEEE, 2012.
 - [21] Satyendra Nath Bose. Plancks gesetz und lichtquantenhypothese. *Z. phys*, 26(3):178, 1924.
 - [22] Albert Einstein. *Quantentheorie des einatomigen idealen Gases*. Akademie der Wissenschaften, in Kommission bei W. de Gruyter, 1924.
 - [23] Christopher J Pethick and Henrik Smith. *Bose-Einstein condensation in dilute gases*. Cambridge university press, 2002.
 - [24] William D Phillips and Harold Metcalf. Laser deceleration of an atomic beam. *Phys. Rev. Lett.*, 48(9):596, 1982.
 - [25] Harold J Metcalf and Peter Straten. *Laser cooling and trapping of neutral atoms*. Wiley Online Library, 2007.
 - [26] W Ketterle and NJ Van Druten. Evaporative cooling of trapped atoms. *Adv. At., Mol., Opt. Phys.*, 37, 1996.
 - [27] Jean-Philippe Brantut, Jakob Meineke, David Stadler, Sebastian Krinner, and Tilman Esslinger. Conduction of ultracold fermions through a mesoscopic channel. *Science*, 337(6098):1069–1071, 2012.
 - [28] David Stadler, Sebastian Krinner, Jakob Meineke, Jean-Philippe Brantut, and Tilman Esslinger. Observing the drop of resistance in the flow of a superfluid Fermi gas. *Nature*, 491(7426):736–739, 2012.

- [29] Jean-Philippe Brantut, Charles Grenier, Jakob Meineke, David Stadler, Sebastian Krinner, Corinna Kollath, Tilman Esslinger, and Antoine Georges. A thermoelectric heat engine with ultracold atoms. *Science*, 342(6159):713–715, 2013.
- [30] Sebastian Krinner, David Stadler, Jakob Meineke, Jean-Philippe Brantut, and Tilman Esslinger. Superfluidity with disorder in a thin film of quantum gas. *Phys. Rev. Lett.*, 110(10):100601, 2013.
- [31] Dominik Husmann, Shun Uchino, Sebastian Krinner, Martin Lebrat, Thierry Gihamarchi, Tilman Esslinger, and Jean-Philippe Brantut. Connecting strongly correlated superfluids by a quantum point contact. *Science*, 350(6267):1498–1501, 2015.
- [32] Sebastian Krinner, David Stadler, Dominik Husmann, Jean-Philippe Brantut, and Tilman Esslinger. Observation of quantized conductance in neutral matter. *Nature*, 517(7532):64–67, 2015.
- [33] Sebastian Krinner, David Stadler, Jakob Meineke, Jean-Philippe Brantut, and Tilman Esslinger. Observation of a fragmented, strongly interacting fermi gas. *Phys. Rev. Lett.*, 115(4):045302, 2015.
- [34] Wolfgang Hänsel, Peter Hommelhoff, TW Hänsch, and Jakob Reichel. Bose-Einstein condensation on a microelectronic chip. *Nature*, 413(6855):498–501, 2001.
- [35] Ron Folman, Peter Krüger, Jörg Schmiedmayer, Johannes Denschlag, and Carsten Henkel. Microscopic atom optics: From wires to an atom chip. *Adv. At. Mol. Opt. Phys.*, 48:263–356, 2002.
- [36] Immanuel Bloch, Jean Dalibard, and Wilhelm Zwerger. Many-body physics with ultracold gases. *Rev. Mod. Phys.*, 80(3):885, 2008.
- [37] Rutger A Van Santen and Matthew Neurock. *Molecular heterogeneous catalysis: a conceptual and computational approach*. John Wiley & Sons, 2009.

- [38] David K Ferry, Stephen M Goodnick, and Jonathan Bird. *Transport in nanostructures*. Cambridge University Press, 2009.
- [39] James R Heath and Mark A Ratner. Molecular electronics. 2003.
- [40] Max Born and Robert Oppenheimer. Zur quantentheorie der molekeln. *Annalen der Physik*, 389(20):457–484, 1927.
- [41] Graham A Worth and Lorenz S Cederbaum. Beyond Born-Oppenheimer: Molecular dynamics through a conical intersection. *Annu. Rev. Phys. Chem.*, 55:127–158, 2004.
- [42] Heinz-Peter Breuer and Francesco Petruccione. *The theory of open quantum systems*. Oxford university press, 2002.
- [43] Jens Kehlet Nørskov, Thomas Bligaard, Jan Rossmeisl, and Claus Hviid Christensen. Towards the computational design of solid catalysts. *Nat. Chem.*, 1(1):37–46, 2009.
- [44] Jerry L LaRue, Tetsuo Katayama, Aaron Lindenberg, Alan S Fisher, Henrik Öström, Anders Nilsson, and Hirohito Ogasawara. THz-pulse-induced selective catalytic CO oxidation on Ru. *Phys. Rev. Lett.*, 115(3):036103, 2015.
- [45] Walter Thiel. Computational catalysis—past, present, and future. *Angew. Chem. Int. Ed.*, 53(33):8605–8613, 2014.
- [46] Shigeru Ajisaka, Bojan Žunkovič, and Yonatan Dubi. The molecular photo-cell: Quantum transport and energy conversion at strong non-equilibrium. *Sci. Rep.*, 5:8312, 2015.
- [47] Vihar P Georgiev, Ewan A Towie, and Asen Asenov. Impact of precisely positioned dopants on the performance of an ultimate silicon nanowire transistor: A full three-dimensional NEGF simulation study. *Electron Devices, IEEE Transactions on*, 60(3):965–971, 2013.

- [48] Matt Krems, Michael Zwolak, Yuriy V Pershin, and Massimiliano Di Ventra. Effect of noise on DNA sequencing via transverse electronic transport. *Biophys. J.*, 97(7):1990–1996, 2009.
- [49] Tal Sharf, Neng-Ping Wang, Joshua W Kevek, Morgan A Brown, Heather Wilson, Stefan Heinze, and Ethan D Minot. Single electron charge sensitivity of liquid-gated carbon nanotube transistors. *Nano Lett.*, 14(9):4925–4930, 2014.
- [50] Chih-Chun Chien, Daniel Gruss, Massimiliano Di Ventra, and Michael Zwolak. Interaction-induced conducting–non-conducting transition of ultra-cold atoms in one-dimensional optical lattices. *New J. Phys.*, 15(6):063026, 2013.
- [51] Daniel Gruss, Kirill A. Velizhanin, and Michael Zwolak. Landauer’s formula with finite-time relaxation: Kramers’ crossover in electronic transport. *Sci. Rep.*, 6:24514, 2016.
- [52] Peter J. Mohr, David B. Newell, and Barry N. Taylor. CODATA recommended values of the fundamental physical constants: 2014. *arXiv preprint arXiv:1507.07956*, 2015.
- [53] William Arveson. *An invitation to C^* -algebras*, volume 39. Springer Science & Business Media, 2012.
- [54] Rolf Landauer. Spatial variation of currents and fields due to localized scatterers in metallic conduction. *IBM J. Res. Dev.*, 1(3):223–231, 1957.
- [55] Massimiliano Di Ventra. *Electrical transport in nanoscale systems*. Cambridge University Press Cambridge, Cambridge, UK, 2008.
- [56] Enrico Fermi. Sulla quantizzazione del gas perfetto monoatomico. *Rend. Lincei*, 3:145–149, 1926.
- [57] Paul AM Dirac. On the theory of quantum mechanics. In *Proceedings of the Royal Society of London A: Mathematical, Physical and Engineering Sciences*, volume 112, pages 661–677. The Royal Society, 1926.

- [58] Hartmut Haug and Antti-Pekka Jauho. *Quantum kinetics in transport and optics of semiconductors*. Springer, 1996.
- [59] N Bogolubov. Kinetic equations. *Zhurnal Eksperimentalnoi i Teoreticheskoi Fiziki*, 16(8):691–702, 1946.
- [60] Max Born and HS Green. A general kinetic theory of liquids. I. the molecular distribution functions. In *Proc. of the Roy. Soc. A*, volume 188, pages 10–18. The Royal Society, 1946.
- [61] John G Kirkwood. The statistical mechanical theory of transport processes i. general theory. *J. Chem. Phys.*, 14(3):180–201, 1946.
- [62] Jacques Yvon. *La théorie statistique des fluides et l'équation d'état*, volume 203. Hermann & cie, 1935.
- [63] Henrik Bruus and Karsten Flensberg. *Many-body quantum theory in condensed matter physics: an introduction*. OUP Oxford, 2004.
- [64] Jørgen Rammer and H Smith. Quantum field-theoretical methods in transport theory of metals. *Rev. Mod. Phys.*, 58(2):323, 1986.
- [65] Ulrich Schollwöck. The density-matrix renormalization group in the age of matrix product states. *Ann. Phys.*, 326(1):96–192, 2011.
- [66] Ulrich Schollwöck. Matrix product state algorithms: DMRG, TEBD and relatives. In *Strongly Correlated Systems*, pages 67–98. Springer, 2013.
- [67] Masuo Suzuki. Generalized Trotter's formula and systematic approximants of exponential operators and inner derivations with applications to many-body problems. *Commun. Math. Phys.*, 51(2):183–190, 1976.
- [68] Michael A Nielsen and Isaac L Chuang. *Quantum computation and quantum information*. Cambridge university press, 2010.

- [69] CD Fertig, KM Ohara, JH Huckans, SL Rolston, WD Phillips, and JV Porto. Strongly inhibited transport of a degenerate 1D Bose gas in a lattice. *Phys. Rev. Lett.*, 94(12):120403, 2005.
- [70] Niels Strohmaier, Yosuke Takasu, Kenneth Günter, Robert Jördens, Michael Köhl, Henning Moritz, and Tilman Esslinger. Interaction-controlled transport of an ultracold fermi gas. *Phys. Rev. Lett.*, 99(22):220601, 2007.
- [71] A Lamacraft and J Moore. Potential insights into nonequilibrium behavior from atomic physics. In K Levin, A L Fetter, and D Stamper-Kurn, editors, *Ultracold bosonic and fermionic gases*. Elsevier, Amsterdam, The Netherlands, 2012.
- [72] Chih-Chun Chien, Sebastiano Peotta, and Massimiliano Di Ventra. Quantum transport in ultracold atoms. *Nat. Phys.*, 11:998–1004, 2015.
- [73] H Ott, E De Mirandes, F Ferlaino, G Roati, G Modugno, and M Inguscio. Collisionally induced transport in periodic potentials. *Phys. Rev. Lett.*, 92(16):160601, 2004.
- [74] Kenneth Günter, Thilo Stöferle, Henning Moritz, Michael Köhl, and Tilman Esslinger. Bose-Fermi mixtures in a three-dimensional optical lattice. *Phys. Rev. Lett.*, 96(18):180402, 2006.
- [75] Paul K Hansma and Jerry Tersoff. Scanning tunneling microscopy. *J. Appl. Phys.*, 61(2):R1–R24, 1987.
- [76] C Julian Chen. *Introduction to scanning tunneling microscopy*, volume 227. Oxford University Press New York, 1993.
- [77] R Gerritsma, S Whitlock, T Fernholz, H Schlatter, J A Luigjes, J U Thiele, J B Goedkoop, and R J C Spreeuw. Lattice of microtraps for ultracold atoms based on patterned magnetic films. *Phys. Rev. A*, 76:033408, 2007.
- [78] M Singh, M Volk, A Akulshin, A Sidorov, R Mclean, and P Hannaford. One-dimensional lattice of permanent magnetic microtraps for ultracold atoms on an atom chip. *J. Phys. B: At. Mol. Opt. Phys.*, 41:065301, 2008.

- [79] J Reichel and V Vuletic, editors. *Atom Chips*. Wiley-VCH, Weinheim, Germany, 2011.
- [80] Smitha Jose, Prince Surendran, Yibo Wang, Ivan Herrera, Leszek Krzemien, Shannon Whitlock, Russell McLean, Andrei Sidorov, and Peter Hannaford. Periodic array of Bose-Einstein condensates in a magnetic lattice. *Phys. Rev. A*, 89(5):051602, 2014.
- [81] David McGloin, G Spalding, H Melville, Wilson Sibbett, and Kishan Dholakia. Applications of spatial light modulators in atom optics. *Opt. Express*, 11(2):158–166, 2003.
- [82] Matthew Pasienski and Brian DeMarco. A high-accuracy algorithm for designing arbitrary holographic atom traps. *Opt. Express*, 16(3):2176–2190, 2008.
- [83] Florence Nogrette, Henning Labuhn, Sylvain Ravets, Daniel Barredo, Lucas Béguin, Aline Vernier, Thierry Lahaye, and Antoine Browaeys. Single-atom trapping in holographic 2D arrays of microtraps with arbitrary geometries. *Phys. Rev. X*, 4(2):021034, 2014.
- [84] Cheng Chin, Rudolf Grimm, Paul Julienne, and Eite Tiesinga. Feshbach resonances in ultracold gases. *Rev. Mod. Phys.*, 82(2):1225, 2010.
- [85] Chih-Chun Chien, Michael Zwolak, and Massimiliano Di Ventra. Bosonic and fermionic transport phenomena of ultracold atoms in one-dimensional optical lattices. *Phys. Rev. A*, 85(4):041601, 2012.
- [86] Chih-Chun Chien, Massimiliano Di Ventra, and Michael Zwolak. Landauer, Kubo, and microcanonical approaches to quantum transport and noise: A comparison and implications for cold-atom dynamics. *Phys. Rev. A*, 90(2):023624, 2014.
- [87] M Zwolak and M Di Ventra. DNA spintronics. *Appl. Phys. Lett.*, 81(5):925–927, 2002.
- [88] G Rickayzen. *Green's functions and condensed matter*. Dover publications, 2013.

- [89] W Jones and N H March. *Theoretical solid state physics I: Perfect lattices in equilibrium*. Dover publications, 1985.
- [90] Guifré Vidal. Efficient simulation of one-dimensional quantum many-body systems. *Phys. Rev. Lett.*, 93(4):040502, 2004.
- [91] E. Miles Stoudenmire and Steven R. White. ITensor - Intelligent Tensor Library. <http://itensor.org/>. Accessed: 2016-04-06.
- [92] U Schneider, L Hackermuller, J P Ronzheimer, S Will, S Braun, T Best, I Bloch, E Demler, S Mandt, D Rasch, and A Rosch. Fermionic transport and out-of-equilibrium dynamics in a homogeneous Hubbard model with ultracold atoms. *Nat. Phys.*, 8:213, 2012.
- [93] Takeshi Fukuhara, Seiji Sugawa, Yosuke Takasu, and Yoshiro Takahashi. All-optical formation of quantum degenerate mixtures. *Phys. Rev. A*, 79(2):021601, 2009.
- [94] Rekishu Yamazaki, Shintaro Taie, Seiji Sugawa, and Yoshiro Takahashi. Submicron spatial modulation of an interatomic interaction in a Bose-Einstein condensate. *Phys. Rev. Lett.*, 105(5):050405, 2010.
- [95] S Blatt, TL Nicholson, BJ Bloom, JR Williams, JW Thomsen, PS Julienne, and J Ye. Measurement of optical Feshbach resonances in an ideal gas. *Phys. Rev. Lett.*, 107(7):073202, 2011.
- [96] Haibin Wu and John E Thomas. Optical control of feshbach resonances in Fermi gases using molecular dark states. *Phys. Rev. Lett.*, 108(1):010401, 2012.
- [97] Chih-Chun Chien. Spatially varying interactions induced in ultra-cold atoms by optical Feshbach resonance. *Phys. Lett. A*, 376(5):729–732, 2012.
- [98] Ulrich Schollwöck. The density-matrix renormalization group. *Rev. Mod. Phys.*, 77(1):259, 2005.

- [99] Leo Esaki and Ray Tsu. Superlattice and negative differential conductivity in semiconductors. *IBM J. Res. Dev.*, 14(1):61–65, 1970.
- [100] Esther M Conwell. Negative differential conductivity. *Phys. Today*, 23(6):35–41, 2008.
- [101] Tobias Salger, Sebastian Kling, Sergey Denisov, Alexey V Ponomarev, Peter Hänggi, and Martin Weitz. Tuning the mobility of a driven Bose-Einstein condensate via diabatic Floquet bands. *Phys. Rev. Lett.*, 110(13):135302, 2013.
- [102] Alexey V Ponomarev, Javier Madroñero, Andrey R Kolovsky, and Andreas Buchleitner. Atomic current across an optical lattice. *Phys. Rev. Lett.*, 96(5):050404, 2006.
- [103] Michael J Hartmann and Martin B Plenio. Migration of bosonic particles across a Mott insulator to a superfluid phase interface. *Phys. Rev. Lett.*, 100(7):070602, 2008.
- [104] A Polkovnikov, K Sengupta, A Silva, and M Vengalattore. Nonequilibrium dynamics of closed interacting quantum systems. *Rev. Mod. Phys.*, 83:863, 2011.
- [105] Massimiliano Di Ventra and Tchavdar N Todorov. Transport in nanoscale systems: the microcanonical versus grand-canonical picture. *J. Phys.: Condens. Matter*, 16(45):8025, 2004.
- [106] Chih-Chun Chien and Massimiliano Di Ventra. Dynamical crossover between the infinite-volume and empty-lattice limits of ultra-cold fermions in 1D optical lattices. *EPL (Europhysics Letters)*, 99(4):40003, 2012.
- [107] A Ramanathan, KC Wright, SR Muniz, M Zelan, WT Hill III, CJ Lobb, Kristian Helmerson, WD Phillips, and GK Campbell. Superflow in a toroidal Bose-Einstein condensate: an atom circuit with a tunable weak link. *Phys. Rev. Lett.*, 106(13):130401, 2011.

- [108] Kevin Henderson, Changhyun Ryu, Calum MacCormick, and MG Boshier. Experimental demonstration of painting arbitrary and dynamic potentials for Bose-Einstein condensates. *New J. Phys.*, 11(4):043030, 2009.
- [109] W Hofstetter, J I Cirac, P Zoller, E Demler, and M D Lukin. High-temperature superfluidity of fermionic atoms in optical lattices. *Phys. Rev. Lett.*, 89(22):220407, 2002.
- [110] Neil Bushong, Na Sai, and Massimiliano Di Ventra. Approach to steady-state transport in nanoscale conductors. *Nano Lett.*, 5(12):2569–2572, 2005.
- [111] Chen-Lung Hung, Xibo Zhang, Nathan Gemelke, and Cheng Chin. Slow mass transport and statistical evolution of an atomic gas across the superfluid–mott-insulator transition. *Phys. Rev. Lett.*, 104(16):160403, 2010.
- [112] Alexander Branschädel, Guenter Schneider, and Peter Schmitteckert. Conductance of inhomogeneous systems: Real-time dynamics. *Ann. Phys.*, 522(9):657–678, 2010.
- [113] David C McKay, Carolyn Meldgin, David Chen, and Brian DeMarco. Slow thermalization between a lattice and free Bose gas. *Phys. Rev. Lett.*, 111(6):063002, 2013.
- [114] F Heidrich-Meisner, SR Manmana, M Rigol, A Muramatsu, AE Feiguin, and E Dagotto. Quantum distillation: Dynamical generation of low-entropy states of strongly correlated fermions in an optical lattice. *Phys. Rev. A*, 80(4):041603, 2009.
- [115] R A Pepino, J Cooper, D Z Anderson, and M J Holland. Atomtronic circuits of diodes and transistors. *Phys. Rev. Lett.*, 103:140405, 2009.
- [116] Aaron Szafer and A Douglas Stone. Theory of quantum conduction through a constriction. *Phys. Rev. Lett.*, 62(3):300, 1989.

- [117] BJ Van Wees, H Van Houten, CWJ Beenakker, J Gr Williamson, LP Kouwenhoven, D Van der Marel, and CT Foxon. Quantized conductance of point contacts in a two-dimensional electron gas. *Phys. Rev. Lett.*, 60(9):848, 1988.
- [118] Hideaki Ohnishi, Yukihito Kondo, and Kunio Takayanagi. Quantized conductance through individual rows of suspended gold atoms. *Nature*, 395(6704):780–783, 1998.
- [119] Tsuneya Ando. Quantum point contacts in magnetic fields. *Phys. Rev. B*, 44(15):8017, 1991.
- [120] S Das Sarma, Shaffique Adam, EH Hwang, and Enrico Rossi. Electronic transport in two-dimensional graphene. *Rev. Mod. Phys.*, 83(2):407, 2011.
- [121] Sriharsha V Aradhya and Latha Venkataraman. Single-molecule junctions beyond electronic transport. *Nature Nanotech.*, 8(6):399–410, 2013.
- [122] Supriyo Datta. *Electronic transport in mesoscopic systems*. Cambridge university press, 1997.
- [123] Elke Scheer. *Molecular electronics: an introduction to theory and experiment*, volume 1. World Scientific, 2010.
- [124] Gianluca Stefanucci and C-O Almbladh. Time-dependent quantum transport: An exact formulation based on TDDFT. *Europhys. Lett.*, 67(1):14, 2004.
- [125] Chiao-Lun Cheng, Jeremy S Evans, and Troy Van Voorhis. Simulating molecular conductance using real-time density functional theory. *Phys. Rev. B*, 74(15):155112, 2006.
- [126] Jeremy S Evans, Chiao-Lun Cheng, and Troy Van Voorhis. Spin-charge separation in molecular wire conductance simulations. *Phys. Rev. B*, 78(16):165108, 2008.
- [127] Michael Zwolak and Massimiliano Di Ventra. Electronic signature of DNA nucleotides via transverse transport. *Nano Lett.*, 5(3):421–424, 2005.

- [128] Johan Lagerqvist, Michael Zwolak, and Massimiliano Di Ventra. Fast DNA sequencing via transverse electronic transport. *Nano Lett.*, 6(4):779–782, 2006.
- [129] Michael Zwolak and Massimiliano Di Ventra. Colloquium: Physical approaches to DNA sequencing and detection. *Rev. Mod. Phys.*, 80(1):141, 2008.
- [130] Daniel Branton, David W Deamer, Andre Marziali, Hagan Bayley, Steven A Benner, Thomas Butler, Massimiliano Di Ventra, Slaven Garaj, Andrew Hibbs, Xiaohua Huang, et al. The potential and challenges of nanopore sequencing. *Nat. Biotechnol.*, 26(10):1146–1153, 2008.
- [131] Shuai Chang, Shuo Huang, Jin He, Feng Liang, Peiming Zhang, Shengqing Li, Xiang Chen, Otto Sankey, and Stuart Lindsay. Electronic signatures of all four DNA nucleosides in a tunneling gap. *Nano Lett.*, 10(3):1070–1075, 2010.
- [132] Makusu Tsutsui, Masateru Taniguchi, Kazumichi Yokota, and Tomoji Kawai. Identifying single nucleotides by tunnelling current. *Nature Nanotech.*, 5(4):286–290, 2010.
- [133] Shuo Huang, Jin He, Shuai Chang, Peiming Zhang, Feng Liang, Shengqin Li, Michael Tuchband, Alexander Fuhrmann, Robert Ros, and Stuart Lindsay. Identifying single bases in a DNA oligomer with electron tunnelling. *Nature Nanotech.*, 5(12):868–873, 2010.
- [134] Takahito Ohshiro, Kazuki Matsubara, Makusu Tsutsui, Masayuki Furuhashi, Masateru Taniguchi, and Tomoji Kawai. Single-molecule electrical random resequencing of DNA and RNA. *Sci. Rep.*, 2:501, 2012.
- [135] Dale M Willard, Tina Mutschler, Ming Yu, Jaemyeong Jung, and Alan Van Orden. Directing energy flow through quantum dots: towards nanoscale sensing. *Anal. Bioanal. Chem.*, 384(3):564–571, 2006.
- [136] Yongki Choi, Issa S Moody, Patrick C Sims, Steven R Hunt, Brad L Corso, Israel Perez, Gregory A Weiss, and Philip G Collins. Single-molecule lysozyme dynamics monitored by an electronic circuit. *Science*, 335(6066):319–324, 2012.

- [137] Brett R Goldsmith, John G Coroneus, Vaikunth R Khalap, Alexander A Kane, Gregory A Weiss, and Philip G Collins. Conductance-controlled point functionalization of single-walled carbon nanotubes. *Science*, 315(5808):77–81, 2007.
- [138] Brett R Goldsmith, John G Coroneus, Alexander A Kane, Gregory A Weiss, and Philip G Collins. Monitoring single-molecule reactivity on a carbon nanotube. *Nano Lett.*, 8(1):189–194, 2008.
- [139] Sebastian Sorgenfrei, Chien-yang Chiu, Ruben L Gonzalez Jr, Young-Jun Yu, Philip Kim, Colin Nuckolls, and Kenneth L Shepard. Label-free single-molecule detection of DNA-hybridization kinetics with a carbon nanotube field-effect transistor. *Nature Nanotech.*, 6(2):126–132, 2011.
- [140] Sebastian Sorgenfrei, Chien-yang Chiu, Matthew Johnston, Colin Nuckolls, and Kenneth L Shepard. Debye screening in single-molecule carbon nanotube field-effect sensors. *Nano Lett.*, 11(9):3739–3743, 2011.
- [141] Landon Prisbrey, David Roundy, Kerstin Blank, Leonard S Fifield, and Ethan D Minot. Electrical characteristics of carbon nanotube devices prepared with single oxidative point defects. *J. Phys. Chem. C*, 116(2):1961–1965, 2012.
- [142] Tal Sharf, Joshua W Kevek, Tristan DeBorde, Jenna L Wardini, and Ethan D Minot. Origins of charge noise in carbon nanotube field-effect transistor biosensors. *Nano Lett.*, 12(12):6380–6384, 2012.
- [143] Yigal Meir and Ned S Wingreen. Landauer formula for the current through an interacting electron region. *Phys. Rev. Lett.*, 68(16):2512, 1992.
- [144] AP Jauho, NS Wingreen, and Y Meir. Time-dependent transport in interacting and noninteracting resonant-tunneling systems. *Phys. Rev. B*, 50(8):5528, 1994.
- [145] Stephanie M Reimann and Matti Manninen. Electronic structure of quantum dots. *Rev. Mod. Phys.*, 74(4):1283, 2002.

- [146] Nicolás Agrait, Alfredo Levy Yeyati, and Jan M Van Ruitenbeek. Quantum properties of atomic-sized conductors. *Phys. Rep.*, 377(2):81–279, 2003.
- [147] Pier Paolo Baruselli, Ryan Requist, Michele Fabrizio, and Erio Tosatti. Ferromagnetic Kondo effect in a triple quantum dot system. *Phys. Rev. Lett.*, 111(4):047201, 2013.
- [148] Roger Lake, Gerhard Klimeck, R Chris Bowen, and Dejan Jovanovic. Single and multiband modeling of quantum electron transport through layered semiconductor devices. *J. Appl. Phys.*, 81(12):7845–7869, 1997.
- [149] Gloria Platero and Ramón Aguado. Photon-assisted transport in semiconductor nanostructures. *Phys. Rep.*, 395(1):1–157, 2004.
- [150] So Takei, Benjamin M Fregoso, Hoi-Yin Hui, Alejandro M Lobos, and S Das Sarma. Soft superconducting gap in semiconductor Majorana nanowires. *Phys. Rev. Lett.*, 110(18):186803, 2013.
- [151] Hendrik Anthony Kramers. Brownian motion in a field of force and the diffusion model of chemical reactions. *Physica*, 7(4):284–304, 1940.
- [152] Kirill A. Velizhanin, Subin Sahu, Chih-Chun Chien, Yonatan Dubi, and Michael Zwolak. Crossover behavior of the thermal conductance and Kramers’ transition rate theory. *arXiv preprint arXiv:1312.5422*, 2013.
- [153] Kirill A. Velizhanin, Subin Sahu, Chih-Chun Chien, Yonatan Dubi, and Michael Zwolak. Crossover behavior of the thermal conductance and Kramers’ transition rate theory. *Sci. Rep.*, 5:17506, 2015.
- [154] Robert Biele, Roberto DAgosta, and Angel Rubio. Time-dependent thermal transport theory. *Phys. Rev. Lett.*, 115(5):056801, 2015.
- [155] SA Gurvitz. Rate equations for quantum transport in multidot systems. *Phys. Rev. B*, 57(11):6602, 1998.

- [156] Shigeru Ajisaka, Felipe Barra, Carlos Mejía-Monasterio, and Tomaž Prosen. Nonequilibrium particle and energy currents in quantum chains connected to mesoscopic Fermi reservoirs. *Phys. Rev. B*, 86(12):125111, 2012.
- [157] Shigeru Ajisaka and Felipe Barra. Nonequilibrium mesoscopic Fermi-reservoir distribution and particle current through a coherent quantum system. *Phys. Rev. B*, 87(19):195114, 2013.
- [158] Tamar Zelovich, Leeor Kronik, and Oded Hod. State representation approach for atomistic time-dependent transport calculations in molecular junctions. *J. Chem. Theory Comput.*, 10(8):2927–2941, 2014.
- [159] Sebastian Diehl, A Micheli, A Kantian, B Kraus, HP Büchler, and P Zoller. Quantum states and phases in driven open quantum systems with cold atoms. *Nat. Phys.*, 4(11):878–883, 2008.
- [160] Markus Greiner, Olaf Mandel, Tilman Esslinger, Theodor W Hänsch, and Immanuel Bloch. Quantum phase transition from a superfluid to a Mott insulator in a gas of ultracold atoms. *Nature*, 415(6867):39–44, 2002.
- [161] Sebastian Diehl, Andrea Tomadin, Andrea Micheli, Rosario Fazio, and Peter Zoller. Dynamical phase transitions and instabilities in open atomic many-body systems. *Phys. Rev. Lett.*, 105(1):015702, 2010.
- [162] Paweł Danielewicz. Quantum theory of nonequilibrium processes, I. *Ann. Phys.*, 152(2):239–304, 1984.
- [163] Harold Ollivier and Wojciech H Zurek. Quantum discord: a measure of the quantumness of correlations. *Phys. Rev. Lett.*, 88(1):017901, 2001.
- [164] Tomaž Prosen. Third quantization: a general method to solve master equations for quadratic open fermi systems. *New J. Phys.*, 10(4):043026, 2008.
- [165] Pierre Weiss. L’hypothèse du champ moléculaire et la propriété ferromagnétique. *J. Phys. Theor. Appl.*, 6(1):661–690, 1907.

- [166] Antoine Georges, Gabriel Kotliar, Werner Krauth, and Marcelo J Rozenberg. Dynamical mean-field theory of strongly correlated fermion systems and the limit of infinite dimensions. *Rev. Mod. Phys.*, 68(1):13, 1996.
- [167] Gaston Floquet. Sur les équations différentielles linéaires à coefficients périodiques. In *Annales scientifiques de l'École normale supérieure*, volume 12, pages 47–88, 1883.
- [168] J Liouville. Note on the theory of the variation of arbitrary constants. *Journ. de Math.*, 3:349, 1838.
- [169] Robert Brown. A brief account of microscopical observations made in the months of June, July and August 1827, on the particles contained in the pollen of plants; and on the general existence of active molecules in organic and inorganic bodies. *Phil. Mag.*, 4(21):161–173, 1828.
- [170] Albert Einstein. Über die von der molekularkinetischen Theorie der Wärme geforderte Bewegung von in ruhenden Flüssigkeiten suspendierten Teilchen. *Ann. Phys.*, 322(8):549–560, 1905.
- [171] Paul Langevin. Sur la théorie du mouvement brownien. *CR Acad. Sci. Paris*, 146 (530-533):530, 1908.
- [172] Loup Verlet. Computer “experiments” on classical fluids. I. thermodynamical properties of Lennard-Jones molecules. *Phys. Rev.*, 159(1):98, 1967.
- [173] Axel Brünger, Charles L Brooks, and Martin Karplus. Stochastic boundary conditions for molecular dynamics simulations of st2 water. *Chem. Phys. Lett.*, 105 (5):495–500, 1984.
- [174] Borivoje Dakić, Vlatko Vedral, and Časlav Brukner. Necessary and sufficient condition for nonzero quantum discord. *Phys. Rev. Lett.*, 105(19):190502, 2010.
- [175] Wojciech H Zurek. Pointer basis of quantum apparatus: Into what mixture does the wave packet collapse? *Phys. Rev. D*, 24(6):1516, 1981.

- [176] Michael Philip Zwolak. *Dynamics and simulation of open quantum systems*. PhD thesis, California Institute of Technology, 2007.
- [177] Carlos Alexandre Brasil, Felipe Fernandes Fanchini, and Reginaldo de Jesus Napolitano. A simple derivation of the Lindblad equation. *Revista Brasileira de Ensino de Física*, 35(1):01–09, 2013.

APPENDICES

Appendix A: Transformations, Distance Measures, and Examples

This Appendix contains a collection of various calculations and examples that were useful in the course of writing this thesis. More details on these and other methods can be found in most quantum mechanics/transport textbooks, such as Refs. [38, 42, 55, 68].

A.1 Jordan-Wigner Transformation

To specify the numerical form for the c_i^\dagger operators, it is natural to map them onto a spin system, of which the creation and annihilation operators correspond to the raising and lowering operators of a single spin. The presence of a particle can be represented by a spin up state, while the lack of a particle is spin down. The raising and lowering operators in Pauli matrix form are simply

$$\sigma_+ = \begin{pmatrix} 0 & 1 \\ 0 & 0 \end{pmatrix} \quad (\text{A.1a})$$

$$\sigma_- = \begin{pmatrix} 0 & 0 \\ 1 & 0 \end{pmatrix}. \quad (\text{A.1b})$$

It is tempting to use these expressions for the fermionic system, with each site being a single spin; however, care must be taken so that the anticommutation relations, Eqs. (2.6),

are fulfilled. If we index each spin operator with the site i that they act on, we find that $\{\sigma_{i-}, \sigma_{i+}\} = \sigma_I$. On different sites, however, the relationship is $[\sigma_{i-}, \sigma_{j+}] = 0$. To correct this, a sign change must be introduced when the operation is performed in the opposite order. There are many possible ways to do this, but the typical method is to make it such that the σ_+ picks up a negative sign when applied to a lower index than the σ_- operator. The adjusted expressions for the transformations are

$$c_i^\dagger = \sigma_z^{\otimes i-1} \otimes \sigma_+ \otimes \sigma_I^{\otimes N-i} \quad (\text{A.2a})$$

$$c_i = \sigma_z^{\otimes i-1} \otimes \sigma_- \otimes \sigma_I^{\otimes N-i}, \quad (\text{A.2b})$$

or, alternatively, in Pauli matrix form

$$c_i^\dagger = \begin{pmatrix} 1 & 0 \\ 0 & -1 \end{pmatrix}^{\otimes i-1} \otimes \begin{pmatrix} 0 & 1 \\ 0 & 0 \end{pmatrix} \otimes \begin{pmatrix} 1 & 0 \\ 0 & 1 \end{pmatrix}^{\otimes N-i} \quad (\text{A.3})$$

and similarly for c_i .

Since we defined the lack of particle as spin down, we can build the vacuum (or completely unoccupied) state from the product of N spin down states:

$$|\psi_0\rangle = \begin{pmatrix} 0 \\ 1 \end{pmatrix} \otimes \begin{pmatrix} 0 \\ 1 \end{pmatrix} \otimes \cdots \otimes \begin{pmatrix} 0 \\ 1 \end{pmatrix} = \begin{pmatrix} 0 \\ 1 \end{pmatrix}^{\otimes N}, \quad (\text{A.4})$$

which we can then build up any desired state by applying the creation operators to it. These operators allow for an explicit matrix form for the Hamiltonian, \mathcal{H} , as well. With this we can calculate the time evolution through a forward integrator (useful if \mathcal{H} is sparse, which it often is) or by exponentiating it to find the time evolution operator (which can be difficult to impossible).

A.2 Wick's Theorem

A common method of working with higher-order correlations is to apply Wick's Theorem. There are several different forms and derivations, but Ref. [162] provides one that is most suitable for our needs. The Wick decomposition allows us to write expectation values of operators into products of expectation values of lower order correlations:

$$\langle ABCD \rangle \rightarrow \langle AB \rangle \langle CD \rangle - \langle AC \rangle \langle BD \rangle + \langle AD \rangle \langle BC \rangle, \quad (\text{A.5})$$

where A , B , C , and D are any operators in our Hilbert space. For density matrices of the form $\rho = e^{\mathcal{A}}$, with \mathcal{A} being a single-particle operator, this decomposition is exact. Therefore, it is true for eigenstates of the system, product states, and thermal states, among others. For other states, the Wick decomposition then becomes an approximation to the true expectation value.

Rather than reproduce the general case given an arbitrary number of operators, what follows is a proof of Eq. (A.5) given the operators are fermionic creation and/or annihilation operators.¹

Without loss of generality, \mathcal{A} may be written in terms of single arbitrary operators $\mathcal{A} = \sum_i \mathcal{A}_i a_i^\dagger a_i$. Consequently, using the commutation relations, Eq. (2.6), and expanding the exponential,

$$a_i^\dagger \rho = e^{-\mathcal{A}_i} \rho a_i^\dagger \quad (\text{A.6a})$$

$$a_i \rho = e^{\mathcal{A}_i} \rho a_i. \quad (\text{A.6b})$$

Next, the expression on the left in Eq. (A.5) can be written instead as $\langle a_i^\dagger a_j a_k^\dagger a_l \rangle$ by recognizing that A through D must be written as linear combinations of the a_i operators, so it can always be expanded and later collapsed through this form. Additionally, all two-particle correlations must have the same number of creation and annihilation operators

¹Equation (A.5) is also the most commonly used form for the calculations in this thesis.

to have a non-zero value, and therefore they can use the commutation relations to put them in this order.

For a single-particle correlation, we use the density matrix commutations and the cyclic property of the trace to show that

$$\text{tr}(\rho a_i^\dagger a_j) = \delta_{ij} - \text{tr}(\rho a_j a_i^\dagger) = \delta_{ij} - e^{-\mathcal{A}_j} \text{tr}(a_j \rho a_i^\dagger) = \delta_{ij} - e^{-\mathcal{A}_j} \text{tr}(\rho a_i^\dagger a_j), \quad (\text{A.7})$$

and therefore

$$\langle a_i^\dagger a_j \rangle = \text{tr}(\rho a_i^\dagger a_j) = \frac{\delta_{ij}}{1 - e^{-\mathcal{A}_j}}. \quad (\text{A.8})$$

Similarly, for the two-particle correlation, we have

$$\begin{aligned} \text{tr}(\rho a_i^\dagger a_j a_k^\dagger a_l) &= \delta_{kl} \text{tr}(\rho a_i^\dagger a_j) + \text{tr}(\rho a_i^\dagger a_l a_j a_k^\dagger) \\ &= \delta_{kl} \text{tr}(\rho a_i^\dagger a_j) + \delta_{il} \text{tr}(\rho a_j a_k^\dagger) - \text{tr}(\rho a_l a_i^\dagger a_j a_k^\dagger) \\ &= \delta_{kl} \text{tr}(\rho a_i^\dagger a_j) + \delta_{il} \text{tr}(\rho a_j a_k^\dagger) - e^{-\mathcal{A}_l} \text{tr}(\rho a_i^\dagger a_j a_k^\dagger a_l). \end{aligned} \quad (\text{A.9})$$

Solving this expression for the larger correlation function and using Eq. (A.8), we see that

$$\begin{aligned} \text{tr}(\rho a_i^\dagger a_j a_k^\dagger a_l) &= \frac{\delta_{kl}}{1 - e^{-\mathcal{A}_l}} \text{tr}(\rho a_i^\dagger a_j) + \frac{\delta_{il}}{1 - e^{-\mathcal{A}_l}} \text{tr}(\rho a_j a_k^\dagger) \\ &= \text{tr}(\rho a_k^\dagger a_l) \text{tr}(\rho a_i^\dagger a_j) + \text{tr}(\rho a_i^\dagger a_l) \text{tr}(\rho a_j a_k^\dagger) \end{aligned}$$

or

$$\langle a_i^\dagger a_j a_k^\dagger a_l \rangle = \langle a_i^\dagger a_j \rangle \langle a_k^\dagger a_l \rangle + \langle a_i^\dagger a_l \rangle \langle a_j a_k^\dagger \rangle. \quad (\text{A.10})$$

This argument is easily expanded into the general case, as in Eq. (A.5), and to include even higher order correlation functions.

While the derivation makes an assumption about the form of the density matrix, this decomposition becomes an approximation when the state is “close” to that form. As

an example, if a two-particle operator is acting on a state, such as $c_{i\uparrow}^\dagger c_{j\uparrow} c_{i\downarrow}^\dagger c_{j\downarrow}$, then this allows us to cast it into mean field form as $c_{i\uparrow}^\dagger c_{j\uparrow} \langle c_{i\downarrow}^\dagger c_{j\downarrow} \rangle$. That is, we use the expectation value rather than the true correlation function. Smaller fluctuations on individual particles do not matter as much as the aggregate average. This type of many-body to single-particle approximation first appeared to study phase transitions [165] and is deeply studied with respect to fermionic systems [166].

A.3 Quantum Discord

In Sec. 2.4, we discussed the entanglement entropy and how it can measure the amount of correlations between two parts of the system. However, correlations can develop in fully classical systems as well. This did not matter before because we just wanted to minimize the Hilbert space, but it occasionally becomes necessary to separate the quantum correlations from the classical ones. The measure of this is known as the quantum discord [163].

The main idea behind quantum discord is that there are two ways of representing the mutual information:

$$I(A; B) \equiv H(A) + H(B) - H(A, B) \quad (\text{A.11a})$$

$$J(A; B) \equiv H(A) - H(A|B). \quad (\text{A.11b})$$

The expression $H(A)$ is the information entropy, $H(A, B)$ is the joint entropy, and $H(A|B)$ is the conditional entropy. An application of the Bayes rule shows that these two expressions are identical for a classical system. However, if we wish to apply this to a quantum system via the usual use of the von Neumann entropy, we find that these expressions become

$$I(\mathcal{A} : \mathcal{B}) = H_{\mathcal{A}} + H_{\mathcal{B}} - H_{\mathcal{AB}} \quad (\text{A.12a})$$

$$J(\Pi_{\mathcal{A}} : \mathcal{B}) = H_{\mathcal{B}} - H(\mathcal{B}|\Pi_{\mathcal{A}}). \quad (\text{A.12b})$$

For the first expression, the entropy is replaced by its quantum version over the whole system or subsystem. That is $H_{\mathcal{A}\mathcal{B}} = H(\rho)$ and $H_{\mathcal{A}} = H(\text{tr}_B\rho)$ if \mathcal{A} and \mathcal{B} constitute the entire system. In the quantum case, in order to make the same conditional statement about “ \mathcal{B} given \mathcal{A} ,” we must define a measurement on the state of \mathcal{A} , which is $\Pi_{\mathcal{A}}$. The discord is the difference between these two expressions for mutual information:

$$\mathcal{D}(\Pi_{\mathcal{A}} : \mathcal{B}) \equiv I(\mathcal{A} : \mathcal{B}) - J(\Pi_{\mathcal{A}} : \mathcal{B}) = H_{\mathcal{A}} - H_{\mathcal{A}\mathcal{B}} + H(\mathcal{B}|\Pi_{\mathcal{A}}). \quad (\text{A.13})$$

In the true measure of quantum discord, $\Pi_{\mathcal{A}}$ is taken to be the measurement that maximizes the discord over all possible states. As this requires variation over many parameters for even small systems, the computation is exponential in the dimension of the Hilbert space and so other measures have been proposed that are simpler to calculate, such as geometric quantum discord [174] where the discord can be quantified in a more computable manner. However, it is not a faithful measure in general.

A nonzero calculation of the discord indicates the presence of correlations that exist due to quantum operators, which could otherwise not be found in classical systems. More importantly, it is possible to find states where the discord is nonzero but the entanglement entropy is zero, which means that is possible for a separable state to still exhibit quantum effects, which means that the lack of entanglement alone is not sufficient to define a classical state. A state with zero discord is known as a pointer state [175], and is the preferred notion of classicality within a quantum system.

A.4 Distance Measurement

Often it becomes necessary to quantify how close two quantum states are to one another, for example, when examining an approximate solution to a known analytic case. Given two quantum states, ρ and σ , we define the trace distance between them as [68]

$$D(\rho, \sigma) \equiv \frac{1}{2}\text{tr}|\rho - \sigma|, \quad (\text{A.14})$$

where we define the norm of an operator to be $|A| \equiv \sqrt{A^\dagger A}$, with a positive square root. Obviously if ρ and σ are the same state then the trace distance is zero, and D will always be positive. An intuitive way to consider the trace distance is to consider a pair of spin states, which can be represented on what is known as a Bloch sphere. If the states are

$$\rho = \frac{I + \vec{r} \cdot \vec{\sigma}}{2} \quad \text{and} \quad \sigma = \frac{I + \vec{s} \cdot \vec{\sigma}}{2}, \quad (\text{A.15})$$

where $\vec{\sigma}$ is the vector of Pauli matrices, then

$$D(\rho, \sigma) = \frac{|\vec{r} - \vec{s}|}{2}. \quad (\text{A.16})$$

In other words, the trace distance is half the Euclidean distance between them on the Bloch sphere. There are several useful properties of the trace distance such as preservation over unitary transformations,

$$D(U\rho U^\dagger, U\sigma U^\dagger) = D(\rho, \sigma), \quad (\text{A.17})$$

triangle inequality,

$$D(\rho, \tau) \leq D(\rho, \sigma) + D(\sigma, \tau), \quad (\text{A.18})$$

and that quantum operations are contractive,

$$D(\mathcal{E}(\rho), \mathcal{E}(\sigma)) \leq D(\rho, \sigma). \quad (\text{A.19})$$

A.5 Switching Between Levels of Approximation

Most of the mathematical details described above and in the main text can apply from exact calculations to mean-field approximations. This section contains examples of how one can move “up” or “down” in the level of detail, while still describing the same system.

A.5.1 Operator to Superoperator Conversions

Often it is useful to move from a left-right matrix multiply, such as that in Eq. (2.22), to only a left matrix multiply or even a fully linearized left matrix multiply. If the equation of motion is put into this form, then the usual techniques with working with linear differential equations apply. For instance, if the differential equation is in the form

$$\dot{x} = \mathbf{M}x, \quad (\text{A.20})$$

with x a vector and \mathbf{M} a matrix, then the exact solution can be found simply by exponentiating \mathbf{M} , if the number of variables is small enough.

In general, we can define a rank-4 superoperator, Ω , acting on a 2D matrix² c as

$$(\Omega \cdot c)_{ij} = \sum_{kl} \Omega_{ijkl} c_{kl}. \quad (\text{A.21})$$

For a closed non-interacting system, the time evolution of c can be defined in this way because \dot{c} is a linear function of all of the other terms in the matrix. Additionally, Eq. (A.21) can be written in matrix-vector form by grouping the two sets of indicies into a single one each with no loss of generality.

Most operations appear as a matrix-matrix product on either side of the correlation matrix, and these can easily be converted into left superoperators on the vectorized c_{vec} by

$$H_L \cdot c \Rightarrow (I_N \otimes H_L) \cdot c_{\text{vec}} \quad (\text{A.22a})$$

$$c \cdot H_R \Rightarrow (H_R^\dagger \otimes I_N) \cdot c_{\text{vec}} \quad (\text{A.22b})$$

$$H_L \cdot c \cdot H_R \Rightarrow (H_R^\dagger \otimes H_L) \cdot c_{\text{vec}}, \quad (\text{A.22c})$$

²The focus is on correlation matrices in this section, but these results are generally true for any set of matrices.

where I_N is the identity matrix of size N , the number of sites. Notice that the superoperator is now an N^4 by N^4 size matrix. The same approach to vectorizing also applies to operations on the full density matrix, ρ , in order to reduce the time evolution of the system to a set of linear operators.

For the open system case, the equation of motion has an additional term of the form

$$\dot{c}_{ij} = \sum_{kl} \Omega_{ijkl} c_{kl} + F_{ij}, \quad (\text{A.23})$$

which is a constant term which does not depend on any of the terms of c . In the steady state solution, $\dot{c}_{ij} = 0$, the term, F , becomes the right hand side of the expression and Ω is inverted to solve for c_{ij} . However, the full dynamics or properties of the time evolution are often required, so it is useful to include F into the linearization of the differential equation.

The solution to this is to expand c_{vec} to include an additional term which is always 1. Therefore, the equation of motion can be rewritten as

$$\begin{pmatrix} \dot{c}_{\text{vec}} \\ 1 \end{pmatrix} = \begin{pmatrix} \Omega & F \\ 0 & 0 \end{pmatrix} \cdot \begin{pmatrix} c_{\text{vec}} \\ 1 \end{pmatrix}, \quad (\text{A.24})$$

and the equation is fully linear and the usual analysis can be applied to it (F and Ω in this expression are their vectorized forms so that the operator is a 2D matrix). Moreover, since the last term is always equal to 1, this provides a convenient way to normalize solutions that would otherwise require another constraint—for example, finding the eigenvectors of the linear operator to locate the states that do not decay.

A.5.2 Correlation Matrix to Density Matrix Conversion

Often it is useful to convert from the reduced representation correlation matrix back into the full density matrix form. For example, different measures of the entanglement entropy or discord require this form. Since the correlation matrix is a collection of

expectation values, then we can easily write the density matrix as [176]

$$\rho = \prod_k \left\langle b_k^\dagger b_k \right\rangle b_k^\dagger b_k + \left\langle b_k b_k^\dagger \right\rangle b_k b_k^\dagger, \quad (\text{A.25})$$

where b_k is associated with the diagonal basis of the block of lattice sites, and can be written in terms of c_i , the site basis. This site basis is expressed using the Jordan-Wigner transformation as described in Sec. A.1. The reverse process is simpler: calculate the needed expectation values using the density matrix,

$$c_{ij}(t) = \text{tr} \left[\rho(t) c_i^\dagger c_j \right]. \quad (\text{A.26})$$

However, information about the density matrix will be lost using this conversion in the general case. Combining this method with the similarity measurement in Sec. A.4 yields a useful matrix for how correlated the state of the system is and how closely it can be represented using the mean field methods.

A.6 Examples

This section contains a few examples of the types of derivations used within the main text. For the most part, any arbitrary system is treated the same way: a Hamiltonian or energy distribution is defined first, which leads to the creation of the expressions for the reservoirs or Green's functions. In numerical cases, these expressions can often be evaluated directly from the initial expressions.

A.6.1 Born-Markov Approximation

If we have an explicit definition of the system Hamiltonian, we can derive the Lindblad terms in Eq. (2.22) by assuming a site is connected to two implicit reservoirs, one full and one empty, each with a Hamiltonian given by $H_B = \sum_k \omega_k a_k^\dagger a_k$, and a connection to the implicit reservoir as an operator $B^\dagger = \sum_k g_k a_k^\dagger$ and R so that the coupling between

the two is $H_{BR} = R^\dagger B + B^\dagger R$. In this example, R is a single site operator c_i with onsite energy ϵ_i so that $R(t) = Re^{-\imath\epsilon_i t}$ in the interaction picture with $i \in L, R$. Following [177], to create the Lindblad operators, we must find the time dependent partial trace of the B terms:

$$F(t) = \int_0^t dt' \operatorname{tr}_B \left[B(t) B^\dagger(t') \rho_B e^{\imath\epsilon_i(t-t')} \right] \quad (\text{A.27})$$

and

$$G(t) = \int_0^t dt' \operatorname{tr}_B \left[B^\dagger(t') B(t) \rho_B e^{\imath\epsilon_i(t-t')} \right]. \quad (\text{A.28})$$

We assume that the bath is in thermal equilibrium with no correlations between the modes $\langle a_k^\dagger a_{k'} \rangle = \delta_{k,k'}$ for the full reservoir and $\langle a_k^\dagger a_{k'} \rangle = 0$ for the empty. In the interaction picture this means that we can express the expectation values as

$$F(t) = \int_{-\infty}^{\infty} d\omega J_f(\omega) \int_0^t dt' e^{-\imath(\omega - \epsilon_i)(t-t')} \quad (\text{A.29})$$

and

$$G(t) = \int_{-\infty}^{\infty} d\omega J_e(\omega) \int_0^t dt' e^{-\imath(\omega - \epsilon_i)(t-t')}, \quad (\text{A.30})$$

with J_f and J_e being the spectral functions of the full and empty implicit reservoirs respectively. In the discrete case, it is described with

$$J(\omega) = \sum_k |g_k|^2 \delta(\omega - \omega_k) \quad (\text{A.31})$$

before being taken into the continuum limit. Still working in the interaction picture, the time evolution of the reservoir density matrix ρ_R can be expressed in terms of the F and G functions via

$$\begin{aligned} \frac{d}{dt} \rho_R(t) &= -G^*(t) \left[RR^\dagger \rho_R(t) - R^\dagger \rho_R(t) R \right] - F^*(t) \left[\rho_R(t) R^\dagger R - R \rho_R(t) R^\dagger \right] \\ &\quad - F(t) \left[R^\dagger R \rho_R(t) - R \rho_R(t) R^\dagger \right] - G(t) \left[\rho_S(t) RR^\dagger - R^\dagger \rho_R(t) R \right], \end{aligned} \quad (\text{A.32})$$

In the Markov approximation, the limit in the integral for F and G is taken to be $t \rightarrow \infty$, meaning that the oscillating term goes to

$$\int_0^\infty d\tau e^{-i(\omega - \epsilon_i)\tau} = \pi\delta(\omega - \epsilon_i) - iP\frac{1}{\omega - \epsilon_i}, \quad (\text{A.33})$$

with the P implying a principal value integral in the expression for F and G :

$$F(t) = \pi J_f(\epsilon_i) - iP \int_{-\infty}^{\infty} d\omega \frac{J_f(\omega)}{\omega - \epsilon_i} \quad (\text{A.34})$$

and similarly for $G(t)$, which are then substituted into Eq. (A.32). In this manner, we can derive the open version of a system coupled to a particular reservoir configuration simply by reevaluating the expression involving the spectral functions. In addition, it is possible to work in a reverse fashion by starting with a desired open reservoir distribution and finding a discretization of the modes yields the desired time evolution, or, if one is not possible, find one that matches in the correct regime.

A.6.2 Non-interacting Green's Functions

As a quick check on the non-equilibrium theory that we have established in Sec. 2.3.3, we want to ensure we recover the same dynamics as in the Landauer formalism. For this we will use a Hamiltonian of the form

$$H = \sum_{\alpha; k \in L, R} \epsilon_{k\alpha} c_{k\alpha}^\dagger c_{k\alpha} + \sum_{\alpha} \epsilon_{\alpha} c_{\alpha}^\dagger c_{\alpha} + \sum_{\alpha; k \in L, R} (V_{k\alpha} c_{k\alpha}^\dagger c_{\alpha} + \text{H.c.}), \quad (\text{A.35})$$

where we have a band of energies on either side connected to a central non-interacting site. We can define a level-width function for the two leads as

$$\Gamma_{L(R)\alpha}(\omega) = 2\pi \sum_{k \in L(R)} |V_{k\alpha}|^2 \delta(\omega - \epsilon_{k\alpha}). \quad (\text{A.36})$$

If we calculate the current using the change in occupation of the left side lead and the equations of motion for the Green's functions, we find the following simple expression

(details of the derivation as found in Ref. [58]):

$$I = \frac{e}{\hbar} \int \frac{d\epsilon}{2\pi} T(\epsilon) [f_L(\epsilon) - f_R(\epsilon)]. \quad (\text{A.37})$$

f_L and f_R are the occupation functions of the left side and right side leads where $T(\epsilon)$ is a transmission probability at a given energy. This expression for the current is the exact same one as we have found in the Landauer formalism; however, we have not built any assumptions into our model beyond describing the Hamiltonian. Furthermore, the transmission coefficient is given by

$$T(\epsilon) = \text{Tr} \{ \Gamma_L(\epsilon) G^r(\epsilon) \Gamma_R(\epsilon) G^a(\epsilon) \}. \quad (\text{A.38})$$

In the case of simple bands, the level-width function just becomes a constant over a specified range and bounds the limits of integration in the expression for the current.

Appendix B: Computational and Practical Considerations

This appendix serves to provide implementation-specific details about how the numerical results in this thesis were calculated and is a reference for specific programming languages and software that I've used over the course of my PhD. In general, I've prioritized open-source and portable solutions over those provided by proprietary software.

B.1 Scientific Computing and Python

Python is an open-source, high-level, interpreted programming language, and was used for nearly all the calculations presented in this thesis. Except on rare occasions, the “hot spots” in the code path—the parts that used the heaviest numerical processing—were able to be delegated to optimized libraries, which were often coded in a lower-level language. This means that the overhead associated with an interpreted language (the cost associated with transpiling the code into processor instructions at runtime) usually does not affect the efficiency of the computation. Moreover, advantages are gained in user time: no compile-time waiting, easier debugging and interactive sessions, and the ability to use the same language for calculation, data processing, and plotting. Because Python emphasizes readability and simplicity, oftentimes written programs are much shorter and simpler than their low-level equivalents.

Python is installed by default in most Linux distributions, and compiling a user-local version from source is relatively simple as well. For Windows machines, the Anaconda distribution includes the scientific libraries mentioned here, although others exist as well. Python also allows packages to be installed locally within a shared system.

However, it should be noted that some modules beyond the core Python libraries are necessary for efficient computation. The following sections describe the main extensions used for the work in this thesis.

B.1.1 NumPy

NumPy is an extension to Python which provides support for pure, memory contiguous arrays and high-level operations on them. In base Python, numbers are represented as objects and are stored in variable-length lists, which add a non-negligible amount of overhead to performing numerical calculations. In addition, many established algorithms operate on a raw memory structure, so having access to it is necessary for backwards compatibility. Any operation that can be expressed on matrices and arrays runs at approximately the same speed as equivalent C code. Since the math used in this thesis is almost entirely matrix operations over various structures, the efficiency provided by NumPy is put to full use. The standard method of importation is through the command

```
import numpy as np .
```

An advantage of NumPy and the abstract representation of matrices is that the back end is decoupled from the implementation, meaning that it can be compiled to take advantage of hardware optimizations for the particular architecture that is used for computation. The BLAS (basic linear algebra subprograms) provide optimized implementations of vector addition, matrix multiplication, etc., which are incorporated into operations within NumPy.

For instance, Intel provides an optimized implementation of BLAS in its math kernel library (MKL). This implementation takes advantage of Intel-specific processor architecture enhancements to optimize for maximum throughput of numerical processing. Different generations of processors have improvements on the x86 core architecture, which are then incorporated into the implementation. Newer processors have improvements to single instructions which act on multiple values at a time, like providing a dot product over a section of a vector rather than having to perform each multiplication and addition individually per instruction cycle. In addition, the operations used within the BLAS can be parallelized to act over multiple cores or machines without changing any of the higher-level interfaces.

What this means is that the correct memory structure for numerical computation can be made through the array creation commands or by converting though `np.array`. Then, the data can be operated on using, for example, `np.transpose` for transposition, `np.dot` for vector and matrix products,¹ or eigensystems calculations or matrix solving through `np.linalg`. These commands remain invariant of the underlying linear algebra implementation. NumPy also provides universal functions, such as `np.sin` and `np.sqrt`, and some data processing tools, such as loading a text file into a numerical array, along with some statistical tools like `np.average` and `np.stddev`.

NumPy is available in most package managers, although if the optimized linear algebra is desired, then it will likely need to be compiled from source. Usually, this involves setting the correct default compiler in the environment variables and modifying the `site.cfg` file to include the desired libraries.

B.1.2 SciPy

SciPy is a Python library that uses the methods exposed in NumPy for tasks that are common in scientific computing, while the scope of NumPy itself is generally limited

¹Or the new matrix multiplication operator `@` if the version is new enough.

to pure numerical operations. Often, these methods are written in a low-level language (such as C or Fortran) and operate on the memory structure provided by NumPy.

The most common use of SciPy for this work is through solving differential equations and numerical integration. It includes a generic interface class `scipy.integrate.ode` that can be set to a number of integrator implementations, such as “VODE” or “LSODA,” which are more common numerical integration libraries each with their own advantages and disadvantages. The types of differential equations used in this thesis—usually in conjunction with an equation of motion—vary with respect to their numerical stability, so the ability to change integration methods and tune solver parameters is useful for correctly solving these problems.

Computation of a definite integral is provided by `scipy.integrate.quad` for one dimensional integrations and `scipy.integrate.nquad` for integration over multiple values. Once again they are coupled to low-level implementations and can be tuned for a given problem. Typically, the numerical integration is used in finding solutions within the Green’s function formalism and, for the most part, sharply peaked functions or infinite limits are readily handled by the built-in functions.

SciPy provides a sparse matrix implementation in `scipy.sparse`, which is able to efficiently store and perform computations on large matrices in which most of the elements are zero. This happens often when working with many-body systems without approximations. The operators themselves—when constructed using a Jordan-Wigner transformation (see Sec. A.1)—are sparse, and typically the Hamiltonian is a summation of a relatively low number of them. Using a sparse matrix saves space in most of these cases, but often a dense matrix is required for other components such as the time evolution operator or the density matrix after a finite time has passed. Calculating a specific eigenvalue directly from a sparse matrix is difficult as well, as the condition number of the matrix is usually large. However, there are some cases, particularly when the system naturally separates into smaller subsystems, where it is useful to use the

exact form of the operators. SciPy offers many different internal memory structures for the sparse matrix, which can be tuned for a given problem as well.

`scipy.interpolate` contains interpolation facilities for multidimensional data and is a convenient way to create a function from fixed data points. The methods range from a simple linear interpolation to a higher-order spline fitting. It usually provides a more accurate derivative or integral estimation for a limited number of data points. When visualizing data, like on a surface plot, it sometimes becomes important to have a strict control over the precise interpolation, rather than relying on the plotting software.

A large number of signal processing algorithms and discrete Fourier transforms are available under `scipy.signal` and `scipy.fftpack` respectively. While these tools are typically used for applications in processing measurements from sensors outside the computer, it is often the case that a particular calculation is too long or difficult to run with a high resolution. Expensive computations often have a level of discreteness associated with them, and it becomes useful to treat the output as the result of an experiment. In some cases, even if the calculation can be run to a perfect resolution and high accuracy, there may be some components of the model that need to be filtered or otherwise processed.

Lastly, SciPy provides optimization and root finding methods through `scipy.optimize`. The non-linear curve fitting (under `scipy.optimize.curve_fit`) is particularly useful, as it computes the least squares fit of data to an arbitrary function. Much of the work in this thesis involves creating an analytic model (which may be a simplified system or an ansatz involving the parameters) and verifying its effectiveness to describe the complex system. A most useful operation is to use a simulation as the input function to the output of a long calculation, both of which might be numerically intractable.

Since SciPy relies on the core facilities exposed by NumPy for numerical processing, then SciPy can simply be installed from a package manager or from source after NumPy and should share the same level of computational efficiency.

B.1.3 Cython

In the rare cases where a computation is desired that does not exist in an optimized library and cannot easily be expressed as a vector or matrix operation, then Cython can be used to compile a module into an efficient form. Cython is an extension to the Python language that allows declaration of static types and interfacing with C routines. By manually specifying types of variables and parameters with the `cdef` command, the compiler is able to remove much of the overhead associated with an interpreted language, such as having to deal with object management or extra time used on control structures. Moreover, the resulting output is in machine language, which means that the processing power is used exclusively outside of the Python virtual machine.

Cython modules have a separate extension and must be compiled separately, but once they are compiled, the usual Python programs can import them just like any other module. The generated C code can be analyzed by the `cython -a` command, which shows how each line of the Cython module corresponds to the C version. This makes it easy to identify inefficient locations where more code is inadvertently added—such as the accidental inclusion of a number as a Python object rather than a numeric datatype. Structures like `for` loops are able to be reduced to a compact C form if the correct type hinting is given. The final compilation to machine code is handled by the system C compiler, and could potentially optimize it much further.

A useful application for a strongly compiled module is for the kernel of a numerical integration or a differential equation solver. When combined with the SciPy routines, much of the overhead of passing parameters and shifting between contexts is reduced. Cython also works well with the NumPy module, as most of the accesses and assignments in a NumPy array can be reduced to a low number of C statements.

B.1.4 Profiling and Testing

Several tools are available for determining an execution profile of Python code—that is, for finding which parts of the program take the longest. For a simple benchmarking of small components, the core library provides the `timeit` module to measure the total execution time. For a function-level breakdown, `cProfile` is a C extension, also included with the core library, which tracks the total number of function calls, as well as the time spent within each function. Often in numerical programming, even single lines can have a large effect on the performance (such as performing operations on very large arrays), so it is useful to profile down to a line-by-line level. The `line_profiler` package, which must be installed separately, can be given a Python function and will time the execution of each individual line within that function.

In simulation, it is sometimes necessary to compare two different models to determine if they match each other under certain conditions. For instance, one might decide to build a simple version of a more complicated, inefficient model or implement a different version that should be identical in theory. Comparing the results by hand—to ensure that any changes have not inadvertently upset past work—becomes very tedious. My preferred method of handling tests is through the `nose` framework, although there are many options available. NumPy includes `np.isclose` and related testing functions for easy access to numerical comparisons within certain error tolerances.

Although `nose` is a unit testing framework, it is useful for creating the full range of tests needed for numerical work. In this work, I divide the testing into multiple levels of scope: implementation (does a numerical function return the expected outputs or is the program representing data correctly), analytic (does a function obey correct symmetries or limits; do two analytic forms match numerically), modeling (does the simulation reproduce the correct results for a smaller system that can be solved in a different way; do two types of simulation match), physical (is energy conserved; are convergence criteria met), and conjecture (does the solution match intuition about the problem). Writing the tests in this manner for a complete problem allows the increase in the level

of complexity of the simulations while minimizing the effect of new errors or regressions. In addition, the tests themselves can be used to determine the simulation execution, such as automatically rerunning sections that fail non-deterministically or by adjusting parameters based on the level of convergence.

Lastly, many tests in numerical programming end up looking quite similar. For example, a function that takes a numeric input is run with a variety of different inputs and something is asserted about the result. However, what we usually want is an assertion over the whole domain of numbers—some property that holds regardless of the input—and check it against some data matching a specification. This is known as *property based testing* and is provided by the Python library `hypothesis`. It works by generating random data that matches a specification (such as three floats for a particular function) and using those inputs as the basis for testing. If a falsifying example is found, the test case is automatically reduced to the simplest possible counterexample that reproduces the error.

B.2 Other Scientific Computing Libraries

Although the bulk of the numerical simulations performed for thesis work was done in Python, there were still a few situations where a suitable module did not exist.

ITensor is a C++ library for implementing matrix product operators and performing DMRG and tDMRG calculations, developed by E. Miles Stoudenmire and Steven R. White. It uses the tensor as the base data structure and allows for the transcription of tensor networks into efficient code, as well as manages the contractions and factorization for matching indices.

In the case of very large matrix operations (size on the order of a million by a million), it becomes necessary to spread the computation over multiple machines. For this case, the ScaLAPACK library is required. ScaLAPACK is an implementation of linear algebra routines that are designed for parallel machines, and a version exists within the MKL.

The routines use a parallel form of BLAS known as PBLAS, which in turn depend on the MPI (message passing interface) for communication. The library itself is written in Fortran, and can be used through a compiled C program. There has been some work in implementing a wrapper for Python, however, it is still in the early stages at the time of writing.

In both of these cases, the expensive numerical computations are already compiled into efficient cores, so writing or extending a higher-level wrappers for these tools remains a possibility for future work.

B.3 Analytic Work

While numerical tools continue to grow in usability and sophistication, the state of computer algebra systems is relatively undeveloped in comparison. Naturally, this is to be somewhat expected, as programming general purpose algebraic tools is much more of a challenge. For this work, I've primarily used Mathematica for when a difficult analytic calculation is needed. In many cases, a given computation would need to be tuned to execute in a reasonable time or might turn out to be outright impossible. Whether or not this sort of work will be easier in the future or will always remain computationally difficult remains to be seen.

B.4 Computational Complexity

In the main text, the efficiency and space requirements were generally mentioned in abstract terms. In this section, we briefly discuss some of the real limits associated with these types of simulations.

Often, these types of calculations are CPU bound rather than memory bound. Even though something like a wavefunction can take up a large amount of space, typically only a few copies are required at any one time. In time evolution, we are often only interested

in a the dynamics of a few observables (such as the electronic current or density), so the intermediate terms can be discarded as the simulation progresses. Even if an entire intermediate state needs to be saved, that still only requires a relatively small amount of space—for instance, a full 32-site wavefunction might only be 100 MB in the MPS method.

For mean-field calculations, systems sizes of 1,000 to 10,000 sites are readily calculated on a single machine, with a processing time on the order of a few hours for 100 time units (the inverse of the hopping frequency). This scales as tN^2 , so even systems with around 1,000,000 sites can be done in an appropriate cluster,² and more processing power can be added for larger systems or for running to longer times. In the case of interacting systems, finding a solution becomes very difficult without any approximations. A single machine can realistically expect to do a simulation with 6-8 sites, and because of the extremely poor scaling, 20 sites is probably the upper bound that a full cluster could compute exactly.

When using matrix product states, for the time evolution that we discussed here, an energy cutoff of 10^{-9} is sufficient for a converged solution and the matrix product dimension limit is set at 5,000, although in practice it never reaches that limit. Even if it had, the whole state would be around 20 GB, which can easily be kept in main memory during the calculation. For simulations out to recurrence, $t = 16$, for a 32 site system—as used in Chapter 3—with a timestep of 0.01, the simulation time was on the order of 3-8 hours on a single machine per simulation.

In tDMRG, since each site is associated with its own tensor and only information from the neighboring sites is needed for each timestep, the algorithm could potentially parallelize extremely well, meaning that systems up to size 3,000 could potentially be simulated within the same time on a cluster. The work to expand this algorithm remains to be done.

²For reference, a cluster as we refer to it here is 1,000 to 10,000 processor cores.

